

**CONCEPTUAL DESIGN AND COMPUTATIONAL DEVELOPMENT OF THRUST
VECTORING SYSTEM FOR UAV APPLICATION**

By

UCHENNA OGEMDI OKWUOSA

**Thesis submitted in fulfilment of the requirements for the degree
Master of Engineering: Mechanical Engineering in the Faculty of Engineering
and the Built Environment at the Cape Peninsula University of Technology**

**Supervisor: Prof Oscar Philander
Co-supervisor: Mr Mornay Riddles.**

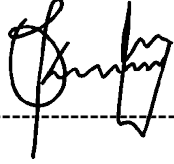
Bellville

September 2020

**CPUT copyright information
The thesis may not be published either in part (in scholarly, scientific
or technical journals), or as a whole (as a monograph), unless
permission has been obtained from the University**

DECLARATION

I, Uchenna Ogemdi Okwuosa, declare that the contents of this dissertation/thesis represent my unaided work, and that the dissertation/thesis has not previously been submitted for academic examination towards any qualification. Furthermore, it represents my own opinions and not necessarily those of the Cape Peninsula University of Technology



Signed

14 - January - 2021

Date

ABSTRACT

Manoeuvrability is a desired and important attribute of an aircraft (both manned and unmanned) if it must fit into the multi-purpose demand of our present-day need. An aircraft which can fit into this must have the capability of taking off at any given /available space and thus quickly get into the air as soon as possible. This plays an important role in aircraft total performance and endurance. With the challenges of limited space for take-off, an aircraft with short take-off ability is highly desired. Several works had been done to achieve short take-off and landing (STOL) but mainly on jet engines with little on pusher propeller aircraft. This propulsion system is gaining more relevance in drone technology due to its operational advantage for short and medium-range purposes like security, surveillance, parcel delivery, medical emergency response, and search and rescue operations. Even though UAVs (Unmanned Aerial Vehicles) with this type of propulsion system can achieve the above-mentioned mission applications, they often fall short due to the need for long take-off distances and therefore long runways.

To tackle this problem, and improve the operational capabilities of Guardian II UAV, a CPUL AMTL (Advance Manufacturing Laboratory Technology) demonstration platform; this research project designed and computationally investigated the means of improving the manoeuvrability and making it operational in the condition mentioned above. One of the ways in which to reduce the ground role (S_g), and to increase the rate of climb (ROC) of an aircraft is through the introduction of short take-off and landing configurations. These flight performance parameters are primarily governed by the dimensionless coefficients for lift, drag and pitching moment.

Literature shows a variety of these devices and their effectiveness in reducing the ground role and increasing rate of climb. Using a design trade-off table with the design specification and requirement of integrating Thrust Vectoring Configuration (TVC) system without major changes in the airframe in view; a shrouded configuration with jet vanes to direct the airflow from a pusher propeller UAV was selected as best suited for this application. The iterative selection choice was governed by these selection criteria namely weight penalty, ease of integration, and suitability.

An experimental investigation using a shroud was conducted to determine the velocity profile of air exiting a pusher propeller configuration as used in the Guardian II UAV. Velocity profiles were obtained for speeds from 2000rpm to 4000rpm, and subsequently, mass flow rates of 11.173kg/s to 23.329kg/s respectively were calculated. The characterization experimental set-up is a test bench equipped with Turnigy C6374 – 200 brushless outrunner electric motor driving a 22 x 10inch three-bladed propeller, speed control device, Pitot tube, manometer and a data logging device.

SolidWorks® 2017 was used to design a shroud with incorporated jet vanes to direct airflow from the pusher propeller; while ANSYS Fluent 2019R was used in the selection and characterization of the jet vanes. Due to the computation resources available, the Reynolds-average Navier-Stokes (RANS) turbulent model was employed to predict the flow parameters of interest. Specifically, three vane configurations were investigated, and results showed that the NACA0012 airfoil was best suited as a jet vane for this application due to its performance showing zero lift at zero deflection angle as desired.

FLUENT was then used to analyse the entire thrust vectoring configuration, i.e. airflows from the propeller through the shroud with vanes deflected through 0° to 5° , and flap angles of 0° , 5° , 10° and 15° to determine the dimensionless coefficients for lift, drag, and pitching moment. The computational domain of length 4800 mm and diameter 495 mm respectively were used as the virtual wind tunnel. The inlet (upstream of the model), outlet (downstream) and sides (walls) boundaries were located at 5L, 10L and 5D of the model respectively. These boundaries represented the propeller freestream airflowing onto the vanes, while the airflows exiting the shroud was acted upon by the vanes and the surrounding respectively. The domain was discretized into 3.8 million elements and inflation layers created around the vanes to predict the flow parameters of interest. A good and acceptable mesh quality was obtained using the localized meshing method. The boundary conditions used for the system characterization to obtain the flow parameters of interest are mass flow inlet and pressure outlet. The mass flowrate obtained from the preliminary experiment was set as the inlet boundary conditions at the speed, and the vane deflection angles were analysed, while the pressure at the exit was predicted in the analysis. This CFD set-up approximated/predicted the coefficients of drag, lift, and pitching moment when the vanes were deflected at the angles considered. The approximated flight performance parameters were used to calculate the Sg and ROC.

The result showed reductions of Sg and increase in the ROC for the different thrust vectoring configurations investigated. The stable performance of the system was obtained at propeller speed from 3000 to 4000 rpm and vane deflection angles of 3° to 5° . At 4° vane deflection angle, a minimum and maximum reduction in GII Sg obtained were 48.12% at 3000 rpm and flaps angle 0° , and 64.98% at 4000 rpm and flaps angle 15° respectively. For the ROC, at 3° and 5° vane deflection angle and flap angle of 5° , 31.28% at 3500 rpm and 31.33% at 4000 rpm respectively, the minimum and maximum improvement in the climbing flight parameter were obtained. The performance was determined by the reduction in power usage by a minimum of 62.37%, and a maximum of 85.53% across the stable and optimal configurations analysed. A minimum of 59.89% at conditions of 2000 rpm, 1° deflection angle, and 0° flaps angle had a corresponding maximum reduction value of 62.36% at the same operational conditions. An optimal power usage which increases with flaps angle was recorded at 4° deflection angle and from 2000 rpm to 4000 rpm.

The result is evident; however, it should be noted that the percentage reduction in S_g , rate of climb and power is expected to decrease when the TVC system is built and integrated onto the airframe of the GII UAV.

The thrust vectoring system decreased the S_g by a maximum of 65.19% and improved the ROC by a maximum of 31.33%. This proves that the set objectives for this research project were met.

Keywords:

Thrust vectoring control system (TVCS), Short take-off and landing (STOL), Manoverbility, aircraft, Unmanned Ariel Vehicle (UAV), ANSYS Fluent, Computational fluid dynamics (CFD)

ACKNOWLEDGEMENT

My sincere gratitude goes to the following people:

Prof Philander: For his invaluable supervision and the inspirational role he played through the process of this study.

Mr Mornay Riddles: For his role in the technical aspects of my thesis. His technical guidance as a co-supervisor was invaluable.

Cyprian Onochie: I was able to stand on my feet in South Africa because he was there through my difficult time as a fresh immigrant.

Mrs Sharon Duplessis: You are my mother from another country. I wouldn't have had a chance to remain in South Africa to complete my study if not for your firm decision and intervention when I was sick.

Prof Veruscha Fester: Not my supervisor but she was there throughout, giving me unreserved moral support as well as other motivations to successfully complete my study.

Qfinsoft team: For their support during the period of my CFD work.

Dr Benjamin Oyegbile: For your great support, guidance and time during this study.

CPGS management: For the financial support that helped me to cope financially.

Ubuntu postgraduate forum: The family where I mostly drew inspiration from to scale through this programme.

My family: For believing in me and praying with to make sure I succeed in my quest for postgraduate studies.

Last but no the least, Ms Raissa Andong Omores whose presence in my life changed lots of things to put me in the stable state emotionally to push this masters programme to an end.

DEDICATION

TO ALL WITH TRUE SENSE OF HUMANITY

TABLE OF CONTENTS

Table of Contents

DECLARATION	i
ABSTRACT	ii
ACKNOWLEDGEMENT	v
DEDICATION.....	vi
TABLE OF CONTENTS.....	vii
LIST OF FIGURES	xii
LIST OF TABLES	xv
NOMENCLATURE.....	xvii
1. CHAPTER ONE: INTRODUCTION	1
1.1 Introduction.....	1
1.2 Background to Research Problem	2
1.3 Research Problem Statement.....	3
1.4 Aim of the Study	4
1.4.1 To develop a thrust vectoring system suitable for propeller aircraft.	5
1.4.2 To investigate the effect of the thrust vectoring system on the pitching motion of an aircraft during take-off.	5
1.4.3 To investigate the effect of thrust vectoring on the ground roll distance of an aircraft.	5
1.4.4 To investigate the effect of thrust vectoring on the rate of climb of an aircraft during the climb phase.....	5
1.4.5 To investigate the effect that thrust vectoring vanes deflection angle would have on the aircraft attitude.	5
1.5 Delineation	5
1.6 Design Requirements	6
1.7 Methodology.....	6
1.7.1 Phase 1 - Literature Review	6
1.7.2 Phase 2 - Determine the Air Velocity Profile on Shrouded Propeller.....	6

1.7.3	Phase 3 – Thrust Vectoring Method Selection and System Characterization	6
1.8	Aircraft Take-off Theory and Thrust Vectoring	7
1.9	Aircraft Take-off Concept.....	7
1.10	Aircraft Operational Forces for Take-off Performance.....	9
1.11	Aircraft Operational Power.....	14
1.12	Aircraft Rate of Climb Concept.....	15
1.13	Aircraft Moment Analysis	17
1.14	Objectives and Approach of Current Research	18
2.	CHAPTER TWO: LITERATURE REVIEW.....	20
2.1	Introduction.....	20
2.2	Thrust Vector Control System (TVCS) Configuration and Method.....	21
2.3	STOL and Reduced Climb Time	24
2.4	Shrouded Propeller Aircraft Developmental Research	26
2.4.1	Experimental Research on Development of Shrouded Propeller for V/STOL	28
2.4.2	UAV Targeted Shrouded Propeller/Ducted Fan for Multipurpose Application	29
2.5	CFD development of thrust Vectoring System.	30
2.5.1	Turbulence model application in Thrust Vectoring Development	31
2.6	Tail Scrape Constrains	31
2.7	Powered-Lift Turbofan Versus Ctol Turprop Aircraft.....	32
2.8	Actuator	32
2.9	Thrust Vectoring Mechanisms/Concepts.....	33
2.9.1	Mechanical Thrust Vectoring Control (MTVC)	34
2.9.2	Fluidic Thrust Vectoring (FTVC)	35
2.10	Advantages and Disadvantages of Thrust Vectoring.....	37
2.10.1	Advantages of Thrust Vectoring	37
2.10.2	Disadvantages of Thrust Vectoring.....	38
2.11	Analysis of Alternative Thrust Vectoring Control Method.....	38
2.11.1	Gimbaled Engine.....	39
2.11.2	Jetavator	40
2.11.3	Jet Vanes	41

2.11.4	Secondary Fluidic Injection FTVCS	41
2.12	Optimal Thrust Vectoring Configuration Selection.....	42
2.13	Correlation between Literature Survey and the Current Work	42
3.	CHAPTER THREE: TVCS CHARACTERIZATION METHODS	44
3.1	Experimental Analysis of Propeller Air Velocity	44
3.1.1	Measurement Equipment and Experiment Setup	44
3.2	Numerical Solution Methods	48
3.2.1	Introduction	48
3.3	Governing Equations of Fluid Flow	49
3.3.1	Continuity Equation	49
3.3.2	Momentum Equation	49
3.4	Turbulence Modelling (TM)	50
3.4.1	Direct Numerical Simulation (DNS)	50
3.4.2	Large Eddy Simulation (LES)	51
3.4.3	Reynolds Average Navier-Stock Models (RANS)	51
3.5	CFD Preliminary Study	56
4.	CHAPTER FOUR: AERODYNAMIC THRUST VECTORING STSYEM CONCEPTUAL DESIGN.....	62
4.1	Optimal Airfoil Selection and Design.....	62
4.1.1	Optimum Airfoil Selection	62
4.1.2	Airfoil Mesh Generation.....	64
4.1.3	Vane Shape Selection Fluent Analysis.....	64
4.1.4	Airfoil Analysis Result.....	64
4.2	Thrust Vectoring System Concept Design and Development (Complete Setup)	66
4.2.1	Design Concept and System Description	66
4.3	Thrust Vectoring Vane Mechanism Design	67
4.4	Shroud Specifications and Design	68
4.4.1	TVCS CAD Geometry Creation	69
4.4.2	Computational Domain.....	73
5.	CHAPTER FIVE: CHARACTERIZATION OF THRUST VECTORING CONCEPTS	74

5.1	Characterized TVCS CFD Analysis	74
5.1.1	Pre-processor	74
5.1.2	Mesh Generation.....	74
5.2	TVC System Solution Analysis.....	78
5.2.1	Fluent Analysis.....	78
5.2.2	Solution Parameters.....	79
5.2.3	Spatial Discretization Scheme.....	80
5.2.4	Virtual Environment Boundary condition.....	84
5.2.5	Mass Flow Inlet	85
5.3	Post-processing.....	86
6. CHAPTER SIX: ANALYSIS, RESULT PRESENTATION AND DISCUSSION		88
6.1	Simulation Analysis.....	88
6.2	Spatial Distribution of Aerodynamic Parameters	88
6.2.1	Qualitative Result Analysis	89
6.2.2	Quantitative Result Analysis.....	94
6.3	GII Operational Characteristics	96
6.4	Aircraft Ground Roll and Take-off Performance Result	97
6.4.1	Take-off Performance of the Aircraft with TVC Configuration	97
6.5	Aircraft Climb Performance Analysis.....	106
6.6	Result Summary	113
7. CHAPTER SEVEN: CONCLUSION AND RECOMMENDATION		114
7.1	Conclusion.....	114
7.1.1	Thrust Vectoring Method Selection	114
7.1.2	TVC Conceptual Design.....	114
7.1.3	Thrust Vectoring System Characterization	115
7.2	Recommendation.....	116
REFERENCES		118
Appendix A:		126
Appendix B: Take-off distance reduction at different α value		127
Appendix C: Percentage Increase in Aircraft Coefficient of Lift.....		129

Appendix D: Percentage increase in Aircraft Coefficient of Drag	130
Appendix E: Input and Output Boundary Conditions.....	131
E.1: 2000 RPM	131

LIST OF FIGURES

Figure 1.1: Flight Phase of CPUT Adaptronics AMTL Technology Demonstrator.....	5
Figure 1.2 Important aircraft take-off velocities (MoTIS, 2007; Sez, 2019)	9
Figure 1.3 Aircraft forces during take-off (AOE, n.d.).....	10
Figure 1.4 Aircraft climbing forces vectors (Sadraey, 2017)	15
Figure 1.5 Aircraft climbing force diagram (Sadraey, 2017).....	16
Figure 2.1: X-31 with canard fore planes (Rockwell-MBBX-31, 1990)	21
Figure 2.2: Three rings, three actuators system (3DOF)(Ikaza, 2000a).....	22
Figure 2.3: Three rings, three actuators nozzle movement (Ikaza, 2000a)	22
Figure 2.4: Three rings, four actuators system (4DOF)) (Ikaza, 2000a)	22
Figure 2.5: Two rings, three actuators (pitch only) (Ikaza, 2000a)	23
Figure 2.6: ISTAR micro air vehicle (Akturk & Camci, 2010)	24
Figure 2.7: Three vane thrust vectoring system (Clarke, 2011)	25
Figure 2.8 Variation of static thrust for shrouded and unshrouded propeller (Platt Jr, 1948). 27	
Figure 2.9 Shrouded propeller mounted and tested at Langley Aeronautical Laboratory (Taylor, 1943)	28
Figure 2.10 Doak VZ-4 (Diseno-art, 2014)	29
Figure 2.11 Shrouded/ducted fan UAV for crosswind application (Fleming et al., 2003).....	30
Figure 2.12: Constraints to avoid tail scrape (Vinayagam and Sinah, 2013).....	32
Figure 2.13: Dual channel development EMA and controller (Bates and Young 2012).....	33
Figure 2.14: Gimbal thrust vectoring system (NASA, n.d.)	34
Figure 2.15: Vane thrust vectoring system (Clarke, 2011).....	35
Figure 2.16: The schematic of a co-flow fluidic thrust vectoring (Li, 2011).....	36
Figure 2.17: Counterflow fluidic thrust vectoring (Li, 2011).....	36
Figure 2.18: Shock wave thrust vectoring system (Li, 2011)	37
Figure 2.19: Gimbale thrust vectoring system (Berrier & Taylor, 1990)	39
Figure 2.20: Gimbale thrust vectoring system for jet engine aircraft (AviationNepal, 2017) 40	
Figure 2.21: Gimbale thrust vectoring system for jet engine aircraft (Wang & Wang, 2016)40	
Figure 2.22: Jet vane mechanism (Sumathy, 2015)	41
Figure 3.1 Velocity profile experiment model	45
Figure 3.2: Velocity profile experiment test bench.....	46
Figure 3.3: Velocity profile experiment full setup	46
Figure 3.4: Velocity profile experiment setup - Side view	47
Figure 3.5: Velocity profile experiment	48
Figure 3.6 Varying Lift coefficient at α_{inf} constant adjustment	57
Figure 3.7: Varying Drag coefficient at α_{inf} constant adjustment	57

Figure 3.8: Varying Lift coefficient at β_{∞} constant adjustment	58
Figure 3.9: Varying Drag coefficient at β_{∞} constant adjustment	59
Figure 3.10: Varying Lift coefficient at β_{inner} increases constant adjustment	59
Figure 3.11: Varying Drag coefficient at β_{inner} increases constant adjustment	60
Figure 3.12: Varying Lift coefficient at β_{∞} decreasing constant adjustment	60
Figure 3.13: Varying Drag coefficient at β_{∞} increasing constant adjustment	61
Figure 4.1 Generated airfoil in ANSYS design modeler.....	63
Figure 4.2: Analyses fluid domain	64
Figure 4.3: CL vs. Deflection angle curve for various airfoils	65
Figure 4.4: CD vs. Deflection angle curve for various airfoils	65
Figure 4.5: CL vs. CD (drag polar) curve for the various airfoils	66
Figure.4.6: Jet vane arrangement on rocket/jet engine aircraft (Chandra Murty & Chakraborty, 2015)	66
Figure 4.7: Design parameters of a shroud (Pereira, 2008).....	68
Figure.4.8: Thrust vectoring geometry model.....	70
Figure.4.9: 2D TVCS showing the vane positioning within shroud	71
Figure 4.10 Vane deflection angles.....	72
Figure 4.11 Simplified and sliced model for fluent simulation	72
Figure 4.12 Computational domain	73
Figure 5.1: Generated mesh view	76
Figure 5.2: Generated mesh showing inflation around the vane.....	77
Figure 5.3: Convergence residual plot	84
Figure 5.4: Overview of CFD.....	87
Figure 6.1: Velocity magnitude along the x-axis of the vane.....	90
Figure 6.2: Pressure magnitude long x-axis of vanes.....	91
Figure 6.3 Velocity contour at different speed and vane deflection angle showing: (a) 2000 rpm, angle 1°; (b) 2000 rpm, angle 5°; (c) 3000 rpm, angle 3°; (d) 3000 rpm, angle 5°; (e) 4000 rpm, angle 1°; and (f) 4000 rpm, angle 5°.....	92
Figure 6.4 Pressure contour at different speed and vane deflection angle showing: (a) 2000 rpm, angle 1°; (b) 2000 rpm, angle = 5°; (c) 3000 rpm, angle = 3°; (d) 3000 rpm, angle = 5°; (e) 4000 rpm, angle = 1°; and (f) 4000 rpm, angle = 5°.....	93
Figure 6.5 Coefficient of lift as a function of deflection angle.....	94
Figure 6.6: Coefficient of drag as a function of deflection angle	95
Figure 6.7: Moment coefficient of as a function of deflection angle	96
Figure 6.8 Enlarged plots of S_g v. propeller speed.....	101
Figure 6.9 Take-off distance (S_g) reduction at $a = 0.000$	101
Figure 6.10 Take-off distance (S_g) reduction at $a = 0.008$	102
Figure 6.11 Take-off distance (S_g) reduction at $a = 0.024$	103

Figure 6.12 Take-off distance reduction pattern of TVC system.....	103
Figure 6.13 Sg v α value @ 4000 rpm	105
Figure 6.14 Sg reduction behavioural curve.....	106
Figure 6.15 GII with TVCS power at 2000 rpm - 4000 rpm.....	109
Figure 6.16 GII power at 0° flaps angle	110
Figure 6.17 Rate of Climb to the Flaps Angles @ 2000 – 4000 rpm.....	112
Figure 6.18 Rate of climb to the vane deflection angles	112
Figure B.1 Take-off distance (Sg) reduction at $a = 0.002$	127
Figure B.2 Take-off distance (Sg) reduction at $a = 0.004$	127
Figure B.3 Take-off distance (Sg) reduction at $a = 0.006$	128
Figure B.4 Take-off distance (Sg) reduction at $a = 0.02$	128
Figure B.5 Take-off distance (Sg) reduction at $a = 0.03$	129

LIST OF TABLES

Table 2.1: TVCS selection analysis result	42
Table 4.1: Geometric properties of the propeller shroud	69
Table 5.1: Skewness mesh metric spectrum	77
Table 5.2: Orthogonal quality mesh metric spectrum	77
Table 5.3: Mesh quality	77
Table 5.4: Working parameters property list.....	78
Table 5.5: Solution parameters	83
Table 6.1 GII operational result 1 (Petersen, 2010).....	96
Table 6.2 GII operational result 2 (Petersen, 2010).....	97
Table 6.3 Total lift coefficient (GII & TVC) at 0° flap	98
Table 6.4 Total drag coefficient (GII & TVC) at 0° flap.....	99
Table 6.5 Total lift coefficient (GII & TVC) at 5° flap	99
Table 6.6 Total drag coefficient (GII & TVC) at 5° flap.....	99
Table 6.7 Total lift coefficient (GII & TVC) at 10° flap	99
Table 6.8 Total drag coefficient (GII & TVC) at 10° flap.....	100
Table 6.9 Total lift coefficient (GII & TVC) at 15° flap	100
Table 6.10 Total drag coefficient (GII & TVC) at 15° flap.....	100
Table 6.11 Power at different propeller speed and at 0° Flaps Angles	107
Table 6.12 Power Percentage Reduction at different propeller Speed and at 0° Flaps Angles	107
Table 6.13 Power at different propeller speed and at 5° Flaps Angles	107
Table 6.14 Power Percentage Reduction at different propeller Speed and at 5° Flaps Angles	108
Table 6.15 Power at different propeller speed and at 10° Flaps Angles	108
Table 6.16 Power Percentage Reduction at different propeller Speed and at 10° Flaps Angles	108
Table 6.17 Power at different propeller speed and at 15° Flaps Angles	108
Table 6.18 Power Percentage Reduction at different propeller Speed and at 15° Flaps Angles	109
Table 6.19 Power difference across the vane angle and propeller speed.....	111
Table C.1 Percentage increase in aircraft coefficient of lift at flaps = 0°	129
Table C.2 Percentage increase in aircraft coefficient of lift at flaps = 5°	129
Table C.3 Percentage increase in aircraft coefficient of lift at flaps = 10°	130
Table C.4 Percentage increase in aircraft coefficient of lift at flaps = 15°	130
Table D.1 Percentage increase in aircraft coefficient of drag at flaps = 0°	130

Table D.2 Percentage increase in aircraft coefficient of drag at flaps = 5°	130
Table D.3 Percentage increase in aircraft coefficient of drag at flaps = 10°	131
Table D.4 Percentage increase in aircraft coefficient of drag at flaps = 15°	131

NOMENCLATURE

A	Aspect Ratio	MAV	Mini Aerial Vehicle
Deflection angle	Deflection angle	MTOW	Maximum Take-off Weight
BFL	Balanced Field Length	SFC	Specific Fuel Consumption
C_L	Coefficient of Lift	STOL	Short Take-off and Landing
CON-DI	Convergent-Divergent	T_o/w	Thrust to Weight Ratio
CTOL	Conventional Take-off and Landing	TVC	Thrust Vectoring control
DOF	Degree of Freedom	TVCS	Thrust Vectoring Control System
ESTOL	Extreme Short Take-off and Landing	MALE	Medium altitude Long Endurance
IBF	Internal Blown Fan	LFL	Landing Field Length
ISR	Intelligent Surveillance and Reconnaissance	UCAV	Unmanned Combat Aerial Vehicle
V	Velocity/Speed	VTOL	Vertical Take-off and Landing
W	Weight	CFD	Computational Fluid Dynamics
ROC	Rate of Climb	C_m	Moment coefficient
P_r	Power	γ	Climb angle

CHAPTER ONE: INTRODUCTION

This chapter gives a brief introduction about the thrust vectoring, the state of the art in thrust vectoring technology, the motivation for this present research, the design requirements, the sets of objectives, and methodology followed to accomplish the aim set for this work. It also presents the sets of equations associated with the areas covered during the course of this work.

1.1 Introduction

Thrust vector control (TVC) enables an aircraft, rocket or other similar vehicles to change the course of the engine thrust or propeller in a direction away from its normal parallel direction of movement (Revolvy, 2016). It brings about a change of attitude of the aircraft in pitch and yaw - depending on the axis in which it is employed. Thrust vectoring during take-off helps to maintain the deflection angle (Deflection angle) to a certain desired angle. Deflection angle is an important parameter of aircraft take-off, and when maintained at a certain value by thrust vectoring, it leads to quick rotation of the aircraft at a speed lower than its normal rotation speed at the time when the conventional control surfaces are ineffective to control the vehicle. One of the biggest advantages of TVC is that it greatly improves turning performance at both low and high speeds (Dhawan, 2014). Another advantage of thrust vectoring is that it allows an aircraft easy manoeuvrability when it enters and recovers from a controlled flat spin during the yaw motion of the aircraft without the concerns surrounding the rudder losing effectiveness at a high deflection angle. Also, in level flight, TVC makes trimming possible, and this, in turn, increases aircraft endurance due to the reduced drag. In addition to the aforementioned, thrust vectoring can add short take-off and landing (STOL) capability to conventional take-off and landing (CTOL) aircraft, however, a simpler, lighter, and cheaper options are favoured more and advisable for consideration when making a choice (as explored in details in section 2.11). Meanwhile, the simpler, lighter, and cheaper options will enable the achievement of a quick take-off and a high range with less effect on the weight of the vehicle.

In practice, there are two means of achieving thrust vectoring. They are by a fluidic actuator, or by the mechanical actuator. Fluidic thrust vectoring utilizes the jet of secondary fluid to deflect the primary jet from the nozzle, and can be in various types such as a.) shock vector control (SUC), b.) throat shifting (TS), or c.) counterflow method (CM). However, in general, they all use a secondary fluid source to create asymmetric pressure distribution around the surface of the nozzle. Mechanical thrust vectoring, on the other hand, uses some mechanical moving actuators to deflect either the entire nozzle to cause a change of attitude of the aircraft, or to deflect some vanes in and out of the exhaust plume of the nozzle to cause the change of

attitude. However, they are easier to control when compared to fluidic type thrust vectoring despite being subject to fatigue caused by continuous moving action of the surfaces. Fluidic thrust vectoring is commonly used in practice due to its simplicity as it has no moving parts – when compared to a mechanical thrust vectoring system which requires a lot of mechanical actuation components.

1.2 Background to Research Problem

CPUT's (Cape Peninsula University of Technology) Advanced Manufacturing Technology Laboratory (AMTL) has unmanned aerial vehicle (UAV) platform development as one of its core research areas. The AMTL has produced the first and second generations of UAV which are used for aerial surveillance. However, due to a high demand for a utility vehicle to fit into both combat and ISR (Intelligence, surveillance and reconnaissance), but hampered by the long runway needed for the take-off of the developed vehicle; the AMTL seeks to improve the UAV by addressing and improving its response time and endurance.

In UAV design, certain attractive points are focused on to satisfy certain single mission objectives and performance capabilities. Range and endurance are therefore important parameters in classifying mission platforms such as surveillance, target acquisition or combat, for UAVs (Petersen, 2010); and short take-off and landing (STOL), and reduced climb time are equally essential factors to consider due to their effect on the response time and endurance of the aircraft. The detailed research work done by Mair and Edwards (1965), Baokai (1995a), and Clarke, (2011) proved that one of the best methods to achieve these important performance capabilities is with the aid of thrust vectoring.

In the next generation of close combat aircraft, victory will be determined by the aircraft agility performance, flight quality and in the post-stall status. At this stage, the conventional control surfaces (rudder, ailerons, etc.) are ineffective and unable to control the aircraft, and in such situation, thrust vectoring control should be adopted for mobility (Baokai, 1995). With thrust vectoring control, the flight envelope is extended and moves into the post-stall region with thrust vectoring as the only control means. It has been originally envisaged that thrust vectoring would provide upward vertical thrust to give aircraft vertical take-off and landing (VTOL) or short take-off and landing (STOL) ability. Subsequently, vectored thrust showed great potential to assist an aircraft to perform various manoeuvres in combat situations which cannot be performed by conventional planes. To perform turns, conventional aircraft must rely on aerodynamic control surfaces only while aircraft with thrust vectoring manoeuvres majorly with less reliance on the control surfaces. (Petrescu, 2013)

Furthermore, aircraft uses different propulsion systems such as electric motor, piston engine, turbofan, turbojet, turboprop, scramjet ramjet, and jet engine (Dinç, 2015) for its propulsion actions. Piston engine and electric motor-powered aircraft utilize the power of propeller(s) to

generate thrust for the vehicle operation either by pushing (pusher propeller aircraft) or pulling (puller propeller aircraft) actions. Based on the propulsion systems (jet or turbine engine, piston engine or electric motor) employed, the method of thrust vectoring system differs. Aircrafts with piston or electric motor propulsion system employ mechanical systems for its pulling or pushing propulsion actions; while jet or turbine engines propulsion systems use fluidic or mechanical thrust vectoring system.

So far, most studies on this subject matter have been conducted on a jet or turbine engine aircraft. For instance, Schaefermeyer, (2011) worked on thrust vectoring for a thrusting jet engine to aid autonomous and human piloted vehicles for space visit; and Mason and Crowther, (2004); Ball, (2008); Gogoi et al, (2013); and Majil, (2016) separately worked on enhancing aircraft with agility by incorporating TVC system all based on jet engine propulsion system. Most recently, Chan's (2020) work on J-20 series stealth jet fighter was fitted with thrust vectoring control system. Notably, thrust vectoring systems operating in jet or turbine engines are achieved either by nozzle or vane movement to deflect the exhaust plume to cause a change of attitude. To date, little work has been done on a pusher propeller aircraft powered by internal combustion or reciprocating engine. For instance, X-31 and F-18 HARV are powered by an F404-GE-400 turbofan engine, F-15 Eagle and F-16 falcon by Pratt & Whitney's F100 engine etc. (Amick, 2005; Connors, 2010), and thrust turbofan W-15 engines power China's stealth jet fighter (Chan, 2020).

Meanwhile, this work focuses on studying the effect of a thrust vectoring system on a pusher propeller UAV to cause a change of attitude on the existing platform, leaving it with STOL capability and reduced climb time.

1.3 Research Problem Statement

Aircrafts are controlled using conventional control surfaces (ailerons, rudder, elevator, and flap) for pitch, yaw, and roll attitude during take-off, climb, and cruise of the flight envelope. The possibility of the control surfaces to manoeuvre the aircraft is dependent on certain factors: the ground roll distance that it must cover to acquire enough lift to begin take-off, the velocity it must roll at, the deflection angle (Deflection angle) to maintain to avoid stall etc. Aircraft performance in take-off and climb stage is of vital importance as this phase plays an important role in the aircraft's total endurance and response time. Importantly, an aircraft requires enough ground speed, and the lift forces to begin take-off processes and then climb. The longer the duration of time that the aircraft spends on the runway, the greater the delay in response time and the more fuel it consumes, which in turn shortens the operation time. The development of air vehicles with long operational time (endurance) has therefore become an optimum goal for aircraft designers.

This desire of an aircraft with long operational time is born out of increasing need and application of UAV in different areas such as security surveillance, search and rescue, parcel delivery services, and agricultural (irrigation and pest control) purposes, and highly needed in combat environments faced with limited spaces for take-off. The possibility and success of these operations in the confined spaces requires UAV with short take-off and landing (STOL) capabilities. The STOL capabilities enhance the UAV by saving the fuel required thereby increasing its total endurance. And most importantly, it makes the operation of the UAV at any available space (short runway) possible in the cities and rural areas

The UAV demonstrator developed by CPUT's AMTL is yet to fit into the multi-mission purpose and currently does not possess the ability to operate from a short runway. This affects the aircraft's mission, purpose and endurance. The UAV platform specifications include a payload weight of 1.0 kg, wing span of 2.50 m, length of 1.5 m, a maximum take-off mass (MTOM) > 7 kg & $< 20/25$ kg, and a flight altitude > 150 m. These specifications require a system which can rotate the aircraft when the control surfaces are ineffective and that can initiate earlier lift-off than possible in the present system.

This work focuses on investigating the effect that thrust vectoring would have on the take-off and climb phase of an aircraft; and to develop a thrust vectoring and actuation system to be incorporated into the existing UAV platform to improve its operational ability in these phases.

1.4 Aim of the Study

Air vehicles, in general, as illustrated in Figure 1.1, have seven phases in operation. They are as follows:

- Phase 1-Take-off: This phase begins from the point of brake release of the aircraft through the ground roll, the rotation (governed by the velocity (V_R) that the aircraft must rotate at, the thrust (T), the lift (L) over the wings, and the drag (D) it must overcome to continue take-off) to the start point when it leaves the ground. The take-off phase is governed by the ground roll distance (S_g), engine thrust (T), speed (V), pitch angle (θ), and rotation speed (V_R).
- Phase 2-Climb: This phase involves the point when aircraft leaves the ground until it clears obstacles at a height of 15 m governed by thrust, power, and deflection angle.
- Phase 3 and 5 is cruise.
- Phase 4 is loiter
- Phase 6.and phase 7involve descent and landing respectively.

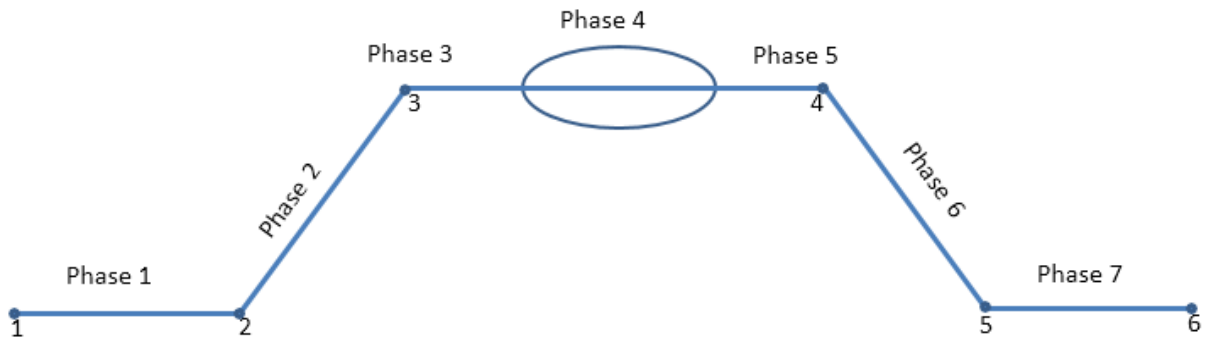


Figure 1.1: Flight Phase of CPUT Adaptronics AMTL Technology Demonstrator

This study aims to investigate the effect of thrust vectoring on the following.

- i. Take-off phase; and
- ii. Climb phase of CPUT's Guardian III UAV.

It is anticipated that the thrust vectoring actuation system will cause a change of attitude of an aircraft at a speed lower than V_R thereby reducing ground roll distance S_g at phase 1. The idea is also to maintain a maximum Deflection angle to cause reduction of climb time (phase 2), while still operating using the same specifications of the CPUT's guardian III UAV.

To achieve the aim mentioned above, the following sub-objectives which should also be achieved are:

- 1.4.1** To develop a thrust vectoring system suitable for propeller aircraft.
- 1.4.2** To investigate the effect of the thrust vectoring system on the pitching motion of an aircraft during take-off.
- 1.4.3** To investigate the effect of thrust vectoring on the ground roll distance of an aircraft.
- 1.4.4** To investigate the effect of thrust vectoring on the rate of climb of an aircraft during the climb phase.
- 1.4.5** To investigate the effect that thrust vectoring vanes deflection angle would have on the aircraft attitude.

1.5 Delineation

This research does not cover the following:

- The effect of a thrust vectoring system on the roll and yaw motions of an aircraft.
- The integration of the thrust vectoring system to be designed onto the airframe.
- The design and analysis of the entire UAV together with the thrust vectoring system.

1.6 Design Requirements

The guardian UAV requires a system to rotate it earlier than what is obtainable in the present system, therefore, the thrust vectoring system to be developed should have the capacity to handle the system at its present design specifications of MTOM of 15kg.

1.7 Methodology

The process of solving the problem at hand was carried out in three different phases. They are:

Phase 1 - Literature review.

Phase 2 - Test to determine air velocity profile on a shrouded propeller

Phase 3 – Thrust vectoring method selection and system characterization.

1.7.1 Phase 1 - Literature Review

A review of past studies done on fixed wing STOL and ESTOL aircraft achieved with the aid of thrust vectoring (TVC) was carried out to understand the design configurations employed with respect to the different propulsion systems placement and actuation system configurations.

Different TVCS methods and configurations were examined, compared and the best configuration suitable for a propeller aircraft was selected.

1.7.2 Phase 2 - Determine the Air Velocity Profile on Shrouded Propeller

Phase 2 aims to determine the air velocity around and along a propeller shroud and thrust vectoring vane, the following steps were employed.

- i. Construct shroud to house the propeller
- ii. Assemble the engine and the shroud on the test bench
- iii. Construct a Pitot tube holder and setup measurement system.
- iv. Run experiment at variable propeller speed.
- v. Propose or develop a suitable thrust vectoring system concept.

The above was done using the operational and physical parameters of Guardian III.

1.7.3 Phase 3 – Thrust Vectoring Method Selection and System Characterization

1.7.3.1 Select Optimal Thrust Vectoring System

This step involved a careful study and a subsequent selection of a thrust vectoring system, among the existing configurations to give the best result. The chosen configuration was the simplest and cost effective.

1.7.3.2 Characterize Thrust Vectoring Concepts

This characterization involved CFD (using ANSYS FLUENT) analysis performed on a CAD modeled vane of the thrust vectoring using the velocity profile of the shrouded propeller obtained from the velocity profile experiment and the physical parameters of the thrust vectoring concepts as an input parameter. The purpose of the aforementioned is to determine the size of the thrust vectoring vanes to be incorporated into the system as it must be capable of producing a force to rotate the aircraft when vectored.

1.8 Aircraft Take-off Theory and Thrust Vectoring

As established from flying possibilities, the flying objects which are either lighter than air (hot air balloon) or heavier than air (aircraft), do so based on established principles. The aircraft must overcome all forces that inhibits flying (force of gravity, drag and weight) before it can lift off into the air (Anon, 1997.). Overcoming the limiting force and speed up during ground roll means the thrust produced by the engine must be high enough to cancel all drag force and the weight of the aircraft. Specifically, the take-off speed depends on the air density, the gross weight, the configuration of the aircraft, wind speed, runway conditions (runway surface, runway slope), setting of the flaps, and airframe shape and smoothness (Skybrary, 2016). For an aircraft to take off, there must be balance between the lift and weight, the drag must be lesser than the thrust produced by the propelling engine (Anon, 1997). The wing made in airfoil shape causes the speed of air above the wing to flow faster than that at the bottom thereby reducing the surrounding air pressure at the upper surface of the wing. The ability to create a lifting force is further explained by the principle of continuity (continuity equation) in fluid flow, and the principle of pressure variation as explained by Bernoulli in his work that explains the pressure variations in a flowing stream of water. The amount of lift and drag force created is dependent on the shape of the airfoil and can be calculated using the equations outlined under flight theory detailed in (Anderson, John David, 1984; Anderson, 2013).

The decision to use airfoil to design the vane used for this work was born out of the desire to utilize the force of air stream from the propeller to create vectoring force to rotate the aircraft, and to use the principle of the pressure variation to create lift force to augment the lift generated by the wing so that the aircraft can take-off earlier than it would ordinarily.

1.9 Aircraft Take-off Concept

The aircraft, be it a little twin engine has the same principle and same sequence of velocities. These velocities are in the same order of V_0 , V_1 , V_r , and V_{LO} and they must be executed before an aircraft can take-off successfully. The distance at which these velocities are accomplished before lifting off an aircraft is called the ground roll. The ground roll (S_g) is measured from the time of brake release (V_0) to the lift-off velocity (V_{LO}). This distance is dependent on the aircraft ability to generate all the forces required for its successful take-off when all other conditions

(Good engine performance, etc.) are normal. The lift-off velocity which is usually $1.2V_{stall}$ (Figure 1.2b) by aerodynamic standard is considered important and it is desired as early as possible to increase aircraft endurance. To increase aircraft operational time (endurance), the target is to decrease the stall velocity (V_{stall}) thereby decreasing the take-off distance (S_g). The reduction of S_g goes a long way reducing the fuel consumption and the power expended to during take-off. During aircraft take-off process, different velocities shown in Figure 1.2(a –f) are observed for guiding the operational stages of lifting off. V_1 known as the decision velocity shown in Figure 1.2c needs to be calculated before take-off can be initiated considering the weight of the aircraft to determine if the lift force generated so far will be able to overcome the weight. Other important factors to consider is the flaps setting, environmental factors, and the engine condition after which, the decision whether to take-off or not will be made. When the decision is made, the next important take-off operation is the rotation of the aircraft. The operation characterizes the application of controls to cause the pitching up of the nose of the aircraft. This sees the nose landing gear to lift off the ground for another few distances run before final lift-off of the entire aircraft. The speed at the point of this operation is known as rotation velocity shown in Figure 1.2d. As shown in Figure 1.2f, at this point, the aircraft either continues taking off or the aircraft will be brought to a stop following the decision made before. V_1 . V_r is also calculated taking into consideration the weight and other important factors. At this take-off speed, the lift force generated must have been able to overcome the weight of the aircraft to aid it to leave the ground. After a little distance run with the main landing gear still on the runway, the aircraft leaves the ground when the V_{LO} is reached and it continues to climb until it clear obstacles as shown in Figure 1.2e. The obstacle clearing height depends on the design and side of the aircraft. The obstacle clearing height of CPUT AMTL platform is 15 m

Additionally, the S_g (V_0 to V_{LOF}) has no rule of thumb as to what it must be. It depends on the lift force capable of supporting the weight (W) of the aircraft causing it to lift-off, and thus suggesting that an aircraft cannot leave the ground except the lift force needed for it to do so is acquired by the control surface.

As soon as this force is acquired, take-off is initiated irrespective of the distance covered. So, it is desirable that this lift force is generated as quickly as possible and all possible way to achieve must be explored. There comes the importance of an additional component like the TVC system to generate lift force to augment that generated by the wings to support the premature take-off. The forces generated by the TVC system will be added to the forces acting on an aircraft on the runway (Figure 1.3) ready for take-off. Moreover, a short S_g enhances the performance and endurance of the aircraft irrespective of the operational characteristics

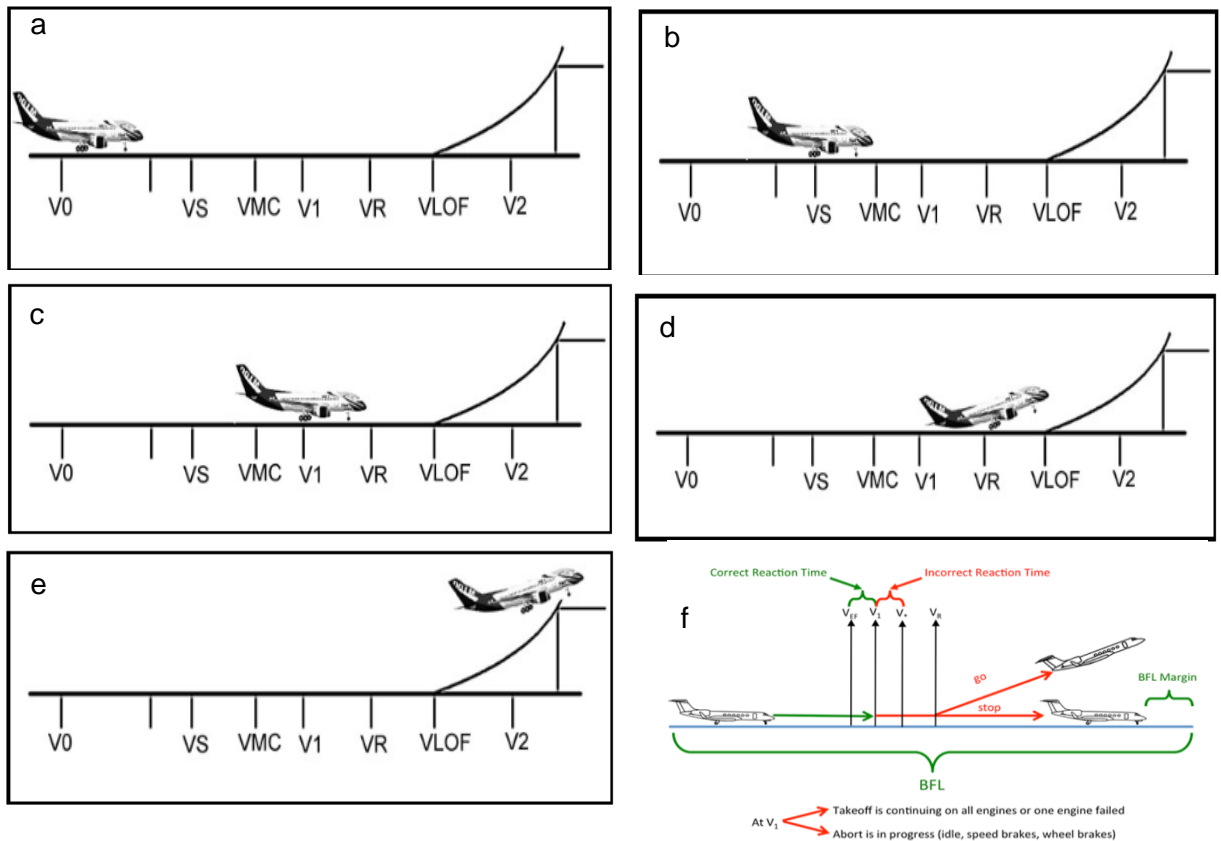


Figure 1.2 Important aircraft take-off velocities (MoTIS, 2007; Sez, 2019)

1.10 Aircraft Operational Forces for Take-off Performance

For a successful take-off of an aircraft, there are associated forces interacting with each other. Some of these forces are acting to limit the operation while some are acting to aid the operation. The set of forces acting to aid the operation must overcome the set limiting to operation for an aircraft to successfully move from the point of V_0 to the point of V_{LOF} and eventually leave the ground. Figure 1.3 presents an aircraft on a runway with the interacting forces acting on it.

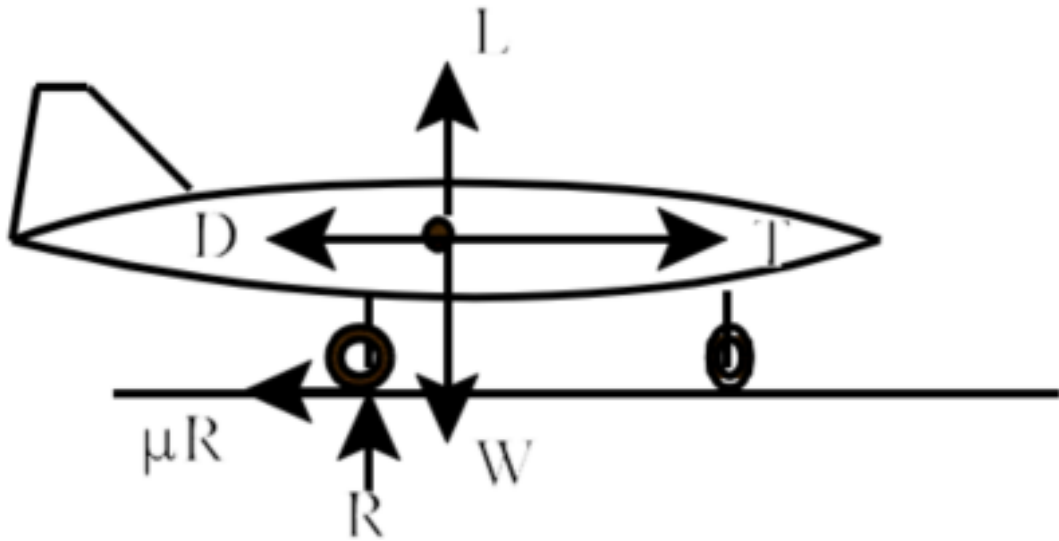


Figure 1.3 Aircraft forces during take-off (AOE, n.d.)

A typical aircraft has lift (L), weight (W), drag (D), thrust (T), normal (R) and the friction force (μR) as the aerodynamic forces acting on it during operation. With W , D and μR as the forces limiting the operation while T , R and L , are acting to aid the operation. Their relationships and actions are direction (vertical and horizontal) dependent and act in obedience to Newton's third law of motion. The directional forces are described below.

1.10.1.1 Vertical Forces

These forces comprise the lift force which tends to pull the aircraft off the ground, the weight pulling it down against the actions of the lift force to keep it on the ground and the normal force as a result of the aircraft weight, hence, for the aircraft to lift off the ground, the aircraft wing and in the case including the TVC system should be able to generate a force higher than the weight of the aircraft. The relationship of the forces acting in this axis is presented in equation 1.1.

$$L + R - W = 0$$

Equation 1.1

1.10.1.2 Horizontal Forces

The horizontal forces acting are the Thrust force (T) generated in the case of the UAV under consideration by the propeller propelled by an internal combustion engine. This force is responsible for the horizontal ground run and an inclined run of the aircraft during the ground roll and climb performance. The drag force (D) which opposes the forward motion of the aircraft

acts due to the interaction of the fast-moving air with the UAV fuselage and the wings. Depending on the angle of attack (AOA), aerodynamic conditions of the wings and the fuselage, the operational stage of the aircraft, and some environmental factors, the drag force can either be due to pressure force (causing pressure drag) or skin friction force (causing friction drag). During take-off, when the aircraft speed is low, and at a small angle of attack, the drag of the aircraft is due to skin friction force. The second of the horizontal forces is the frictional force (μR) action due to the ground effect between the take-off and landing gears of the vehicle. The rate of change of forward motion of the aircraft is dependent on how it can generate high thrust to overcome the limiting drag and the frictional force. The mathematical connections binding these forces are shown in equation 1.2.

$$T - D - \mu R = m \frac{dV}{dt} \quad \text{Equation 1.2}$$

1.10.1.3 Total Aircraft Equation

The total equation is the combination of the horizontal and the vertical. It takes into account the dimensionless quantities (lift C_L and drag coefficient, C_D), the wing area (S), the density (ρ) of the air during the operation, the velocity of the aircraft (V), the weight (W), the thrust (T), also the gravitational acceleration (g), and finally the constant a which is dependent on the take-off thrust and the static thrust. All these quantities are represented in equation 1.3.

$$\frac{dV}{dt} = g \left(\frac{T_0}{W} - \mu \right) - \frac{g}{W} \left[\frac{1}{2} \rho S V^2 (C_D - \mu C_L) + a \right] V^2 \quad \text{Equation 1.3}$$

Furthermore, careful integration of equation 1.3 with respect to the change in distance travelled yields the ground roll distance S_g shown in equation 1.4

$$Sg = \frac{1}{2\frac{g}{W}\left[\frac{1}{2}\rho SV_{LO}^2(C_D - \mu C_{Lmax}) + \alpha\right]} \ln \frac{g\left(\frac{T_o}{W} - \mu\right)}{g\left(\frac{T_o}{W} - \mu\right) - \frac{g}{W}\left[\frac{1}{2}\rho SV_{LO}^2(C_D - \mu C_{Lmax}) + \alpha\right]V_{LO}^2} \quad \text{Equation 1.4}$$

(Williams, 1972; AGARD, 1974; Daidzic, 2016; AOE, n.d.)

Meanwhile, equation 1.4 is simplified and presented in equation 1.5

$$Sg = \frac{1}{2B} \ln \frac{A}{A - BV_{TO}^2} \quad \text{Equation 1.5}$$

Where

$$A = g\left(\frac{T_o}{W} - \mu\right)$$

$$B = \frac{g}{W}\left[\frac{1}{2}\rho SV^2(C_D - \mu C_L) + \alpha\right]$$

$$V_{LO} = 1.2V_{stall} = 1.2\sqrt{\frac{2W}{\rho_{\infty}SC_{Lmax}}} \quad \text{(Anderson, 2013)} \quad \text{Equation 1.6}$$

$$\alpha = \pm \frac{T-T_0}{V^2}$$

Equation 1.7

The lift and the drag can be calculated using both equation 1.8 and 1.9

$$L = \frac{1}{2} \rho_{\infty} V_{\infty}^2 S C_L$$

Equation 1.8

$$D = \frac{1}{2} \rho_{\infty} V_{\infty}^2 S C_D$$

Equation 1.9

Notably, the thrust (T) based on the propeller system of the CPUT demonstrator UAV is 61N; while the coefficient of rolling friction is taken as 0.04, a standard dry concrete surface taken from Anderson (2013).

From equations (1.1-1.9), the aircraft design parameters playing an important role during the take-off are the wings span (S), the weight (W), thrust (T) and the maximum lift (C_{Lmax}). The ratio of these parameters (W/S , and T/W) determines the performance of the aircraft at take-off. Another importance parameter found in equation 1.1 is the ratio between the thrust and square of the velocity at lift-off ($T/V^2 = \alpha$) in equation 1.3. The alpha (α) value is the difference between the thrust at lift-off and the static thrust to the speed of the aircraft. As the thrust to speed ratio increases, S_g increases. This parameter adds to the aerodynamic characteristics as it increases the C_{Lmax} . Additionally, optimizing wing loading and thrust-to-weight ratio are geared towards optimizing thrust-to-speed ratio which aids in decreasing the ground roll. A watch out in all these is drag C_D , and it must be minimized as the increase in C_D degrades the conditions needed for a quick take-off, thereby increasing the ground roll.

1.11 Aircraft Operational Power

With regards to the endurance and high performance, the longer the S_g , the lower the endurance and the overall performance. The longer the S_g , the higher the power usage which amounts to high fuel consumption. For a propeller aircraft, the thrust produced by the propulsion engine is a function of the propeller efficiency, the air speed, and the power. Therefore, the available power (TV) for propeller aircraft can be computed using equation 1.10

$$TV = \eta P \quad (\text{Filippone, 2012; Sadraey, 2017}) \quad \text{Equation 1.10}$$

Where T is the engine thrust, V is the air speed, P is the power, and η is the propeller efficiency.

Other factors contributing to the climb performance for propeller propulsion system is the power ratio ($C_L^{3/2}/C_D$), and other aircraft characteristics (lift, drag, and weight). Considering these factors, the power value can be computed using equation 1.11.

$$P_r = \sqrt{\frac{2W^3 C_D^2}{\rho_\infty S C_L^3}} \left(\frac{C_D}{C_L^{3/2}} \right) \quad (\text{Sadraey, 2017}) \quad \text{Equation 1.11}$$

Notably, for an aircraft with constant operational characteristics, the power is an inverse function of the $C_L^{3/2}/C_D$, as can be seen in equation 1.11.

Therefore, the TVC system to be integrated onto the fixed airframe of the CPUT AMTL GII platform must be optimized to increase the power ratio for effective performance and increased endurance.

1.12 Aircraft Rate of Climb Concept

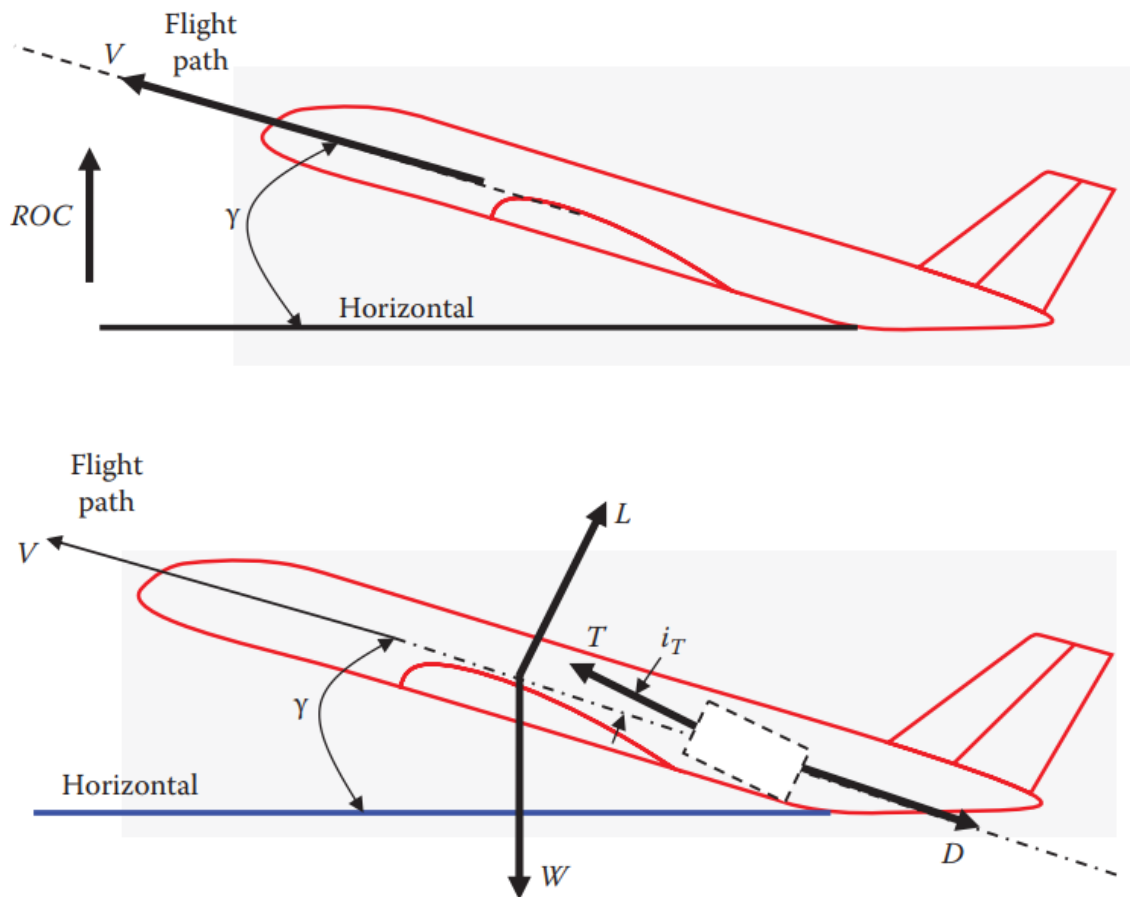


Figure 1.4 Aircraft climbing forces vectors (Sadraey, 2017)

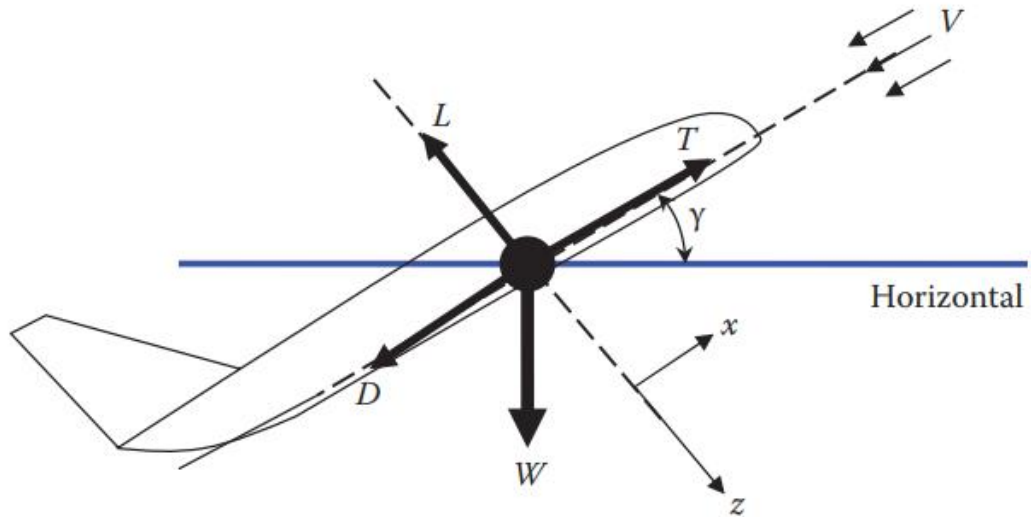


Figure 1.5 Aircraft climbing force diagram (Sadraey, 2017)

The general climb equation considering the forces vectors shown in Figure 1.4 and 1.5 is given as:

$$T \cos(i_T + \alpha) - D - W \sin(\gamma) = ma = m \frac{dV}{dt} \quad (\text{Sadraey, 2017}) \quad \text{Equation 1.12}$$

Assuming a constant climb speed, $AOA = 0$, thrust line coinciding with the flight path is assumed, and a simplified equation 1.13 is obtained

$$T - D - W \sin(\gamma) = 0 \quad \text{Equation 1.13}$$

An important parameter for the operation of the TVC system during climb phase is the angle of climb (γ) which can be calculated from equation 1.13 as

$$\gamma = \text{Sin}^{-1} \left(\frac{T-D}{W} \right) \quad \text{Equation 1.14}$$

Furthermore, for an aircraft to lift off the ground and climb, an important performance parameter ROC (rate of climb) shown in Figure 1.4 determines the aircraft ability to climb successfully until it clears obstacles. ROC, a vertical component is the velocity of the aircraft normal to the ground.

This parameter depends on the power delivered by the propulsion engine which loses thrust at this phase of flight (Filippone, 2012) which determines the amount of power required to accomplish this flight phase. High power ratio means lower power required which translates to lower rate of climb. The ROC for an aircraft is obtained by the use of equation 1.16

$$ROC = V \sin \gamma = \frac{TV - DV}{W} = \frac{\eta P - DV}{W} \quad \text{Equation 1.16}$$

Where ηP is the available power, and DV is the required power.

Equation 1.16 shows that ROC can be reduced by optimizing the available while trying to reduce the required power (Sadraey, 2017; Filippone, 2012)

A full consideration of the aircraft characteristics yields equation 1.17

$$R/C = \frac{TV C_{climb}}{W} - \left(\frac{C_D}{C_L^{3/2}} \right) \sqrt{\frac{2}{\rho_\infty} \frac{W}{S}} \quad \text{Equation 1.17}$$

(Filippone, 2012; Sadraey, 2017)

1.13 Aircraft Moment Analysis

The possibility of taking off prematurely, the UAV is dependent on the ability of the TVC system to create moment to rotate the UAV at its design specifications. Moment is the force x the distance from the TVC to the centre of lift of the aircraft.

The pitching moment is obtained using equation 1.18

$$C_m = \frac{M}{qSc} \quad \text{Equation 1.18}$$

$$q = \frac{\rho V^2}{2} \quad \text{Equation 1.19}$$

Where M is the pitching moment, q is the dynamic pressure of the air calculated using equation 1.19 above, S is the wing area, and c is the length of the chord of the vane. While C_m is a dimensionless coefficient obtained from the computational analysis. V is the maximum air velocity at a different propeller rotational, and ρ is the air density.

1.14 Objectives and Approach of Current Research

Drawing from the survey of the literature presented in the next chapter on thrust vectoring application on a pusher propeller aircraft using shroud and vanes, a considerable amount of work has been done to prove the viability of thrust vectoring in manoeuvring aircraft at various flight regimes. However, most works done so far have been mainly on a jet engine-powered aircraft, whereas the ones on propeller-powered aircraft are on a puller configuration. After an extensive literature review, the author could not find data on the TVC system for pusher propeller systems under investigation. The pusher configuration, although has recently gained attention for use in UAVs (predator drone, US endurance UAV, etc.), the research data on the topic is limited compared to the data which exists on the importance, usage and advantages of applying it in modern technological operations. In the research conducted thus far on thrust vectoring with regards to different propulsion systems, vital pieces of information such as the percentage by which the take-off distance is reduced by a shrouded propeller are unavailable. The unavailability could be because none of such research on the shrouded TVC system exists in the open and accessible domain. However, the research on propeller aircraft focuses only on a gimbal method of thrust vectoring - which is a proven technology for effective manoeuvrability, but it is not effective at the take-off stage, and low speed as it causes serious instability to the vehicle. The instability notably comes from the yaw and roll motion produced when the engine is swivelled downward for pitch control (Schaefermeyer, 2011; Carstens, 2017).

The above-mentioned factors highlight the need for a substantial and systemized investigation to determine the effect that thrust vectoring will have in shortening the take-off distance of a pusher propeller aircraft. The investigations have been conducted and the procedures and findings are presented in different chapters of this thesis.

Chapter 1: This chapter gives a brief introduction about the thrust vectoring, the state of the art in thrust vectoring technology, the motivation for this present research, the design requirements, the sets of objectives, and methodology followed to accomplish the aim set for this work. It also presents the sets of equations associated with the areas covered during this work

Chapter 2: This chapter first describes a brief review of works done in this under investigation covering the take-off and climb operational researches as well as the concepts of thrust

vectoring and shroud systems. Furthermore, it presents the thrust vectoring concept and iterative study to select suitable TVCS method for GII UAV.

Chapter 3: This chapter first covers the preliminary experimental work done to obtain the propeller air velocity and all the test bench design steps and set-up. It thereafter presents CFD theories and all mathematical turbulence model, methods and preliminary CFD studies to ensure the accurate set-up of the analysis process.

Chapter 4: This chapter focuses on the selection process to obtain suitable airfoil used for the design of the vanes. It also presents the TVCS CAD model, the description of the component parts of the system, and the computational domain creation using Solidworks

Chapter 5: This section accounts for the CFD FLUENT analysis performed on a CAD model described in section 4.3 using parameters obtained from the velocity profile experiment detailed in section 4.4. It explicates the set-up processes employed in characterizing the designed TVC system to establish the drag, lift coefficient, force and pitching moment generated when the vanes are deflected at a different vane deflection angle.

Chapter 6: The chapter presents the characterization result of the TVC system. It shows the percentage increase in lift, drag and moment of the aircraft. It also covers the calculation and percentage reduction in S_g , power and rate of climb. Overall, it presents the proof of the effectiveness of the TVC system in giving the GII UAV STOL capabilities.

Chapter 7: This chapter gives the conclusions drawn from the analysis and it also offers some recommendations for future research to improve the system.

Furthermore, Appendix A presents the result of a propeller profile experiment employed for calculating the mass flow rate, and used as an input value for the inlet boundary condition. Appendix B contains the take-off distance reduction at different flaps angle, vane deflection angle and propeller speed. While Appendix C shows the percentage increase on the lift and drag coefficient of the aircraft; Appendix D presents the inlet and outlet boundary condition profile used for the simulation.

CHAPTER TWO: LITERATURE REVIEW

This chapter first presents a brief review of works done in this study under investigation, covering the take-off and climb operational researches as well as the concepts of thrust vectoring and shroud systems. The chapter also discusses the thrust vectoring concept and iterative study to select suitable TVCS method for GII UAV.

2.1 Introduction

Thrust vectoring gives an aircraft, the potential to change the orientation of the thrust from its engine(s) with the aid of vanes or nozzles to control the attitude of the vehicle (Revolvy, 2016). Thrust vectoring is a system that enables an aircraft to redirect the thrust of its exhaust plume or propeller in a direction other than its normal parallel direction of movement. It brings about a change of attitude of the aircraft in pitch and yaw motion but dependent on the axis in which it is employed. Thrust vectoring during take-off helps to maintain the angle of attack (AOA) to a certain desired angle. AOA, being an important parameter of aircraft take-off, when maintained at a certain value by thrust vectoring, leads to quick rotation of the aircraft at a speed lower than its normal rotation speed. When the conventional control surfaces are ineffective to control the vehicle, thrust vector control (TVC) provides the advantages of greatly improved turning performance at both low and high speeds (Dhawan, 2014). Entering and recovering from a controlled flat spin without the control surfaces losing their effectiveness at a high AOA is one of the advantages of thrust vectoring (Defenseissues, 2013). In level flight, thrust vectoring makes trimming possible. This in-turn increases aircraft endurance due to a reduction in drag. Furthermore, thrust vectoring can add STOL capability to conventional take-off and landing (CTOL) aircraft, however, it is always advisable to consider more simplified, light weighted and low-cost options. These lightweights and low-cost options will enable the achievement of a quicker take-off and a high range with less effect on the weight of the vehicle. The ability of a fixed-wing aircraft to achieve short take-off and landing (STOL) or vertical/short take-off and landing (VSTOL) has been a point of focus for aerospace designers for over 50 years due to the benefit of it operating at short or zero field length (Joslin & Miller, 2009). Historically, the evolution and research on thrust vectoring date back to the 1960s when Dr W. Hersbst made predictions concerning the agility in future aircraft to the point where there is minimum aerodynamic power in the post-stall region (Connors, 2010). According to Hunt (2015), for the agility and STOL/VSTOL capability to be achieved, vectored thrust by tilting the propeller is necessary to control lift so that the thrust is aligned with the airship lift axis and is used primarily for vertical and short take-off and landing.

2.2 Thrust Vector Control System (TVCS) Configuration and Method

An enhanced flight manoeuvrability program was formed to test thrust vectoring technology (Rockwell-MBBX-31, 1990). This flight test program focused on flight agility within the post-stall regime. X-31 used canard foreplanes mounted just aft of the nose for primary pitch control with thrust vectoring as the secondary control, and it achieved controlled flight at 70° AOA. Thrust vectoring was combined with a flight control system to make manoeuvre at a high AOA possible in a combat situation. To improve manoeuvrability in pitch (up and down), and yaw (right and left), three paddles for thrust vectoring mounted aft fuselage were directed into the engine exhaust plume as shown in Figure 2.1.



Figure 2.1: X-31 with canard fore planes (Rockwell-MBBX-31, 1990)

In order to achieve a multi-axis thrust vectoring system that is mechanically actuated, Ikaza, (2000) improved an existing EJ200 with 1-Dof CON-DI nozzle into a 3-DoF. He designed a convergent-divergent nozzle with multi-axis thrust vectoring which was mechanically actuated and capable of diverting/deflecting the engine gas at the divergent part of the nozzle, and in so doing avoided the complete movement of the nozzle by orienting the divergent part of the nozzle to cause deflection of the gas with the aid of hydraulic actuators.

Three configurations were employed, and they are shown in Figures 2.2 to 2.5.

- a. Three rings, three actuators system (3DOF)

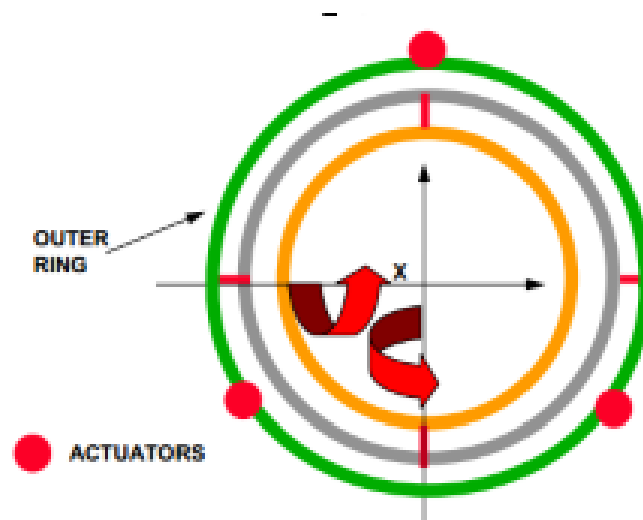


Figure 2.2: Three rings, three actuators system (3DOF)(Ikaza, 2000a)

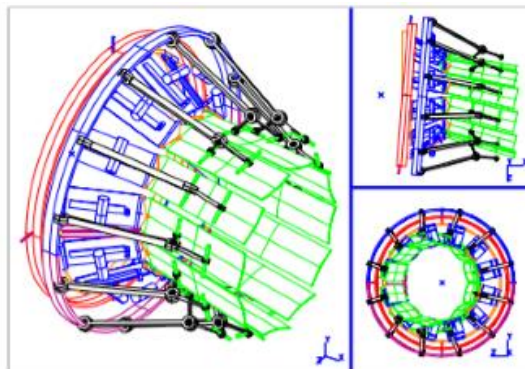


Figure 2.3: Three rings, three actuators nozzle movement (Ikaza, 2000a)

b. Three rings, four actuators system

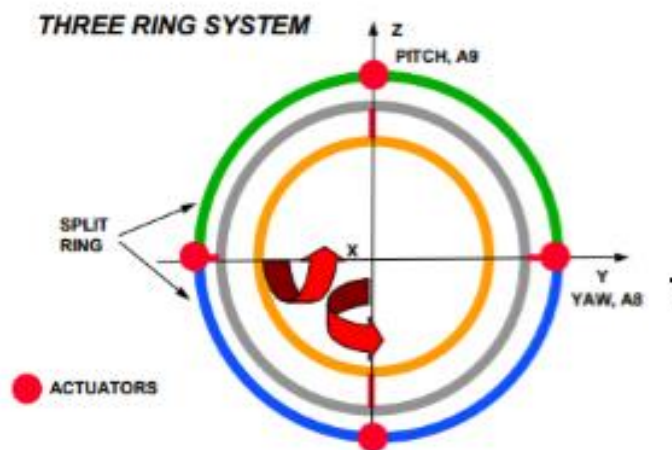


Figure 2.4: Three rings, four actuators system (4DOF) (Ikaza, 2000a)

c. Two rings, four actuators system

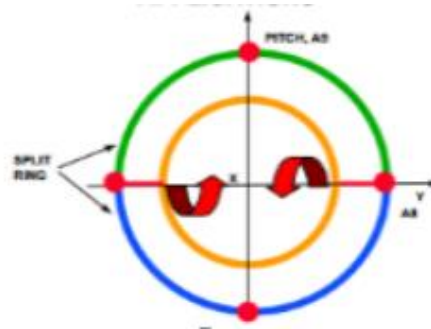


Figure 2.5: Two rings, three actuators (pitch only) (Ikaza, 2000a)

The result showed that the system can vector at a maximum angle of 23.5° and possible vectoring of 360° . However, the three ring-actuation systems could achieve good attitude control only at rapid cruise, climb, high-speed strike, but not on take-off, supersonic cruise, low cruise, and loiter. Also, an independent control system for the nozzle exit was designed for this purpose.

Additionally, the Allied Aerospace Company developed the iSTAR micro air vehicle (MAV) in the year 2000. The iSTAR used an OS-32 SX single cylinder engine (Figure 2.6), which develops 1.2hp. It also used a directly driven fixed pitch propeller. The component comprises a fan system enclosed by a duct, centre body (for avionics and subsystems), and an actuator is controlled by a moveable vane(s) for thrust vectoring, and the centre body houses the engine(Akturk, 2010).

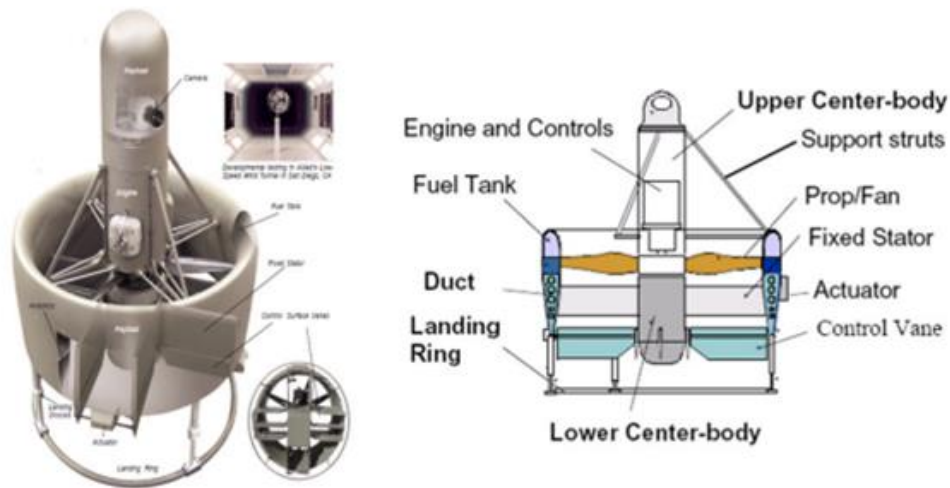


Figure 2.6: ISTAR micro air vehicle (Akturk & Camci, 2010)

2.3 STOL and Reduced Climb Time

Mair and Edwards, (1965) investigated the effects of thrust vectoring on the take-off and landing distance of both jet engine and propeller aircraft on the assumption of wing loading of 73.24kg/m^2 to 1220.60kg/m^2 , the aspect ratio of 5 to 48, thrust to weight ratio of 0.26 to 0.47 for jets, and 0.32 to 0.58 for the propeller. The study greatly emphasized an aircraft using deflected thrust and investigated it from the point of take-off from rest until it reached a height of 15.24m, and landing from a height of 15.24m until it came to rest. Their investigation was able to yield the following results.

- The major parameters affecting take-off distance were T_o/W and the ratio of the wing loading to the coefficient of lift, not the thrust to weight ratio and stalling speed. Also, the maximum coefficient of lift possible was due to the available aspect ratio and thrust to weight ratio.
- Take-off distances of the order of 304.8m can be realized a lot easier for a propeller aircraft with Thrust to weight ratio = 0 - 45, this distance can be achieved with $2 < 18.60\text{kg/m}^2$ a1-16 W/A less C_{Ls} of 9. With $C_L = 5$, these conditions were met by making wing loading = 292.95kg/m^2 and aspect ratio = 7.
- For a high thrust velocity (T_o & V), C_L of 2-5 and with undeflected thrust based on the T_o/w assumed, a reduction of 152.4m was achieved.

It can be deduced from their investigation that a reduction in take-off distance is possible at some certain T_o/w , ranges of C_L and aspect ratio.

Furthermore, Clarke (2011) investigated the possibility of replacing the conventional control surfaces with a cheap mechanical thrust vectoring system as used in X-31 by rescaling the

TVC system. He developed the TVC system with three large external paddles placed at equidistance to each other around the circumference of the nozzle as presented in Figure 2.7. These paddles were connected to a hydraulic actuator that caused deflection of the paddles between the range of -60° to $+35^\circ$ into and out of the exhaust flow. The result showed a reduction in the take-off rotation speed of 43mph, roll distance by 25%, and landing roll distance from 2300m to 500m (though only suitable and possible for UCAV and not for Male UAV).

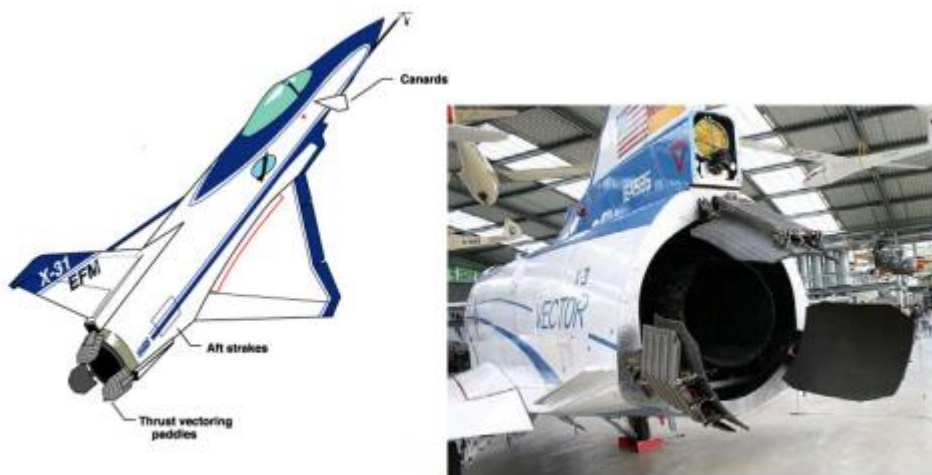


Figure 2.7: Three vane thrust vectoring system (Clarke, 2011)

Based on that work, the three vanes thrust vectoring system can be explained thus.

Take-off Ground Roll: Velocity at the point of rotation was 57.09m/s for UCAV and 38.79m/s for Male UAV with the engine thrust held at its maximum thrust.

Take-off Rotation: AOA assumed to be increasing by 1% until the wing acquires enough lift to support the aircraft. The analysis showed the identical result for both UCAV and Male UAV when $L-W=0$.

Take-off Climb Out: At the height of 10.666m (airworthiness height), and AOA was fixed at the value from the previous stage, both UAVs showed an identical result. Beyond this height, UCAV attained a velocity = 12.5m/s and attaining desired cruise altitude of 12.192km at the desired speed of Mach 0.9 simultaneously. While in the Male UAV, the cruise height was in two stages with a velocity of 6.1m/s. In the first stage, at an altitude of 4.572km, they accelerated to a cruise speed of Mach 0.3488. They then finally climbed to loiter altitude of 7.620km with AOA treated as a variable, then analyzed to find the best corresponding thrust

required. Also, the climb angle as a variable was iterated to obtain optimal flight path to meet thrust requirement while operating the engine at 97.5%.

Zhao Baokai (1995), studied the effects of TVC on aircraft (YF-17 and F-15s) to determine the variation of lift and drag properties as well as the variation in mobility performance after applying a two-dimensional nozzle alongside pneumatic manoeuvring. The study revealed that at low speed, the lift was high and decreases with rise in Mach number and when AOA is between $0^\circ - 14^\circ$, the obtained lift was a linear function of AOA. Maintaining a constant Mach number, aircraft will always possess enough lift coefficient at any thrust angle. Specifically, AOA on the wing can be reduced, which correspondingly reduces the drag. With Mach number ≤ 0.25 for YF-17 and 0.4 for F-15s, the aircraft pitch developed by TVC constantly maintains constant pitch movement of the aircraft. Similarly, some take-off and landing performance studies have shown that for conditions of thrust to weight ratio of 0.89, centre of mass of 44%, a wing loading of 302kg/m^2 , the temperature of -15°C , on sea level, and dry runway; the thrust to weight ratio resulted in nearly half the take-off distance with a large thrust to weight ratio, while wing loading increased in ground roll distance.

In addition, Vinayagam and Sinah (2013) performed computational analysis using GPOPS with four control strategies for the take-off of a modeled F-18/HARV aircraft. These were done using different pitch control effectors in collaboration with: (i) stabilator, (ii) stabilator and flaps, (iii) stabilator and thrust vectoring nozzle, and (iv) stabilator, flaps and thrust vector nozzle. These were geared towards determining the benefits of a thrust vectoring nozzle together with other control means in order to reduce the take-off distance and time using the optimal control methodology.

With the limits of velocity between $0-100\text{ms}^{-1}$: $\alpha= 0 - 13^\circ$ $q= -0.3- 0.3\text{rad/s}$, $\Theta= 0 - 20^\circ$ $Z_E= -18 - 0\text{m}$, $X_E 0 - 1200\text{m}$; the results showed that a shorter take-off distance was realized in case 4 with thrust vectoring deflected upward to rotate the plane at 17ms^{-1} (Minimum speed limit even though TVC pitch control power was very high and thus enough to rotate the aircraft at zero speed). Firstly, the ground roll distance was lowered by lowering the lift-off speed from 68.2ms^{-1} to 62.6ms^{-1} reducing the distance to 222.8m from 266.6m, and AOA increased to 12° from 11.2° with 7.5° downward deflection of thrust vector nozzle against 1.5° .

2.4 Shrouded Propeller Aircraft Developmental Research

The authorities in shrouded propeller performance for aircraft application performed a series of research on this subject matter in the 1930s. To date, reference is still being made to the excellent and noble works done by them. The early aircraft propellers were designed for high performance in high speed cruising flight, so, the early researchers' primary objective was to improve the efficiency of the propellers. In so doing, they incorporated shroud around the propeller to improve its performance at low speed and take-off performance. The shroud helps

to increase airflow through the propeller (Platt Jr, 1948; Oppermann, 1937). Furthermore, Platt experimentally tested 1219.2 mm (4-foot) of varying lengths and diffuser angles for both shrouded and unshrouded propellers. The result of the investigation (Figure 2-8) indicated that a shrouded propeller mount superiority over the unshrouded propeller by producing thrust more than twice higher whilst at the same power consumption.

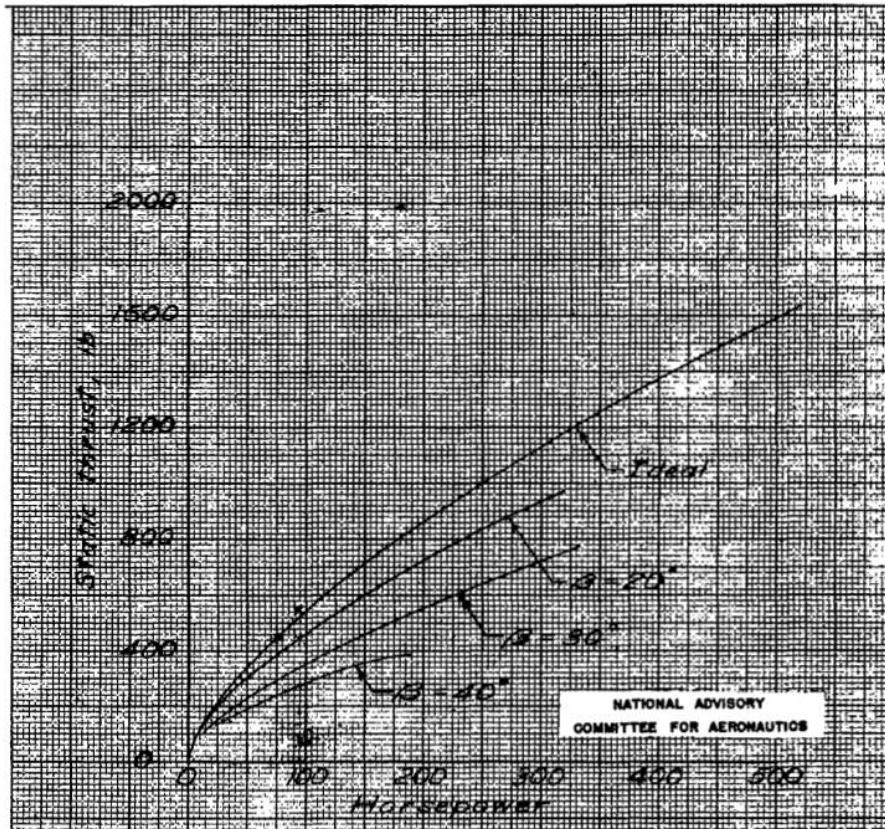


Figure 2.8 Variation of static thrust for shrouded and unshrouded propeller (Platt Jr, 1948)

The work done by Platt and Kruger laid the foundation on this subject matter and was extended by Sacks and Burnell (1962) to establish the principles upon which researches on the subject of shrouded propellers rely on. To account for the performance of shrouded propeller, different researchers and research centres/laboratories including National Aeronautic and Aerospace Administration (NASA) conducted a series of experiments on different standard sizes of the shroud enclosed propellers. Abrego and Bulaga (2002) from NASA reported that a negative duct AOA helped them to produce high propulsion force and the vertical component of the force vector aids the duct (shroud) to generate some lift. Similarly, so many factors were considered and studied to determine their effect and to maximize the effectiveness of shrouded propeller already established by early scientists. Taylor(1958) performed an experiment to study the effects of shroud-lip radius of curvature, shroud length, diffuser angle, and most

especially the effect of the exit distance of the shroud to the ground regarding the thrust it could produce for take-off purposes (Figure 2-8). The procedure showed that all the mentioned quantities studied have an effect on the static thrust produced by the shroud and the performance efficiency. Notably was the shroud length which indicated that minimum length was required to give room for pressure rise adequate to develop axial dynamic pressure. Furthermore, increasing the exit area was accompanied with a loss in static efficiency but less dependency on the diffuser angle.

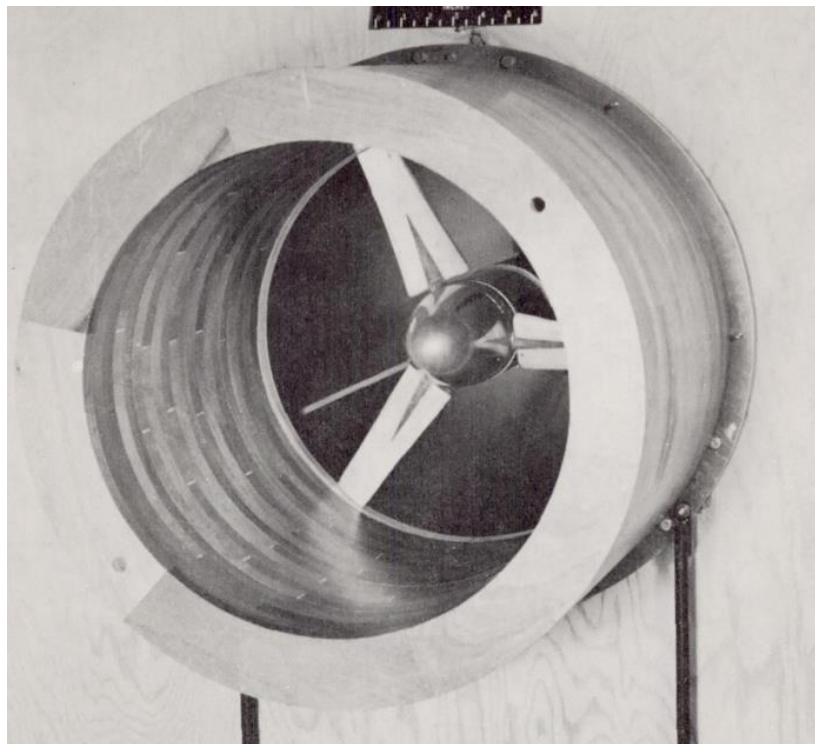


Figure 2.9 Shrouded propeller mounted and tested at Langley Aeronautical Laboratory (Taylor, 1943)

Meanwhile, the aim to develop an aircraft which could be operated in any condition and space has created the need to ultimately develop vertical/short take-off and landing vehicles. This has also necessitated research into the use of shrouded propellers and ducted fan to achieve that aim. The section below explains further.

2.4.1 Experimental Research on Development of Shrouded Propeller for V/STOL

To fully utilize the operational advantage of a ducted fan and a shrouded propeller, the research into vertical/short take-off has been attempted. These attempts yielded good results experimentally and then moved onto the application. In 1950, Edmund R. Doak, Jr developed VTOL aircraft equipped with two wingtip-mounted 1524 mm (5-foot) diameter ducted fan propellers which he proposed to the US army (aviationsmilitaires, 2017; Omics, 2014). This

vehicle was accepted and the model Doak VZ-4DA was successfully tested at a NASA facility in 1956 (Figure 2.10).



Figure 2.10 Doak VZ-4 (Diseno-art, 2014)

Following the breakthrough in ducted fan and shrouded propeller research by the early researchers, several funded developmental pieces of research to actualize the existence of robust and full functional fix-wing and rotary-wing UAV's for all condition application have been conducted. Studies from Yaggy and Mort (1961)(Kenneth W. Mort & Yaggy, 1962) experimentally verified the power, free stream velocity, duct angle of a 1219.2 mm (4-foot) diameter ducted fan mounted on the wing tip of an aircraft to establish the lift, and the thrust and pitching moment of the ducted fan equipped aircraft at the speed range of between 0 to 192.608 Km/h. The result indicated that the ducted fan increased the aerodynamic characteristics of the aircraft. Another significant finding that can be deduced from Yaggy and Mort's work is that when the duct is equipped and supported with vanes both at the inlet and exit of the shroud to vary the thrust, it plays a great role in the maneuverability of the aircraft at a reduced power.

2.4.2 UAV Targeted Shrouded Propeller/Ducted Fan for Multipurpose Application

The experimental research on the shrouded and ducted fan propelled aircraft grew so big and mostly propelled by the curiosity to develop air vehicles to fit into multipurpose; surveillance,

search and rescue, parcel delivery, medical emergency ambulance (Tesla, 1898; Fleming et al., 2003) These mentioned functionalities and operations are within the confines of clustered cities, thus they require some high level of safety (Pereira, 2008). During the last two decades, there has been a paradigm shift, and an increase in the research around UAVs and several tremendous results have been achieved. One of the breakthrough outputs with shroud application is US patent work invented in 1992 by Cycon et al. (1992) where the pitch change from two countered propeller in a shroud generates the lifts required to operate the UAV. Also, with varying design considerations including the incorporation of vanes, Fleming et al. (2003) computationally and experimentally investigated the improvement of the control of a ducted fan UAV for proper operation at a crosswind using the design shown in Figure 2-11. The investigation yielded a 21% increase in static thrust when the setup was operated at a speed greater than 8 000 rpm.

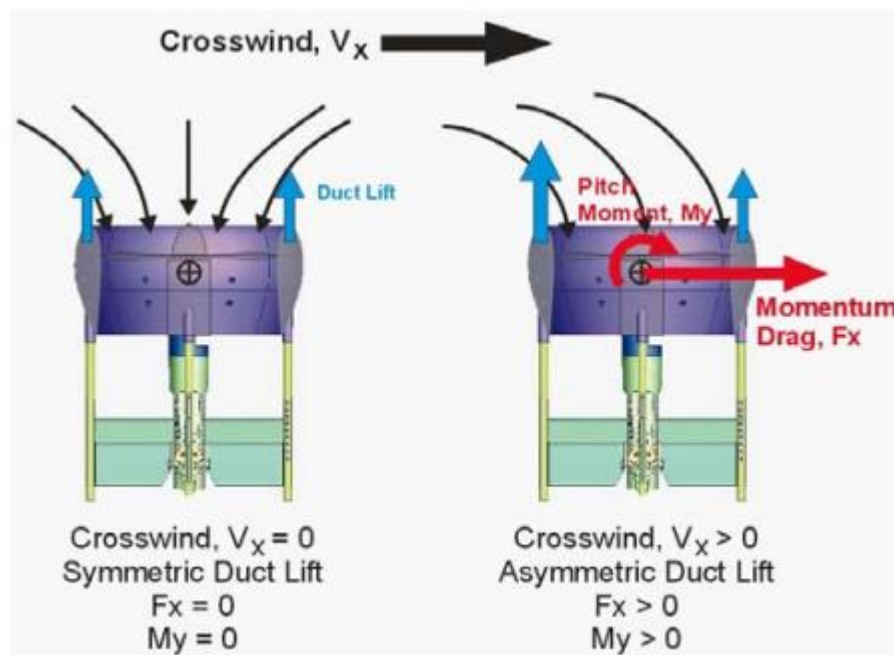


Figure 2.11 Shrouded/ducted fan UAV for crosswind application (Fleming et al., 2003)

2.5 CFD development of thrust Vectoring System.

Fluidic and mechanical thrust vectoring system have been developed by different scholars through computational means to establish the performance characteristics of the system. A study by Prasath et al. (2020) analysed a dual throat chevron nozzle of thrust vectoring system alongside other nozzles to determine its effectiveness in reducing aircraft noise using ANSYS fluent. The investigation showed that chevron nozzle gave a better performance in terms of noise reduction with effect on the nozzle performance and the efficiency of the thrust vectoring system. Majil (2016) used CFD to determine the effectiveness of thrust vectoring nozzle

deflection angle on the overall performance of an aircraft fitted with a thrust vectoring system and operating at subsonic speed. Their optimized flow parameters in direct proportionality to the deflection angle yielded an increase in the thrust force to effectively control the aircraft at subsonic speed. Also, on the account of increasing thrust force for missile control, Sankar and Sreejith (2018) employed ANSYS fluent to study the modified geometrical model of a thrust vectoring system and found that the modification improved the thrust force value by 18480N from the compared figure and the exit temperature of the system were improved.

2.5.1 Turbulence model application in Thrust Vectoring Development

In computational analysis, there is no superior turbulence model/closure. However, different RANS turbulence model (Spalart allmaras, $k - \omega$, $k - \varepsilon$, and RSM) gives different degrees of accuracy depending on the nature of the analysis being conducted as well as computational cost. Živković et al. (2014) computationally investigated the pressure distribution on a two-dimensional thrust vectoring nozzle with obstacle tab (jet vane) at the exit area with different turbulence closures. Their work involved variation of influential parameters (with shadowed ratio: 10 %, 20 % and 30 %; tab gap 0, 2, 1, 6.3 and 13.3 mm; expansion: 2.2 and 2.9) of the nozzle performance. The result revealed that transitional $k - \omega$ and RSM model gave a better pressure distribution prediction accuracy due to the associated flow separation discovered during the wind tunnel experiment. But $k - \omega$ was found to give better distribution at a lower computational cost. Investigating a shock vector control nozzle, Forghany et al. (2018) studied the effect of free-stream flow, fluidic angle, secondary pressure ratio and nozzle pressure ratio of a convergent-divergent nozzle. They employed unsteady RSM and Spalart-Allmaras turbulence model to determine the effect of these operational parameters on the thrust vectoring performance at Mach number range between 0.05 and 1.1. The following different sets of results: increasing the free-stream flow Mach number deteriorate the thrust vectoring performance, the increase and decrease of the secondary and pressure ration respectively increases the agility of the system while optimization of the fluidic injection angle improves the overall performance of the system through the reduction of the free-stream effect were obtained. Through computational means, Noaman et al. (2019) established that secondary flow injection location and the nozzle divergence half-angle had more influence on the performance parameters of a secondary injection thrust vectoring control system when operated at Mach number equal 2.75.

2.6 Tail Scrape Constrains

The AOA to be maintained by an aircraft during and prior to lift-off is dependent on and limited by the tail clearance of the aircraft from the ground. Based on this, (A. Vinayagam & Sinha, 2014) reviewed the angle of attack limit of 13° imposed to avoid tail touching the runway and added path constraints based on the formula below and presented in Figure 2.12:

$$\theta \leq \sin^{-1} \left[\frac{z}{z_0} \sin^{-1} \right] \text{ (Vinayagam and Sinah, 2013)} \quad \text{Equation 2.1}$$

Since the tail scrape constraints are no longer effective after aircraft liftoff, the result is shown in the graph below:

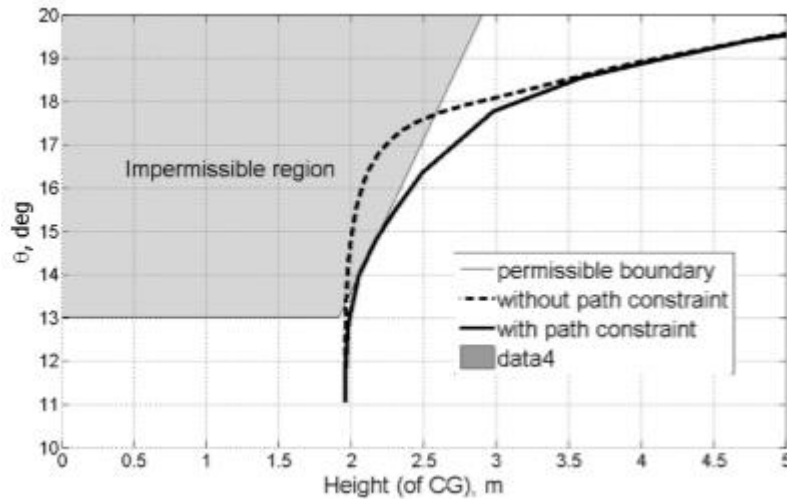


Figure 2.12: Constraints to avoid tail scrape (Vinayagam and Sinah, 2013)

2.7 Powered-Lift Turbofan Versus Ctol Turbprop Aircraft

A propulsion system has a different fuel consumption penalty especially in conditions of extreme short take-off and landing (ESTOL) where more power is required to cause a quick liftoff of the aircraft within the limited take-off field. The study carried by (Gologan & Schmitt, 2010) showed that under the same test conditions, a turbofan contained 0.29 as its thrust-to-weight ratio, and $w = 550\text{kg/m}^2$ BFL of 1867m and LFL of 15661m, whereas a turboprop had a power to weight ratio of 183W/kg, and a wing/loading of 375kg/m^2 BFL of 1325m and LFL of 1017m.

As noted, both aircraft were sized for ESTOL, and an approach angle of -3° & -6° was considered for the field length condition. A shorter field length was achieved with -6° approach for the same fuel burn to -3° approach. However, fuel burn increased with shorter field length, and IBF aircraft had a higher fuel penalty to a turboprop.

2.8 Actuator

The electromechanical actuator (EMA, shown in Figure 2.13), an electro-hydrolic actuator (EHA), heritage electro-hydraulic actuator (HEHA), and integrated actuating pulse (IAP) are

possible actuation means to control the thrust vector. According to a study conducted by Bates and Young, (2012), EMA as a modern developed actuation mechanism has simplicity and cost advantages over another actuator type. The EMA approach was successfully employed in the Apollo service propulsion system (SPS) to perform the critical mission of the trans-lunar injection manoeuvre.

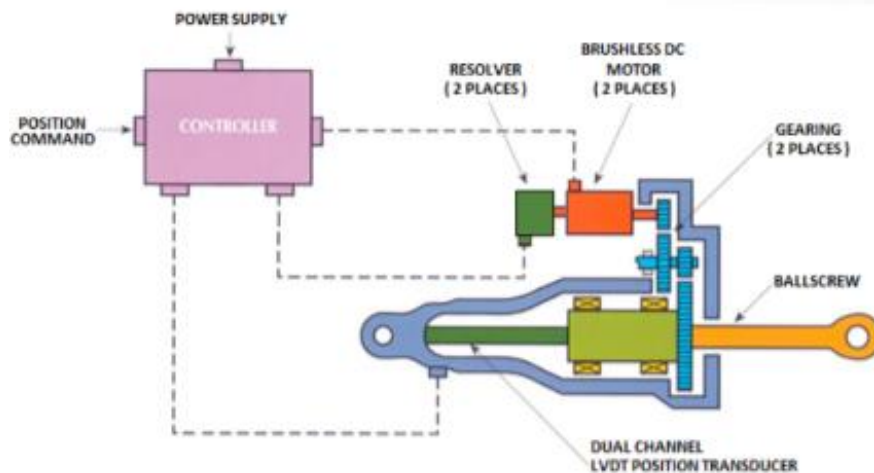


Figure 2.13: Dual channel development EMA and controller (Bates and Young 2012)

At different points in aircraft operations, there is always a need to recover the aircraft from some level of instability or loss of ability of the control surfaces to pull the vehicle into full control. This loss of ability is caused by different factors namely a high angle of attack and a high lift which causes the aircraft to stall. When the aircraft stalls, the chances of it entering into flat spin is high due to loss of control power by the control surfaces. There is still a possibility for the aircraft to be flyable at a post-stall region with an increased C_L and thrust to weight ratio. According to Carter (2005), proper consideration has to be given to some criteria like: (i) whether the aircraft has enough thrust to overcome the high drag increase, (ii) whether the aircraft has the control that will not be rendered ineffective by separated flow over the wings and tail, and (iii) whether C_L remains great enough in post-stall to overcome the aircraft weight to make the operation of the aircraft at post-stall region possible. For all this to be possible, a non-aerodynamics control (thrust vectoring) needs to be developed to control the aircraft when aerodynamic surfaces are ineffective because of flow separation.

2.9 Thrust Vectoring Mechanisms/Concepts

Generally, two means exist by which thrust vectoring can be achieved. They are by mechanical, and by means of a fluidic thrust vectoring system.

2.9.1 Mechanical Thrust Vectoring Control (MTVC)

This involves deflection of gas flow away from the nozzle's longitudinal axis by movement of some mechanical systems to change the angular position of the exhaust nozzle by either hydraulic or pneumatic means. It is known for its effectiveness, and can be retrofitted into an existing system but the problem with MTVC is its complexity. The complexity, weight, integration and aerodynamic inefficiency of the mechanical system limit its application. This system consists of two different application types, they are internal thrust vectoring system – which permits only pitch control; and external thrust vectoring - which permits both yaw and pitch controls. Also, different techniques are available in mechanical thrust vectoring, these include gimbaling the nozzle, moving the divergent flaps or vanes to deflect the exhaust flow.

2.9.1.1 Gimbaling the Nozzle

In this system of thrust vectoring, the divergent part of a nozzle or the entire nozzle or engine is mounted on a gimbal joint which can move (swivel) around depending on the direction of actuation to deflect the exhaust plume. As the gimbal system is moved from side to side, the thrust of the exhaust plume changes with relative to centre of gravity. The thrust line will be inclined at an angle called gimbal angle “a” as shown in Figure 2.14.

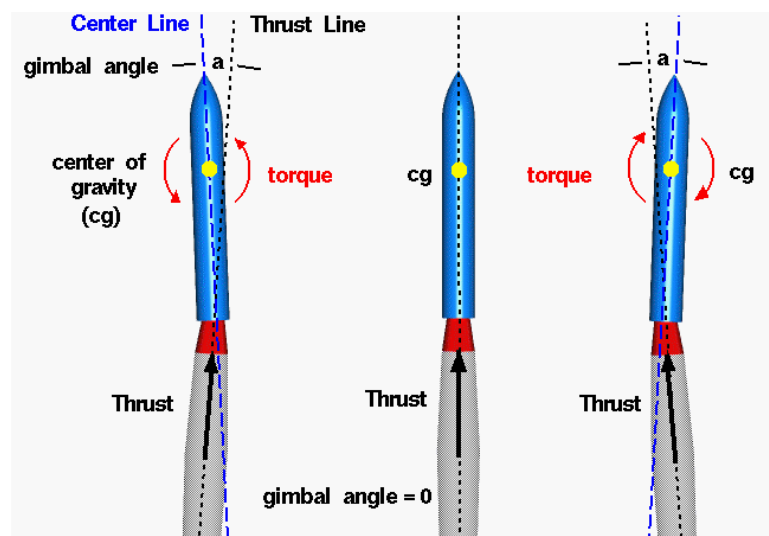


Figure 2.14: Gimbal thrust vectoring system (NASA, n.d.)

2.9.1.2 Vane System

The deflection of the exhaust stream is caused by some vanes mounted at the tip of the nozzle or engine. The diagram of a vane system thrust vectoring is shown in Figure 2.18. The vanes are pneumatically or hydraulically actuated to move in and out of the exhaust stream to cause deflection of the flow away from the centre line.



Figure 2.15: Vane thrust vectoring system (Clarke, 2011)

2.9.2 Fluidic Thrust Vectoring (FTVC)

The deflection of exhaust flow is achieved by injection of secondary airflow to manipulate the primary flow. This has been demonstrated successfully at the laboratory scale. Its advantage over mechanical control is its simple configuration without moving parts, low noise, simplicity, low maintenance costs and lighter weight. However, its challenges lie in ensuring an effective control with a linear response as well as a source of secondary air since overdrawing of secondary air from the primary air supply reduces the engine thrust. The techniques of fluidic thrust vectoring include co-flow, counterflow, shock vector control, throat skewing and synthetic jet actuators.

2.9.2.1 Co-flow Fluidic Thrust Vectoring

Co-flow thrust vectoring is achieved by utilizing the Coanda effect which was named after a Romanian aerodynamics pioneer called Henri Coanda in 1930. **Coanda effect** is the phenomena in which a jet flow attaches itself to the surface and follows the surface curvature and move away from the initial jet direction. The schematic of a co-flow fluidic thrust vectoring is shown in Figure 2.16, and from the schematic, the secondary stream is in the same direction as the primary stream.

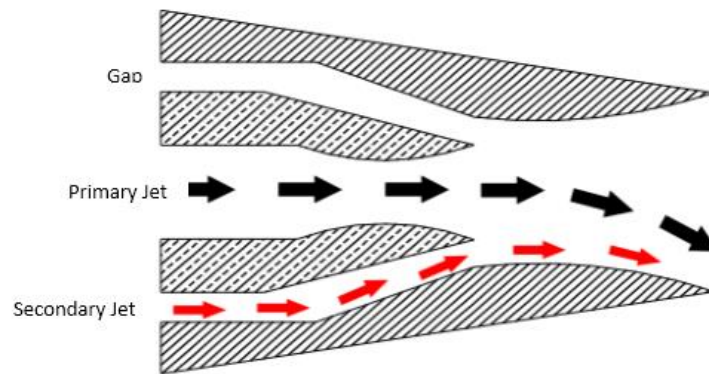


Figure 2.16: The schematic of a co-flow fluidic thrust vectoring (Li, 2011)

2.9.2.2 Counterflow Fluidic Thrust Vectoring

Counterflow technique also uses the Coanda effect in deflecting the primary jet with a secondary jet. This technique was proposed by Strykowski and Krothapali in 1993. Jet deflection can therefore be achieved by fitting a nozzle with a collar leaving a gap between the passage of the secondary stream to create counter flow in the gap between the nozzle jet and the collar, while the secondary jet is introduced opposite the direction of flow of the primary jet. The schematic of the counter flow is shown in Figure 2.17 below.

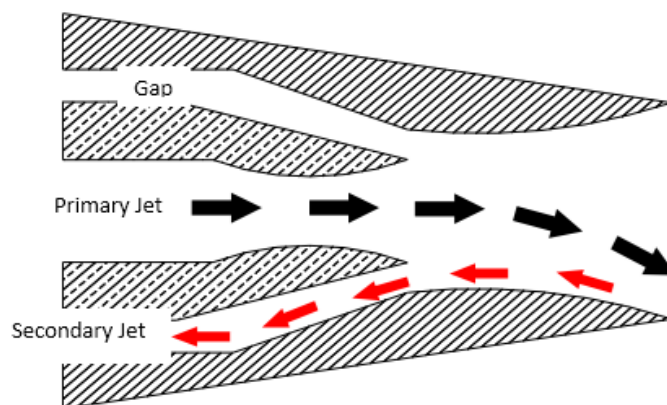


Figure 2.17: Counterflow fluidic thrust vectoring (Li, 2011)

Notably, the potential limitation of the counter flow thrust vectoring system is the possibility of the primary jet attaching to the suction collar that occurs at some certain conditions. This is also notable on various geometric configurations and it has a hysteresis problem as well. However, counterflow shows if the jet attachment can be avoided through good nozzle design

2.9.2.3 Shock Vector Control Fluidic Thrust Vectoring

Shock vector control is achieved by the asymmetric injection of secondary air stream through one of the divergent flaps into the supersonic primary jet. This forms an oblique shock wave within the primary jet and thus deflects the primary jet from its longitudinal flow axis. Furthermore, shock vector control produces a high thrust vector angle, but at a tradeoff of thrust ratio as losses occur when the primary jet interacts with the shock wave, and when the oblique shock created by the injected fluid impinges on the opposite nozzle divergent flap. A schematic of the SVC is shown in Figure 2.18.

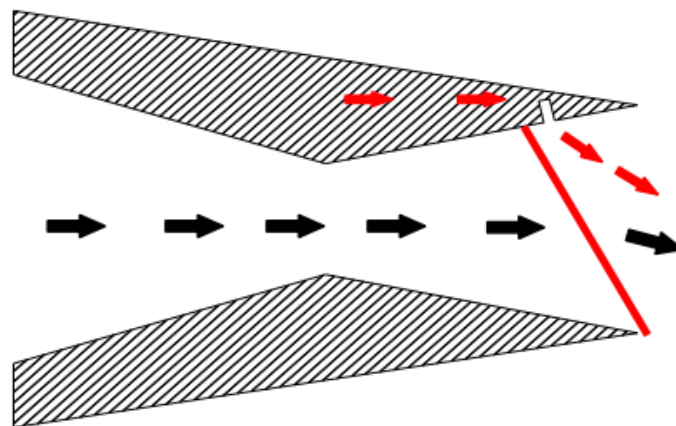


Figure 2.18: Shock wave thrust vectoring system (Li, 2011)

2.10 Advantages and Disadvantages of Thrust Vectoring

2.10.1 Advantages of Thrust Vectoring

There are benefits of incorporating thrust vectoring on an aircraft. These are:

- Increase in aircraft efficiency: Thrust vectoring has been found to be an efficiency improvement facility for an aircraft.
- Low speed manoeuvre capabilities: At the flight regime where low speed flight is inevitable, this is the regime where thrust vectoring plays the most important role - as shown by studies.
- Reduction in size of lifting surfaces: Since vectored thrust from an engine can augment lift from lifting surfaces, the size of the surfaces can be reduced.
- Size reduction or elimination of control surfaces: Thrust vectoring can be used for control, which enables the size of the control to be reduced or even eliminated due to the additional power from the system.
- Expansion of flight control envelope: Thrust vectoring makes manoeuvring of aircraft in the post-stall region possible and at a low speed and high angle of attack flight regime

as it cannot be rendered ineffective as conventional control surfaces. At this point, agility and manoeuvrability are very important.

- Reduction in field length: Thrust vectoring has been found to supplement lift from the lifting surfaces during take-off and landing which enables reduction of the take-off and landing field length.
- Provides manoeuvrability in the post-stalled regime: At flight regime where the control surfaces have stalled, thrust vectoring can become a means of manoeuvrability.

2.10.2 Disadvantages of Thrust Vectoring

The limitations of incorporating thrust vectoring to an aircraft are:

- High cost and complexity: Thrust vectoring systems have a proven complexity problem and high-cost implications.
- Maintenance: The complexity of the existing thrust vectoring system is a concern as it comprises several moving parts - as in the case of multi-axis vectoring systems - which makes its maintenance difficult and costly.
- Systems can be specific in application: Certain thrust vectoring systems cannot work for all purpose aircraft (combat and recreational) configurations. A particular TVC system may be very useful for a combat aircraft but not for a recreational system.
- A robust/complex control system: For thrust vectoring to control aircraft effectively, a complex control system is required to be able to take into account thrust disparities, vectoring requirements, altitude and speed.
- Engine power dependency: Thrust vectoring control power depends wholly or partially on engine power. This can be dangerous when an engine is lost or fails.

The detailed advantages and disadvantages of thrust vectoring are as reported by Clark(2011).

2.11 Analysis of Alternative Thrust Vectoring Control Method

The difficulty in integrating a thrust vectoring system onto a pusher propeller UAV (aircraft) and the effectiveness in directing the thrust from the propeller to the desired directions limits the possibility of developing a pusher propeller aircraft with thrust vectoring capabilities. Considering the small scale of the guardian III UAV which the TVC is being designed for, there are size and weight limitations. These factors must be put into consideration when making a choice as to which configuration should be adopted for this purpose. The available TVC methods were analyzed individually for their operational advantages when used on Guardian III UAV. The higher operational advantage of the configurations are judged based on; lower weight penalty, higher ease integration possibilities, low impact of the configuration on the operational capability of the UAV, and easy maintenance. Based on these criteria, a rating of 1 to 5 was assigned to each of the TVC systems. A rating of 5 means that the system has a

higher operational advantage and stands a higher chance of being used for this purpose. A rating of 1 means the system is not suitable for this application.

The following section gives a detailed explanation and reports on the findings from the careful analysis of the existing TVC configurations.

2.11.1 Gimbaled Engine

In this configuration of thrust vectoring system, the engine is mounted on a universal joint (gimbal system) that allows it to rotate about its axis. The whole engine is swivelled or pivoted on a bearing to direct the thrust to the desired direction as shown in Figure 2.19. Figure 2.20 and 2.21 show its application on an aircraft with jet engines and propeller mount aircraft respectively. As a proven technology from researchers like Wang et al. (2017), who have performed research on using this technology to provide manoeuvring capability on a puller configuration tail-sitter UAV; however, it is known for low torque and small thrust loss, high inertia and requires large manoeuvring power for its high slew rate (Sumathy, 2015). Also, it has a high weight penalty, is complex in design and requires so many actuators for its operation. In the case of a pusher propeller aircraft powered by a piston engine being considered here, the torque generated by swivelling or tilting the engine causes yaw and roll motion (Carstens, 2017). The yaw and roll motion caused requires the rudder to counteract the motion which in some conditions might not have the effectiveness to do so as the thrust vectoring may occur at low speed. Drawing from the analysis, a rating of 2 is assigned to this method – the result being that this method is not suitable for implementation on a piston engine powered aircraft and thrust vectoring application at low speed.

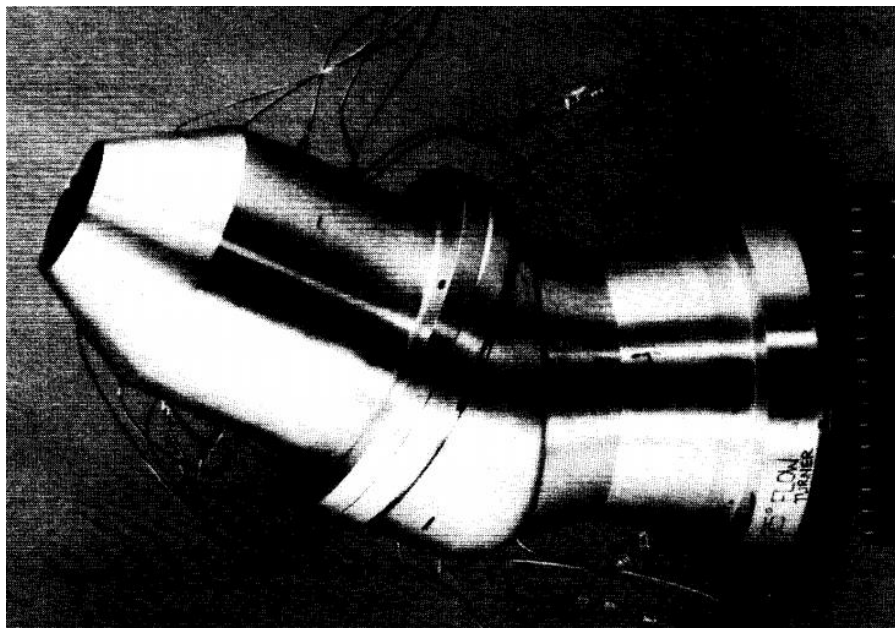


Figure 2.19: Gimbaled thrust vectoring system (Berrier & Taylor, 1990)



Figure 2.20: Gimbaled thrust vectoring system for jet engine aircraft (AviationNepal, 2017)

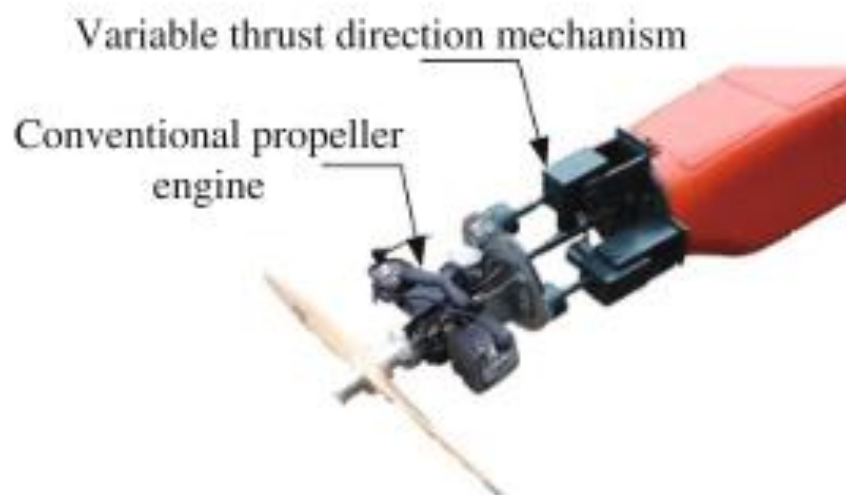


Figure 2.21: Gimbaled thrust vectoring system for jet engine aircraft (Wang & Wang, 2016)

2.11.2 Jetavator

This system has a rotating collar which is shaped like an airfoil. This gives an unsymmetrical distribution of gas flow which provides side forces that change the direction of flight to the desired direction. It looks similar to the jet vanes, however, it is bulky in nature - which leaves it with a heavier weight. The bulky nature hampers its application in the system under consideration as it will increase the overall weight of the system. After a critical study, a rating of 3 is given to this method.

2.11.3 Jet Vanes

These are small airfoils - like shaped vane(s) located at the exit plane of a nozzle (Figure 2.22) which acts like aileron and elevator in an aircraft and causes a change of direction of the vehicle when deflected. Despite little thrust loss and the limited duration of operation due to the erosion caused by hot exhaust gas when used in a jet engine (which does not apply to the case under consideration), the simplicity and lower actuation power make its application easy and profitable (Sumathy, 2015). The ability to incorporate it within a shroud system is another profitable aspect which makes it suitable for pusher propeller aircraft and a shroud system chosen for this work. Due to the suitability of this method, it is given the rating of 4.5

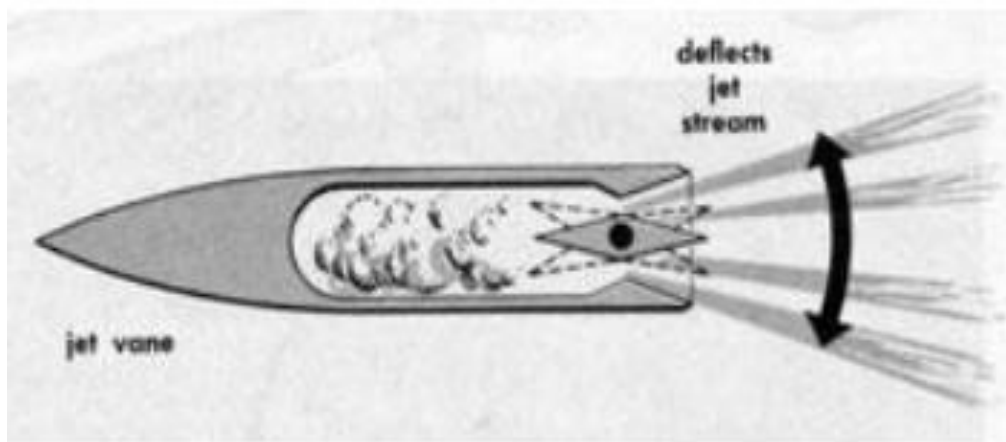


Figure 2.22: Jet vane mechanism (Sumathy, 2015)

2.11.4 Secondary Fluidic Injection FTVCS

As discussed in section 2.9.2, thrust vectoring in this method involves using a jet of secondary fluid to deflect the main exhaust flow from the jet engine. This changes the direction of the primary flow, thereby causing a change of attitude of the aircraft. This can be achieved without movement of any part and therefore makes the operation easy. However, it requires a modification of the existing platform (modification of the engine nozzle to create a cavity for the injection of the secondary fluid) for its integration. Also, to implement this, it will be necessary to install storage tanks for the secondary fluid. This increases the overall weight of the system. When considered for the platform under consideration, its application will not be possible as this is a propeller aircraft and not a jet engine. Therefore, it is given a rating of 1.

Table 2.1: TVCS selection analysis result

TVCS System	Suitability rating
Secondary fluid injection	1
Gimbale	2
Jetavator	3
Jet vanes	4.5

2.12 Optimal Thrust Vectoring Configuration Selection

Based on the study and analysis performed and result summary given in Table 2.1, jet vanes after all consideration shows a better tendency towards good performance on the existing platform of CPUT AMTL guardian III UAV. Therefore, it was chosen by the author as the optimal method suitable for the application under consideration. Hence, all designs for this present work are based on jet vane configuration.

As explained in section 2.11.3, the vanes are airfoil shaped component(s). Some design considerations should be used as a yardstick when selecting the airfoil among the numerous airfoils available in aerodynamic applications. The airfoil to be selected for vane design must meet the design considerations and give the desired result. The processes and analysis involved in the selection of the vane airfoil shape are detailed in section 4.3.1. Also, section 4.3.2 gives details of the process of creating the airfoils selected and the fluid domain needed for the fluent analysis.

2.13 Correlation between Literature Survey and the Current Work

The scope of this research project was to design a thrust vectoring system and to investigate its effect on the pitching control of an aircraft (AMTL Guardian II UAV), to shorten the ground roll and to reduce the overall take-off distance. The second part is to improve the rate of climb thereby increasing the endurance and overall performance of the UAV. The major drawback of the AMTL developed fixed wing UAV is the need for a long runway for its take-off. The singular requirement limitation is its operational long runway for take-off. Therefore, there is a need to reduce the UAV S_g so that it can take off at any available space. This identified limitations motivated this research. This work involves designing a thrust vectoring system to be integrated on the platform to equip it with quick take-off and climb capabilities. The work done by Mair and Edwards (1965), Clarke (2011), and Ikaza (2000b) focused on the reducing the ground roll distance and the aircraft's STOL capabilities through different technological means in combination with TVC system. It can be inferred that their work is mainly on jet engine propulsion system; and closer to the propeller system being investigated in this project is the

work of Akturk and Camci (2010). . Meanwhile, the thrust vectoring method study presented in section 2.11 has shown both possible and suitable method for propeller platform, and also guided the selection process. Furthermore, shroud system (ducted fan) researches presented in section 2.4, have shown the pioneer works done by authors like Berrier and Taylor (1990), Mort and Yaggy (1962), Parlett (1950), and Omics(2014) with the focus on how to enhance propeller performance. Fleming et al. (2003) and Pereira, (2008) and other authors applied ducted fan on UAV to improve its take-off and hovering performance.

Specifically, the work by Vinayagam and Sinha (2014) was selected to guide this work on the rotation of the aircraft to maintain minimum tail clearance during take-off to avoid tail striking on the runway.

The works done by Prasath et al. (2020), Sankar and Sreejith,(2018), Majil (2016b), Živković et al. (2014), Forghany et al. (2018), and Noaman et al.(2019) presented in section 2.5 are a suitable guide to the use of CFD for the investigation of thrust vectoring system.

Taking the work of these researchers further, this work combines their approaches and focus on the use of CFD to design a thrust vectoring technology to enhance pitch control of a pusher propeller UAV operation at any available space.

CHAPTER THREE: TVCS CHARACTERIZATION METHODS

This chapter first presents the preliminary experimental work done to obtain the propeller air velocity and all the test bench design steps and setup. It thereafter discusses CFD theories and all mathematical turbulence model, methods and preliminary CFD studies to ensure accurate setup of the analysis process.

3.1 Experimental Analysis of Propeller Air Velocity

The effective building, modelling and simulation of a thrust vectoring system for a pusher propeller UAV require some operational parameters that matches the design requirements of a shrouded system. This set of data is not readily available because little work has been done in this area. The parameters, therefore, need to be obtained through a laboratory experimental setup that matches the actual system in terms of power and speed.

This experimental setup logs the airspeed along the propeller at a different rotational speed range. To perform this experiment, a test-bench that allows the measurement of the propeller airspeed with the aid of a Pitot tube was designed and manufactured.

The measurement was executed using a Turnigy C6374-200 brushless runner electric motor driving a 20 x10 three-bladed propeller.

3.1.1 Measurement Equipment and Experiment Setup

Figure 3.1 shows a CAD model of the measurement test-bench. The test-bench has the propulsion unit (3) mounted on the bed (2). These two units are mounted on the bench (1). Also fixed on the bench is a shroud (4) which is held rigidly by the bracket (5) to prevent it from vibrating.

The Pitot tube (6) for the air velocity measurement is suspended by a Pitot tube holder (8) and (9) and held tight with a bolt (10) to avoid it sliding down. The Pitot tube holders which are threaded rods are fastened on a hanger which is fixed on the shroud by welding it with the aid of two nuts (7). On the hanger are holes of 12 mm drilled at a distance of 15 mm centre to centre which is used to control the uniform distance from the tip of the propeller as the Pitot tube is lowered through to the centre of the propeller during the experiment.

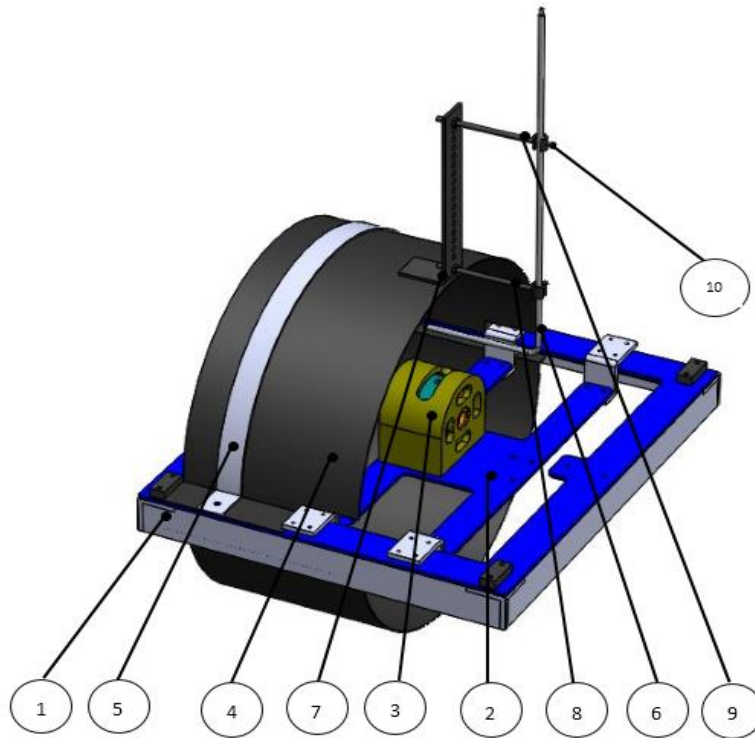


Figure 3.1 Velocity profile experiment model

The setup is designed in such a way that the Pitot tube stagnation point is directly facing the airflow from the propeller. The measurement is done by adjusting the Pitot tube from a point close to the tip of the propeller through to the centre of the propeller using the holes drilled at an equi-distance from each other on the hanger. Pitot tube holder (8) is meant to be stationary while Pitot tube holder (9) will be moved from one hole to another starting from top to bottom of the hanger.

The experiment setup is also equipped with other gadgets as shown in Figure 3.2. The control and logging unit (11) which logs the measurement onto a data storage device is connected to a remote data unit (RDU) (12) which measures the voltage and current of the system. Electronic speed controller (13) connects to the RDU and receives the throttle position as a pulse width drive from the control and logging unit. Two 5 cell 5000mAh lipo battery (15) are connected in series to power the propulsion unit. Pitot tube manometer (14) which connects through two transparent hose (tube) to the Pitot tube - it reads and logs the airflow velocity along the length of the prop. Other views of the experimental setup are shown in Figure 3.3 and Figure 3.4

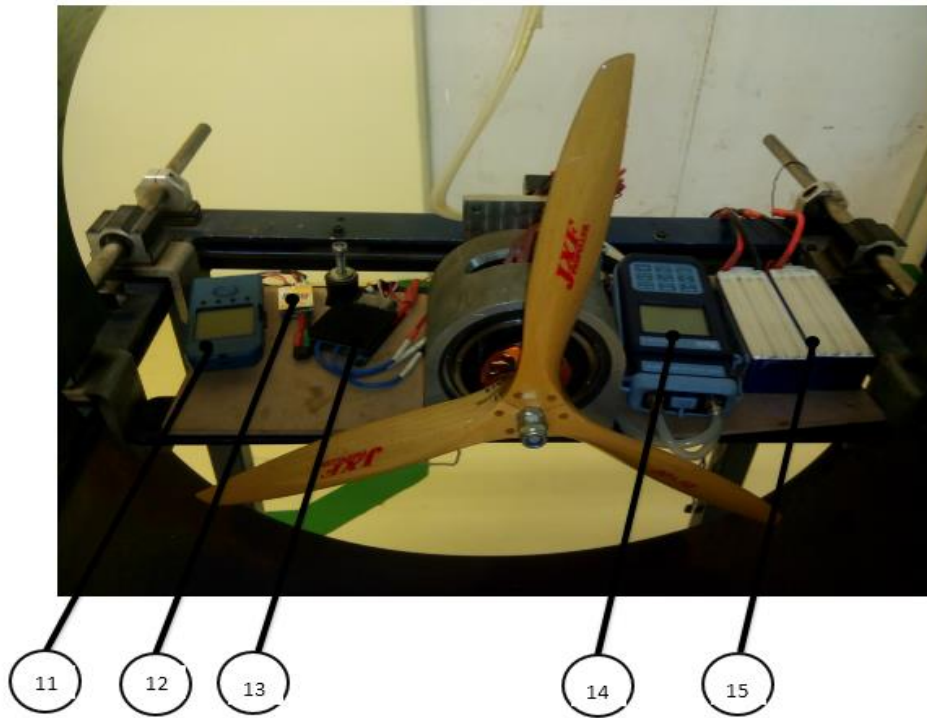


Figure 3.2: Velocity profile experiment test bench



Figure 3.3: Velocity profile experiment full setup



Figure 3.4: Velocity profile experiment setup - Side view

The experiment setup measures the air velocity of a spinning propeller from 1000 rpm up to 4000 rpm along the length of the prop from 0 – 180 mm at intervals of 15mm starting from the tip through to the center of the prop. The propeller can be either two or three blades mounted on either an internal combustion engine or electric motor. For an internal combustion engine propelled setup, the Pitot tube should be mounted on a holder isolated from the test bench as the vibration from the engine transferred to the test bench will not allow a stable flow of air into the Pitot tube, which also vibrates and will therefore cause the manometer to give reading. Due to the vibrational problem associated with the use of an internal combustion engine, an electric motor was used for the experiment and because the electric motor runs smoothly and is void of vibration, the Pitot tube was mounted directly on the shroud. The result of the experiment is illustrated on the distance versus velocity curve shown graphically in Figure 3.5, and the tabular result is presented in Appendix A. It can be deduced from the result that the air velocity along the blade of a spinning propeller is not uniform, and the airflow pattern is parabolic - that is, the air velocity at the tip and the core of the propeller are the same. The propeller has its maximum air velocity at its mid-distance.

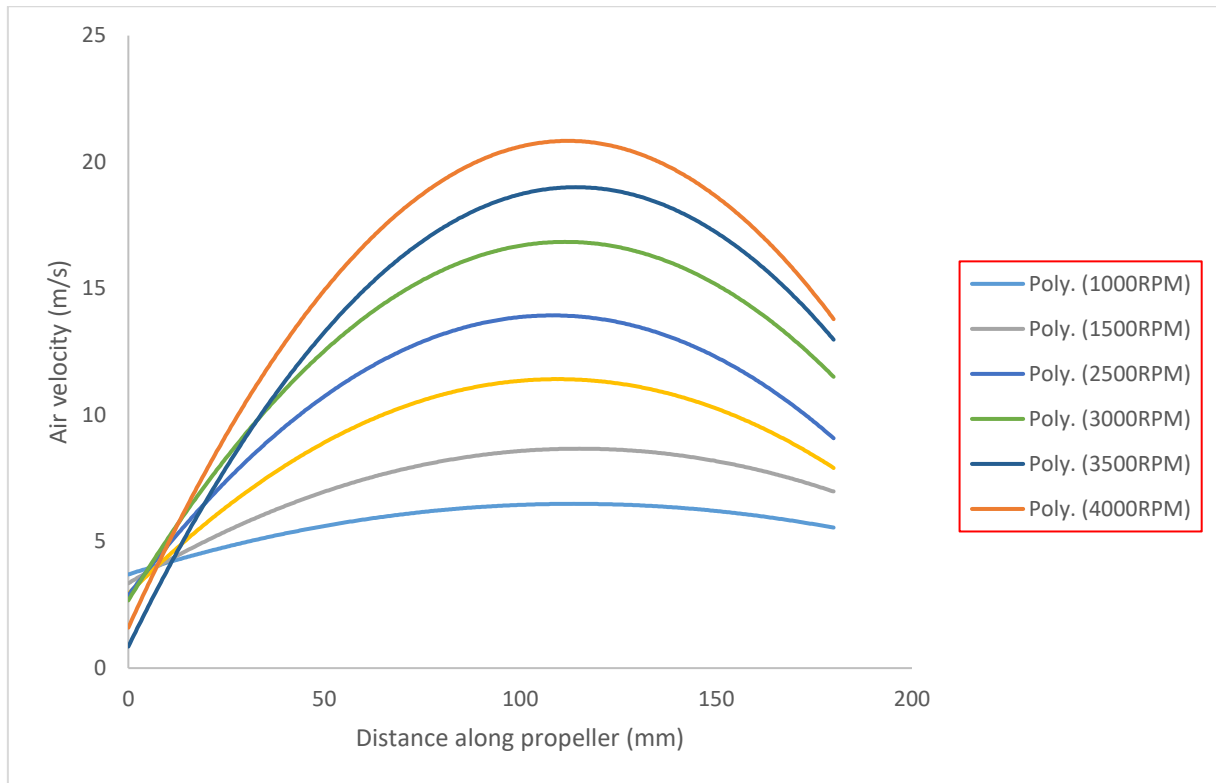


Figure 3.5: Velocity profile experiment

3.2 Numerical Solution Methods

3.2.1 Introduction

Computational Fluid Dynamic (CFD) is a computational method used for the simulation of heat transfer, Laminar and turbulence flow as well as the reactions of different substances. It is used by industries and researchers to proffer a solution to industrial related problems. It tackles the energy, mass and momentum equation of any geometry of choice. CFD is used in all stages of the engineering process, conceptual studies of new designs, detailed product development, optimization, troubleshooting, and revamping. CFD analysis compliments testing and experimentation by reducing total effort, time and cost required for experimentation and data acquisition.

CFD is applied extensively to solve diverse engineering problems. The aerodynamic design in aeronautical engineering these days is greatly influenced by CFD which shortens the design cycle, reduces prototyping, and improves aerodynamic properties. Furthermore, CFD is employed in the work under investigation to simulate flow effects around the vane using ANSYS FLUENT 2019R, while the flow parameters of interest are monitored during the simulation and compared with the experimental values. If it agrees with the experimental result, the simulated result will be accepted, otherwise, modifications will be made to the design or the mesh and then re-simulated. This is done until an acceptable result is achieved. By simulating until optimal result is obtained, less time is spent and lower cost is incurred when

compared to the time consumed in system construction, cost of material (wasted and used) and experimentation time.

The numerical approach in ANSYS processes is divided into three stages namely pre-processing, fluent simulation (solver), and post processing. The pre-processing stage involves developing the model on which the analysis is to be carried on in ICEM or in design modeler. The geometry can be created using any cad application (in this work, Solidworks is used) and then imported into ANSYS analysis package. When the establishment of the geometry is complete, a fluid or computational domain is created around the geometry at defined distances. The computational domain is discretized into a finite set control volume forming quadrilateral or triangular cells in 2D or tetrahedral or hexagonal cells in 3D which establishes grids or mesh. After meshing, boundaries such as inlet, outlet and walls are defined within the automatic mesh generator. The ready mesh is then imported into ANSYS FLUENT 2019R for fluid flow solution analysis which is generated at cell points. After the solution simulation, the results are analysed in ANSYS postprocessing. At this stage, the velocity and pressure contours as well as the other flow parameters result are generated, graphs plotted or exported to other file formats.

3.3 Governing Equations of Fluid Flow

CFD governing equation of fluid dynamics (continuity equation, momentum and energy equation) describing the flow behaviour of a Newtonian fluid are based on three physical phenomena namely mass conservation, newton's second law and energy conservation (Anderson, 1995).

3.3.1 Continuity Equation

The physical statement of the continuity equation is that no mass is lost throughout the control volume. That is mass flow into a control volume is equal to mass flow out of the control volume. The mass conservation equation is written as:

$$\frac{\partial \rho}{\partial t} + \frac{\partial(\rho u)}{\partial x} + \frac{\partial(\rho v)}{\partial y} + \frac{\partial(\rho w)}{\partial z} = 0 \quad \text{Equation 3.1}$$

3.3.2 Momentum Equation

The momentum equation is obtained from Newton's second law; the net force on a fluid element equals the mass times the acceleration of the element.

$$F = ma \quad \text{Equation 3.2}$$

Based on the left-hand side of this equation, we can deduce that the moving fluid experiences some forces in different directions. There are two sources of force experienced by the fluid; the body force and surface force. Body forces are electrical, gravitational and magnetic and they act directly on the control volume, while surface forces are pressure, shear and normal

forces which act on the surface of the fluid. The vector relation of Newton's second law can be split into three scalar relations along the x, y and z directions and the momentum equation along these various directions are written as:

X- Momentum Equation

$$\frac{\partial}{\partial t}(\rho u) + \frac{\partial}{\partial x}(\rho uu) + \frac{\partial}{\partial y}(\rho vu) + \frac{\partial}{\partial z}(\rho wu) = -\frac{\partial P}{\partial x} + \mu \left(\frac{\partial^2 u}{\partial x^2} + \frac{\partial^2 u}{\partial y^2} + \frac{\partial^2 u}{\partial z^2} \right) \quad \text{Equation 3.3}$$

y- Momentum Equation

$$\frac{\partial}{\partial t}(\rho v) + \frac{\partial}{\partial x}(\rho uv) + \frac{\partial}{\partial y}(\rho vv) + \frac{\partial}{\partial z}(\rho wv) = -\frac{\partial P}{\partial y} + \mu \left(\frac{\partial^2 v}{\partial x^2} + \frac{\partial^2 v}{\partial y^2} + \frac{\partial^2 v}{\partial z^2} \right) - \rho g \beta (T_\infty - T)$$

Equation 3.4

Z-Momentum Equation

$$\frac{\partial}{\partial t}(\rho w) + \frac{\partial}{\partial x}(\rho uw) + \frac{\partial}{\partial y}(\rho vw) + \frac{\partial}{\partial z}(\rho ww) = -\frac{\partial P}{\partial z} + \mu \left(\frac{\partial^2 w}{\partial x^2} + \frac{\partial^2 w}{\partial y^2} + \frac{\partial^2 w}{\partial z^2} \right)$$

Equation 3.5

3.4 Turbulence Modelling (TM)

Virtually all real engineering flow and flows in nature are turbulent, hence researchers in computational fluid dynamics do not focus on flows where turbulence is predominant such as the case under investigation. Even though the precise physical disposition of turbulence is yet to be fully appreciated, it has for the mean time been numerically modelled to high level of accuracy through simulation by applying some developed numerical approaches (Zhiyin, 2015). These numerical approaches resolve the flow turbulence to a different degree of accuracy. The overall goal is to have a controllable or manageable quantitative postulations (model) to be implemented in calculating important quantities which are of interest to the engineering (or other fields) community (Pope, 2000). The different available approaches are direct numerical simulation (DNS), large eddy simulation (LES) and Reynolds average Navier-Stock (RANS) model. These approaches are discussed below.

3.4.1 Direct Numerical Simulation (DNS)

Resolving Navier-Stock equation to predict turbulence to a high degree of accuracy, to date has only been done using DNS. DNS tackles turbulent resolution through closed mathematical formulations that gives no room for empirical input (Prez-Segarra et al., 2009). It resolves all timescales and length scales in Navier-Stock equation to obtain the direct velocity field $U(x, t)$ for one realization of the flow. By so doing, it incurs a lot of computer costs which increases as the Reynolds number increases in the order of Re^3 . The computational time expended on DNS

simulation is directed towards resolving the dissipative rate (motion) of small eddies of the turbulence whereas the energy of the flow is predominantly in the large-scale eddies. The computationally expensive nature of this method makes its application limited to flows of moderate and low Reynolds number. It would have been the pleasure of the author to completely determine or resolve all the turbulent quantities surrounding the case under investigation by applying a direct numerical simulation (DNS) approach, however computer resources available made it impossible.

3.4.2 Large Eddy Simulation (LES)

Turbulence are made up of large eddies which disintegrate into smaller eddies during flow phase. On seeing the computational demand of DNS and limitations of RAN, Smagorinsky in 1963 proposed an approach which compute explicitly the dynamics of the large eddies motions and only modeled the small-scale motions (small eddy), hence his approach adopted the name large-eddy simulation (LES). It decomposed the velocity field $U(x, t)$ through a filtering into a component $\bar{U}(x, t)$ and a sub-grid scale (residual component) $u'(x, t)$, to capture the full sense of large-eddies. By so doing, the computational requirement of the DNS was reduced by removing the cost of catering for dissipative motion of the entire flow. This approach presents a more accurate result of turbulence resolution than RANS by resolving completely the large scale motion (large eddies) which account for the major turbulent energy transfer and is accountable for the momentum transfer as well as turbulent mixing (Pope, 2000; Zhiyin, 2015). It although incurs less computational cost than DNS, it is still far beyond the computational resources available for this work.

3.4.3 Reynolds Average Navier-Stock Models (RANS)

The major motive behind RANS is the decomposition of the instantaneous quantity (velocity field) as contained in Navier-Stock equation into its time-averaged and fluctuating quantities. The rest of the turbulent motions are then modeled using turbulent model. The approach is aimed at solving the steady state of fluid flows, hence it does not require complete simulation of the turbulent quantities. In this case therefore, both the large scale and the small-scale motions are modeled thereby buying lots of computing time and cost. This approach to a large extent has been the pillar of industrial CFD applications for a few decades now due to its cheap computational requirement.

Notably, turbulent modelling (TM) – is an approach which denotes the construction and the use of models to predict the effect of turbulence in a fluid flow. Due to the computational expense of the direct numerical simulation (DNS) and the large eddy simulation (LES), averaging is mostly used to reduce the governing equation to a simple form which is computationally manageable (Sharafani, 2015). This work like every other industrial and research problem with limited resources employed the RANS approach of using turbulent model as a closure to predict the flow characteristics of this investigation.

The eddy viscous turbulent models as contained in RANS approach are grouped based on the number of equations they tend to solve. There are zero, one, two and seven equation models. But for this work, only two equation models which are relevant will be discussed. These are discussed in the following section.

3.4.3.1 Two Equation Models

This is one of the most common types of turbulence models widely used by industrialist and researchers in different fields ranging from engineering, sciences and even medical and bio-medical fields. They execute their activities by solving two transport equations in order to properly represent properties of turbulent flows. They usually solve the turbulent kinetic energy equation k and turbulent dissipation ε or specific turbulent dissipation ω . The models are coined from turbulent kinetic energy equation k and either turbulent dissipation ε or specific turbulent dissipation ω equations which they solve. The first variable, k making up the model determines the energy in the turbulence while the second variable (ε or ω) determines the scale of the turbulence (length scale or time scale) (CFD-online, 2017).

The two common equation models available for CFD simulation are:

- k -Epsilon model (k - ε)
- k - Omega model (k - ω)

K- ε Model

This model was firstly proposed in 1972 by Jones and Launder (Jones & Launder, 1972). Today, it is the most popular model being used in ANSYS-FLUENT. There are three types of the K- ε model, namely the standard, the Re-normalization group (RNG), and the Realizable model.


Standard K-Epsilon Model (Sk- ε)

This solves the two transport equations (turbulent kinetic energy equation k , and turbulent dissipation equation ε) by determining the value of μ_t .


Turbulent Kinetic Energy (k - transport equation). The equation for turbulent kinetic energy is as follows:

$$\rho \frac{Dk}{Dt} = \frac{\partial}{\partial x_j} \left[\left(\mu + \frac{\mu_t}{\sigma_k} \right) \frac{\partial k}{\partial x_j} \right] + \mu_t S^2 - \rho \varepsilon$$

Equation 3.6



Production



Dissipation

Where $S = \sqrt{2S_{ij}S_{ij}}$

Turbulent Dissipation Equation (ε -transport equation):

$$\rho \frac{D\varepsilon}{Dt} = \frac{\partial}{\partial x_j} \left[\left(\mu + \frac{\mu_t}{\sigma_\varepsilon} \right) \frac{\partial \varepsilon}{\partial x_j} \right] + \frac{\varepsilon}{k} (C_{i\varepsilon} \mu_t S^2 - \rho C_{2\varepsilon} \varepsilon) \quad \text{Equation 3.7}$$

Inverse time scale

$\sigma_k, \sigma_\varepsilon, C_{i\varepsilon}, C_{2\varepsilon}$ are constants with $\sigma_k = 1.0, \sigma_\varepsilon = 1.2, C_{i\varepsilon} = 1.44, C_{2\varepsilon} = 1.9$

Turbulent viscosity $\mu_t = \rho C_\mu \frac{k^2}{\varepsilon} \quad C_\mu = 0.09$

Standard k-epsilon model is known for its simplicity, its ease to converge and its good prediction for many flows, but it is also characterised by some limitations which makes the application limited in some areas. The limitations are poor predictions for swirling and rotating flows, flows with strong separation, axisymmetric jets, certain unconfined flows, and fully developed flows in non-circular ducts, spreading rate of round jet prediction is inaccurate, and its validity for only fully turbulent flows.

Additionally, k-epsilon model has been improved in several ways in order to tackle the limitations of the standard model and improve its performance. The improved versions of the model are RNG k-epsilon model and Realizable k-epsilon model.

RNG K-Epsilon Model

The transport equation for k and ε are basically the same as that of standard k - ε model, but the model constants differ in the turbulent dissipation where $C_{1\varepsilon}$ is replaced with $C_{1\varepsilon RNG}$. The model is based on renormalization group method of Navier-Stokes equations. The turbulent dissipation equation for RNG k - ε becomes:

$$\frac{\partial(\rho\varepsilon)}{\partial t} + \frac{\partial}{\partial x_j} (\rho U_j \varepsilon) = \frac{\partial}{\partial x_j} \left[\left(\mu + \frac{\mu_t}{\sigma_{\varepsilon RNG}} \right) \frac{\partial \varepsilon}{\partial x_j} \right] + \frac{\varepsilon}{k} (C_{\varepsilon 1 RNG} P_k - C_{\varepsilon 2 RNG} P_\varepsilon) + C_{\varepsilon 1 RNG} P_{\varepsilon b}$$

Equation 3.8

Where $C_{\varepsilon 1 RNG} = 1.42 - f_\eta$ and $f_\eta = \frac{\eta(1-\frac{\eta}{4.38})}{(1+\beta_{RNG}\eta^3)}$, $\eta = \sqrt{\frac{P_k}{\rho C_{\mu RNG} \varepsilon}}$

$$C_{\varepsilon 2RNG} = 1.68$$

Furthermore, RNG k-epsilon model has a lot of improvement from the standard k-epsilon model in the areas of handling swirling and rotational flow, improved prediction of high streamline curvature and strain, transitional flows as well as wall heat and mass transfer. Despite all these advantages, the limitation is its inaccurate prediction of spreading of a round jet.

Realizable K-epsilon Model

Realizable k-epsilon model contains a new formulation for turbulent viscosity and a new transport equation for dissipation rate ε has been derived from the known standard transport of the mean-square vorticity fluctuation. It shares the same turbulent kinetic equation with the standard k-epsilon model. The transport equation for realizable k-epsilon model for modeled transport equation for k and ε is as follows:

$$\frac{\partial}{\partial t}(\rho k) + \frac{\partial}{\partial x_j}(\rho k u_j) = \frac{\partial}{\partial x_j} \left[\left(\mu + \frac{\mu_t}{\sigma_k} \right) \frac{\partial k}{\partial x_j} \right] + G_k + G_b + \rho \varepsilon - Y_M + S_k \quad \text{Equation 3.9}$$

And

$$\frac{\partial}{\partial t}(\rho \varepsilon) + \frac{\partial}{\partial x_j}(\rho \varepsilon u_j) = \frac{\partial}{\partial x_j} \left[\left(\mu + \frac{\mu_t}{\sigma_k} \right) \frac{\partial \varepsilon}{\partial x_j} \right] + \rho C_1 S_\varepsilon - \rho C_2 \frac{\varepsilon^2}{k + \sqrt{\nu \varepsilon}} + C_{1\varepsilon} \frac{\varepsilon}{k} C_{3\varepsilon} G_b + S_\varepsilon$$

(Sharcnet, 2006)

Equation 3.10

Where

$$C_1 = \max \left[0.43, \frac{\eta}{\eta + 5} \right], \quad \eta = S \frac{k}{\varepsilon}, \quad S = \sqrt{2 S_{ij} S_{ij}}$$

Where, G_k represents the generation of turbulence kinetic energy due to the mean velocity gradients, G_b is the generation of turbulence kinetic energy due to buoyancy, Y_M is the contribution of fluctuating dilation in compressible turbulence to overall dissipation rate, C_2 and $C_{1\varepsilon}$ are constants. σ_k and σ_ε are the turbulent prandtl numbers for k and ε , S_k and S_ε are user-defined source terms.

Realizable k-epsilon model has proven to be better than standard k-epsilon model after validation in so many ways. The model accurately predicts rotating homogenous shear flows, channel and boundary layer flows, separated flows and spreading rate of axisymmetric jets as well as planar jets.

K-Omega (ω) Model

$k - \omega$ model was formulated based on turbulent kinetic transport equation k and specific turbulent dissipation transport equation ω . It was developed by Wilcox and his group in 1988. $K-\omega$ model is significantly more computationally accurate than $k-\epsilon$ in the near wall layers. It has recorded a success in flow that has to do with moderate adverse pressure gradient and has been found to be widely used in industrial application as well as for research purposes. The limitations of this model is its failure to accurately predict flow with pressure induced separation (Kayne & Agarwal, 2013; Menter et al., 2003). The transport equations are given as:

$$\frac{\partial}{\partial t}(\rho k) + \frac{\partial}{\partial x_j}(\rho U_j k) = \frac{\partial}{\partial x_j} \left[\left(\mu + \frac{\mu_t}{\sigma_k} \right) \frac{\partial k}{\partial x_j} \right] + P_k - \beta' \rho k \omega + P_{kb} \quad \text{Equation 3.11}$$

$$\frac{\partial}{\partial t}(\rho \omega) + \frac{\partial}{\partial x_j}(\rho U_j \omega) = \frac{\partial}{\partial x_j} \left[\left(\mu + \frac{\mu_t}{\sigma_\omega} \right) \frac{\partial \omega}{\partial x_j} \right] + \alpha \frac{\omega}{k} P_k - \beta \rho \omega^2 + P_{\omega b} \quad (\text{Sharcnet, 2015})(\text{Michalcová et al., 2017})$$

Equation 3.12

$$\text{Where } \beta' = 0.09, \alpha = 5/9, \beta = 0.075, \sigma_k = 2, \sigma_\omega = 2$$

k- ω SST Model

The shear stress transport (SST) k-omega model takes care of the turbulent shear stress with a high accurate prediction of onset and amount of flow separation under adverse pressure gradient on a smooth surface. It was developed by Menter in 1994 (Menter, 1994). The turbulence kinetic energy k and the specific dissipation rate ω are obtained from the following transport equations:

$$\frac{\partial}{\partial t}(\rho k) + \frac{\partial}{\partial x_i}(\rho k u_i) = \frac{\partial}{\partial x_j} \left(\Gamma_k \frac{\partial k}{\partial x_j} \right) + G_k - Y_k + S_k$$

Equation 3.12

$$\frac{\partial}{\partial t}(\rho \omega) + \frac{\partial}{\partial x_i}(\rho \omega u_i) = \frac{\partial}{\partial x_j} \left(\Gamma_\omega \frac{\partial \omega}{\partial x_j} \right) + G_\omega - Y_\omega + S_\omega$$

Equation 3.13

Where G_k represents generation of turbulence kinetic energy due to mean velocity gradients. G_ω represents the generation of ω . Γ_k , and Γ_ω represents the effective diffusivity of k and ω . Y_k , and Y_ω represents the dissipation of k and ω due to turbulence. S_k and S_ω are user-defined source terms.

The choice of the model employed in this work was based on the computing resources available and the nature of the analysis. The analysis is an aerodynamic flow over vanes which is characterized by flow separation at a certain angle of vane deflection and adverse pressure gradient, k-epsilon realizable model has the potential to give a good prediction of the problems when coupled with its wall function. In order to fully capture the flow characteristics in these conditions mentioned, Menter in his work in 1993 developed k – omega model to take into account all the limitations of k-epsilon model. The k – omega model was therefore regarded as an upgrade of k-epsilon model in that it gives good flow characteristics prediction in conditions where these two possibilities may arise. After due study and consideration of all available models, k – omega model was chosen by the author as the choice model to be used for this work since it is more likely to produce a better result.

3.5 CFD Preliminary Study

To ascertain the suitability of the CFD approach to give good result, constant adjustment studies was performed. Constants are terms which enable the K-Omega model through the turbulent kinetic energy and specific dissipation rate equation to solve the RANS equation in order to proffer a solution to flows with moderate adverse pressure gradients. They also predict more accurately than k-ε in the near wall layers (Menter et al, 2003). The constant (ALPHA*_INF, ALPHA_INF, BETA*_INF, BETA_INNER and BETA_OUTER) was adjusted by increasing or decreasing the value to see the effect that they will have on the overall result of the simulation, convergence time and the residual. The report of the studies of the effects adjusting the constants will have on the analysis is given below:

Alpha*_Inf

Increment and decrement of this constant show the same trend of the effect on the result of the analysis. The constant decreases the result of the simulation by 1.345 percent and the

percentage increases as the constant value adjustment gets bigger or smaller. Figure 3.6 and Figure 3.7 below show the simulation result (lift Coefficient and drag coefficient) of increasing the constant by an increment of 10 percent and later at 20 percent. The graph shows the CL and CD versus the constant values. Altering this constant also extends the convergence time of the simulation from 542 iterations to 552 iterations but the residual was dropped from 10^{-4} to 10^{-7} .

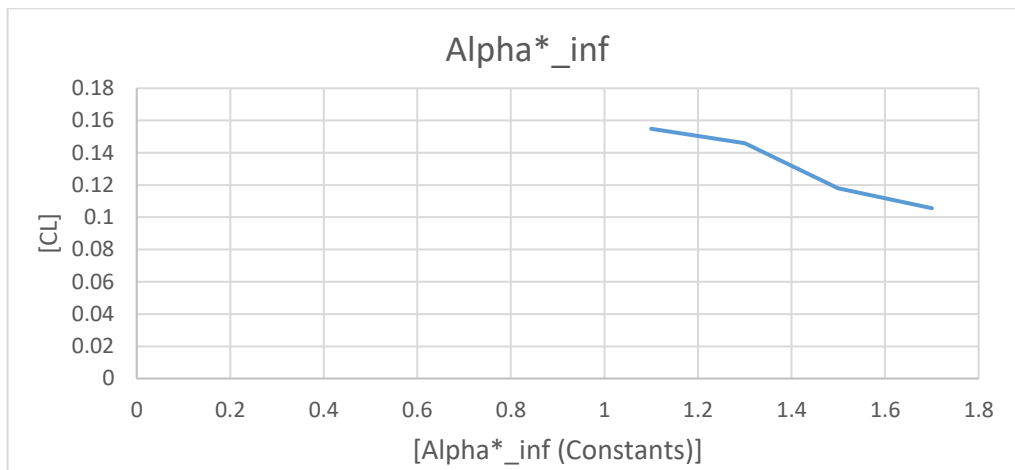


Figure 3.6 Varying Lift coefficient at Alpha*_inf constant adjustment

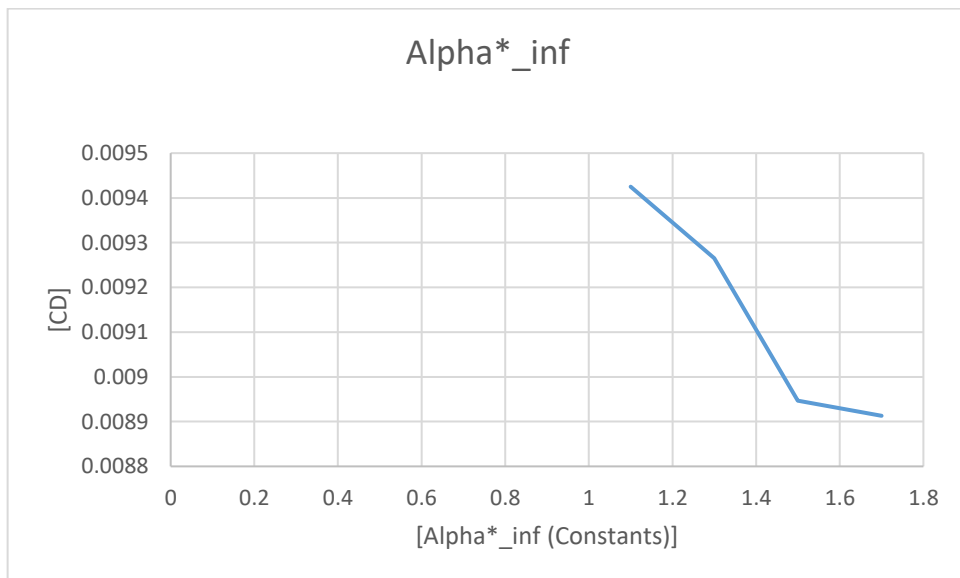


Figure 3.7: Varying Drag coefficient at Alpha*_inf constant adjustment

Alpha_Inf

Adjusting this constant has no effect on the analysis result in terms of the value of the CL and CD, but it only extended the convergence time and dropped the residual to below 10^{-7} .

Beta*Inf

Adjusting this constant made the simulation unstable. The value of the CL and CD kept increasing and decreasing but was still below the simulation result when the constants are intact. It also extends the convergence time and drops the residual. Figure 3.8 shows the result of the analysis when the beta constant was adjusted. The graph also shows the behaviour of the simulation.

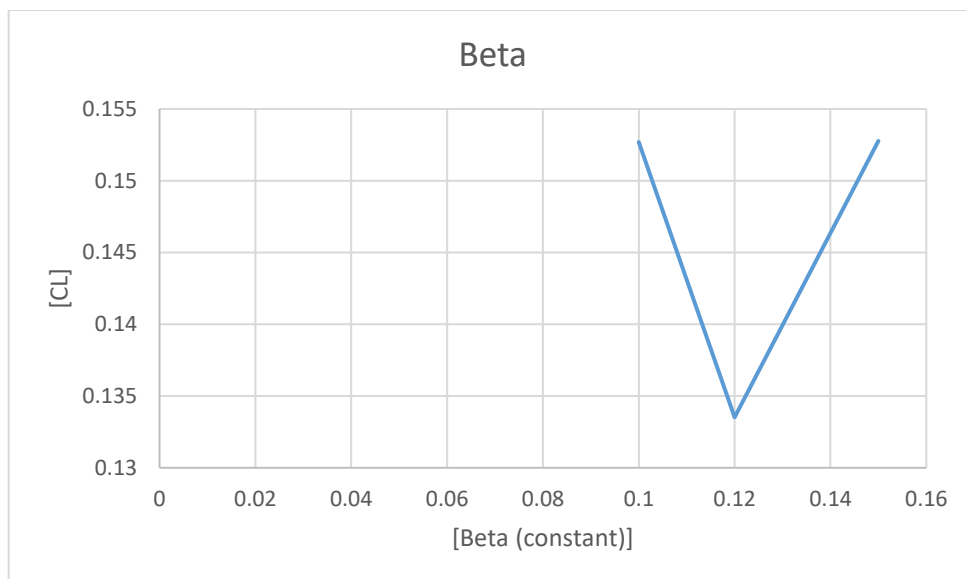


Figure 3.8: Varying Lift coefficient at Beta*inf constant adjustment

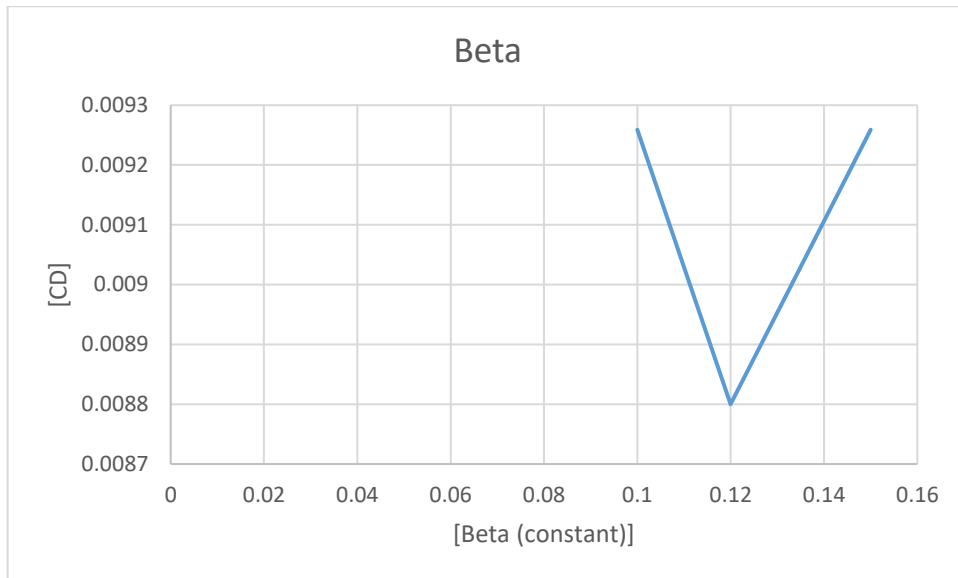


Figure 3.9: Varying Drag coefficient at Beta*inf constant adjustment

Beta_Inner

This is one of the constants which when adjusted affects the overall result of the analysis. Increasing this constant by approximately 19% reduces the final result of the simulation in terms of the value of CL and CD by 0.828%, however decreasing it by approximately 73%, increases the final result significantly by 2.3% as shown in Figure 3.10 and Figure 3.11. After the level of increment, any further increment reduces the result. Furthermore, adjusting beta inner also extends the convergence time of the simulation but drops the convergence residual.

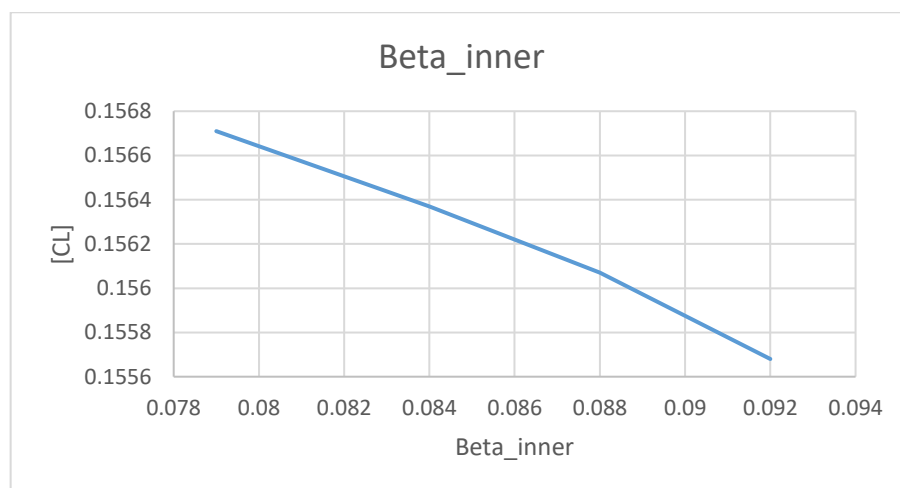


Figure 3.10: Varying Lift coefficient at Beta_inner increases constant adjustment

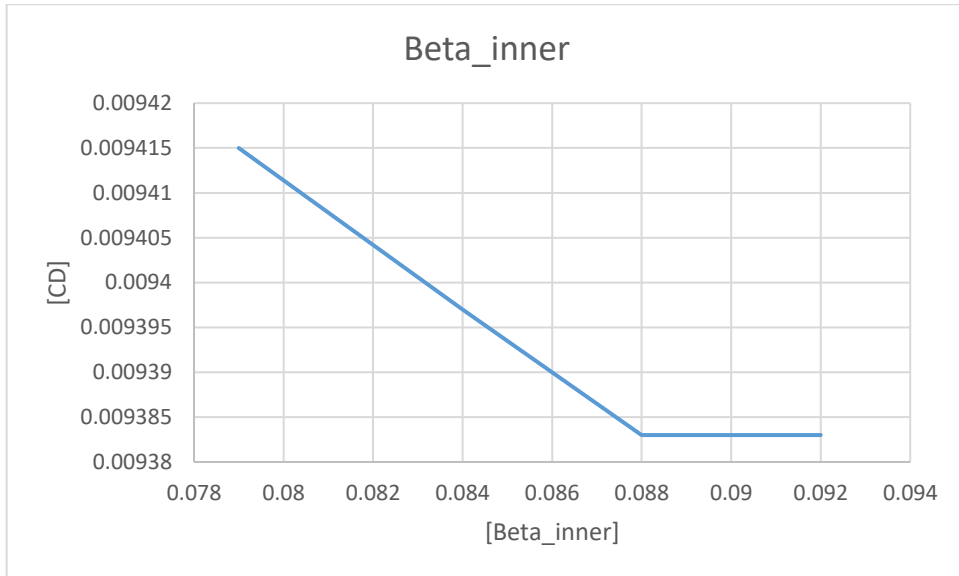


Figure 3.11: Varying Drag coefficient at Beta_inner increases constant adjustment

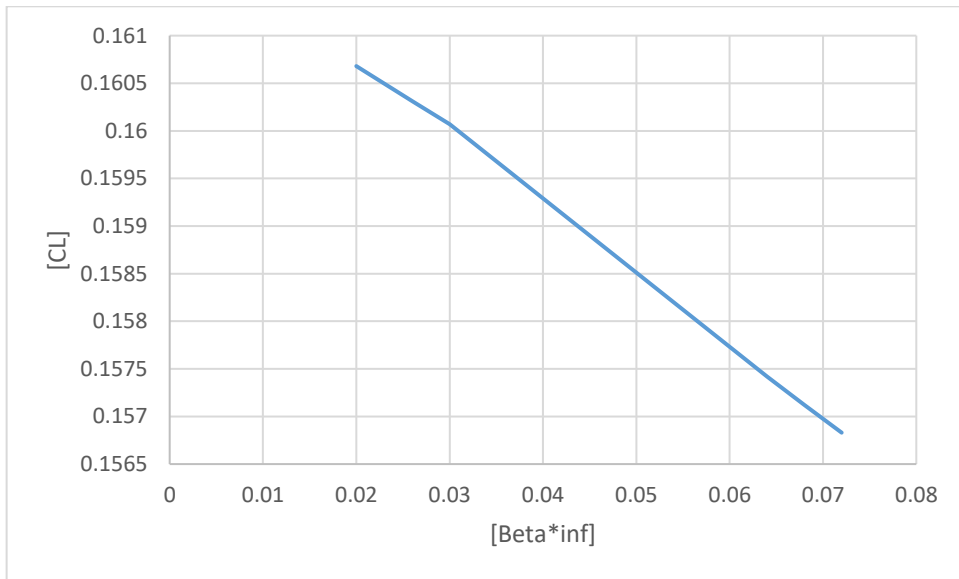


Figure 3.12: Varying Lift coefficient at Beta*inf decreasing constant adjustment

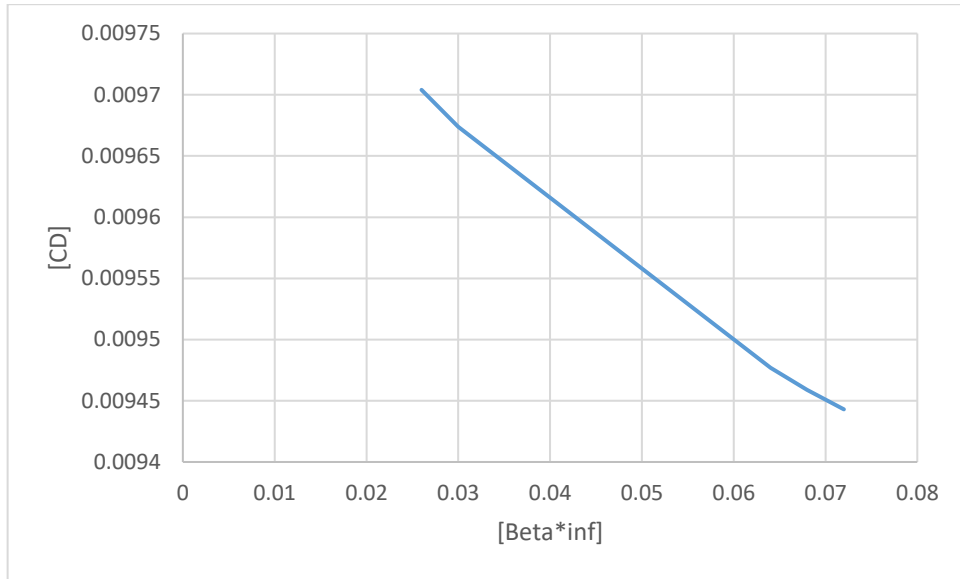


Figure 3.13: Varying Drag coefficient at Beta*inf increasing constant adjustment

CHAPTER FOUR: AERODYNAMIC THRUST VECTORING SYSTEM CONCEPTUAL DESIGN

This chapter first explains the selection process to obtain the suitable airfoil used for the design of the vanes. It also presents the TVCS CAD model, the description of the component parts of the system, and the computational domain creation using Solidworks.

4.1 Optimal Airfoil Selection and Design

Among the different airfoil shapes available, three NACA four-digit series symmetrical airfoils were selected for analysis. It is author's desired operational characteristics that the thrust vectoring system for this work produces no lift at zero deflection angle. The lift can only be expected when the vanes are vectored to a certain angle. Zero lift at zero vane deflection angle influences the author's choice to only analyze symmetrical airfoils. Several symmetrical airfoils are available in practice and this places demand for a careful selection from the numerous airfoils in order to achieve optimum performance from the system.

The selection criteria were based on section lift, section drag and section drag polar at a different vane deflection angle and physical dimensions. The process considers the effects of thickness on the lift and drag characteristics of different airfoil.

4.1.1 Optimum Airfoil Selection

Three randomly selected NACA airfoils (0006, 0012, and 0016) were characterized using the two-dimensional ANSYS FLUENT 2019R compressible flow code. A typical CFD analysis process was followed in performing this study, namely: geometry design, fluid domain creation, mesh generation and flow analysis. The aim of this process is the selection, among available airfoils, to give optimum performance for the purpose for which we are carrying out this investigation.

The geometric properties of NACA airfoils used in the study was generated from the NACA standard airfoil data generator, a designated website used to generate different airfoil geometric data points (Airfoiltools, n.d.). The generated data points were copied to excel for formatting to a form acceptable by ANSYS workbench. The formatted points were imported into ANSYS design modeler where it was transformed into curves forming the shape of the airfoil as shown in Figure 4.1. After the curves were generated, a C-shape fluid domain shown in Figure 4.2 was created around the airfoil with dimensions big enough to handle the wake and flow effect at the outlet boundary to avoid reverse flow. The inlet boundary (left of the leading edge of the airfoil) were made 5L, outlet boundary (Right of the trailing edge of the

airfoil) were made $8L$, and walls (up and down boundary to the airfoil) were made $4L$ each. L is the length chord of the airfoil which is 1000 mm. The size of the fluid domain and the distance around the airfoil was drawn from ANSYS user guide. Surfaces were generated from both the airfoil curves and the sketches of the fluid domain thereafter Boolean operations performed to create a cut out of the airfoil surface from the surface of the fluid domain. In order to obtain a well-structured grid during meshing, projections were created dividing the fluid domain into four partitions.

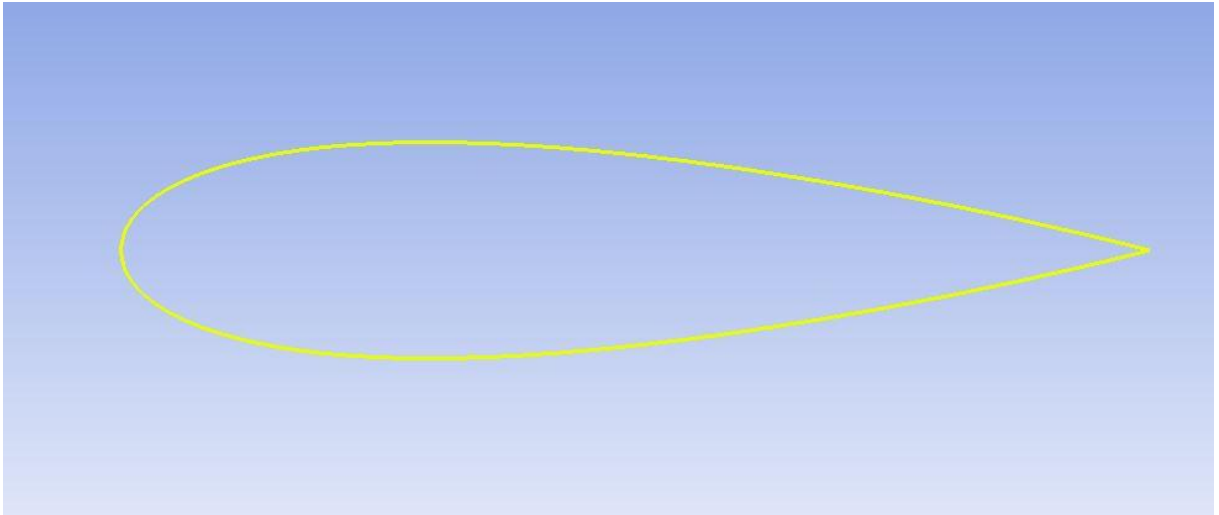


Figure 4.1 Generated airfoil in ANSYS design modeler

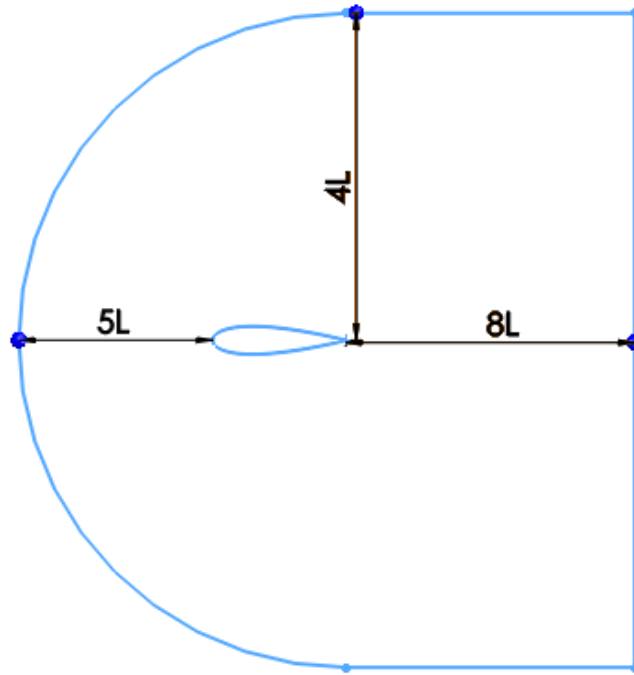


Figure 4.2: Analyses fluid domain

4.1.2 Airfoil Mesh Generation

The complete part formed after the operations in design modeler described in the preceding section was imported in ANSYS mesher where the meshing operation was carried out. Before proceeding with grid generation, sizing with a number of divisions between 300 and 500 were added to the partition lines with a bias factor of 50. This helps to obtain fine grids (mesh) in the boundaries around the geometry. The fine grids are to ensure the accurate measurement of flow characteristics. Upon completion of the necessary operation required, the grid (mesh) was generated giving a number of elements ranging from 500 000 and 570 000 for the three airfoils studied. Name selections (inlet, outlet, walls, and airfoil-wall) were created to define boundaries for the simulation.

4.1.3 Vane Shape Selection Fluent Analysis

Analyses to determine the fluid flow characteristics were performed on the selected airfoils. Pressure far-field and pressure outlet were set for inlet and outlet boundary conditions (BC). For the inlet BC, the Mach number and the gauge pressure were defined as 0.7 and 73048 Pa respectively and same pressure of 73048 Pa were set for the outlet boundary condition. The analyses were performed at airfoil deflection angle ranging from 0° to 4° which was enough to establish the flow characteristics (C_L and C_D) of the different airfoil under study.

4.1.4 Airfoil Analysis Result

Figure 4.3 below illustrates plots of lift characteristics against the vane deflection angle of the airfoils (NACA 0006, 0012 and 0016) under this study. At 4° , NACA 0006 shows 11% better

lift characteristics than NACA 0012; and 40% better lift characteristics than NACA 0016 at the range of deflection angle analyzed. This result has proven what was published by Abbott and Doenhoff that NACA 0006 gives a good lift performance at Mach number less than 0.85 (Abbott & Von Doenhoff, 1959).

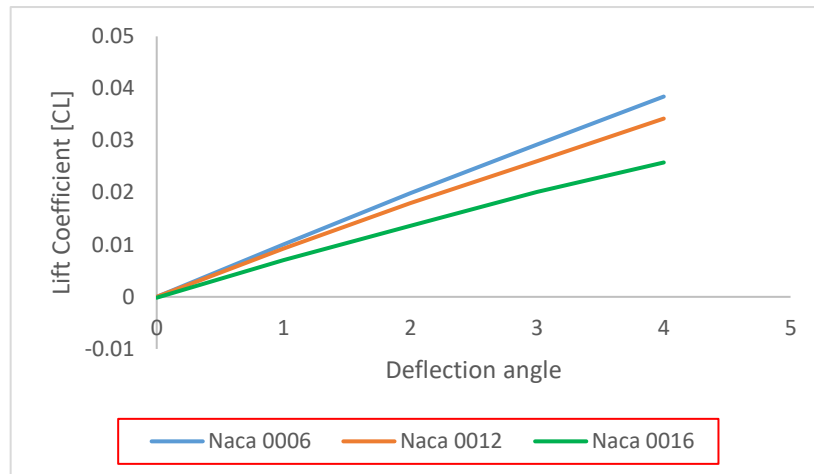


Figure 4.3: CL vs. Deflection angle curve for various airfoils

Overall, NACA 0006 shows a better aerodynamics characteristic when compared to the other two airfoils analyzed. It is clearly seen from Figure 4.4 and Figure 4.5 that NACA 0006 performs better in terms of the drag produced at a different deflection angle and in the lift to drag ratio (drag polar).

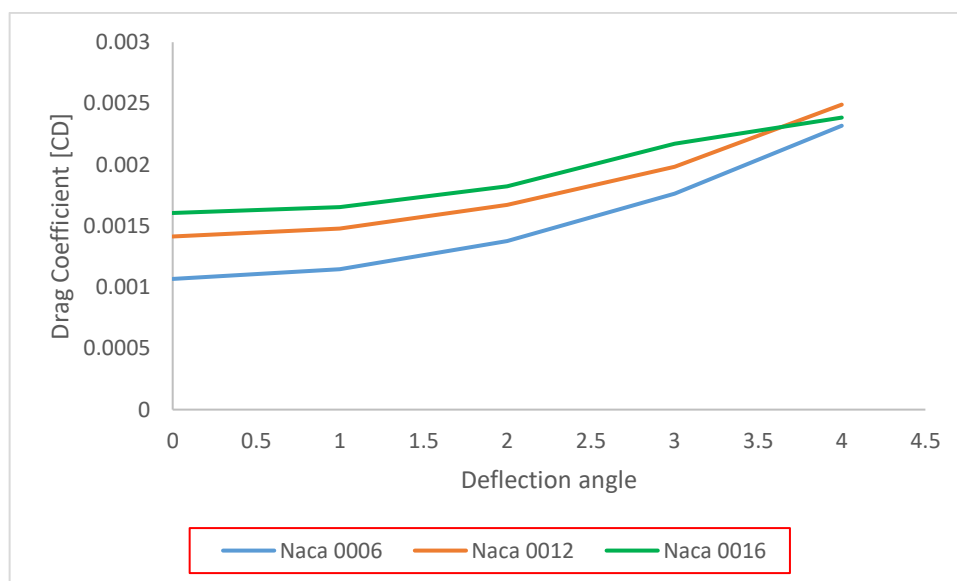


Figure 4.4: CD vs. Deflection angle curve for various airfoils

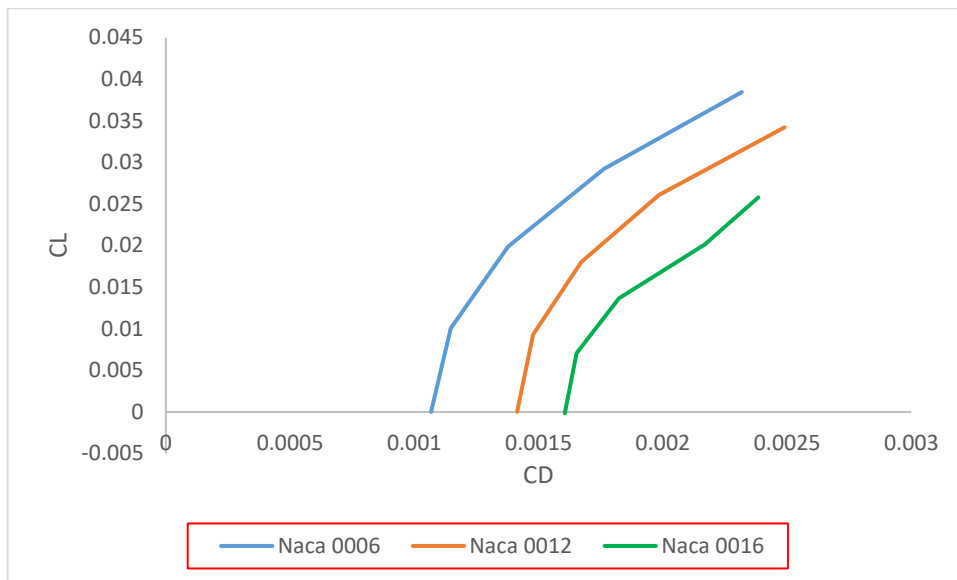


Figure 4.5: CL vs. CD (drag polar) curve for the various airfoils

4.2 Thrust Vectoring System Concept Design and Development (Complete Setup)

4.2.1 Design Concept and System Description

The design of this system follows a concept like the existing configurations which is found in jet engine aircraft or rocket. The sole aim of the process is to design a system which, when deflected, can change the pitch attitude of the aircraft even when the conventional surfaces have not acquired the required force to control the vehicle. The vanes of a jet engine aircraft are placed outside or inside the nozzle and move into the nozzle exit to deflect the exhaust flow from the engine to cause a change in the aircraft attitude. The vanes are arranged in X formation in a rocket or jet engine as shown in Figure 4.6 to cause a change of attitude in different axis to bring about the pitch, yaw or roll movement. The present work seeks to investigate the change of attitude on pitch movement and therefore, the arrangement of the vane in parallel formation shown in Figure 4.7 (that is, vanes placed on top of each other) was done taking this fact into consideration.

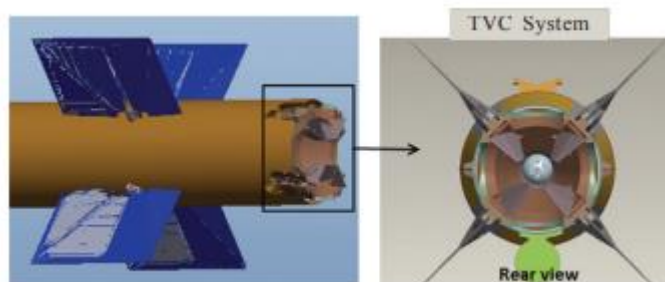


Figure.4.6: Jet vane arrangement on rocket/jet engine aircraft (Chandra Murty & Chakraborty, 2015)

Also, the arrangement was considered so that the vanes designed in airfoil shape which generates some lift force when deflected at an angle, will augment the lift generated by the aircraft wings. By so doing, the aircraft can lift off prematurely. The percentage of lift and drag generated by the vanes can be computed using equation 4.1 and 4.2.

$$L = \frac{1}{2} \rho_{\infty} V_{\infty}^2 S C_L$$

Equation 4.1

$$D = \frac{1}{2} \rho_{\infty} V_{\infty}^2 S C_D$$

Equation 4.2

Based on the chosen configuration as determined by the method of comparison and selection described in section 2.11, Cad model was developed. This consist of the vanes designed according to the shape of NACA 0012 and a shroud system.

4.3 Thrust Vectoring Vane Mechanism Design

In the design of vane for thrust vectoring applications, criteria such as lift, drag, drag polar at different deflection angle and airfoil thickness at the quarter chord, are usually considered. The quarter chord was considered taking into account the structural integrity of the vane as it will intersect high speed airflow from the propeller. For this reason, a favourable airfoil must not have a thickness above 12% (Schaefermeyer, 2011).

The following can be noted by looking closely into thin airfoil theory of symmetrical airfoil.

- Coefficient of lift (CL) = $2\pi\alpha$
- Lift slope = 2π
- The aerodynamic centre and centre of pressure are both at the quarter chord point.
- The required geometry should have its fitting at the quarter chord.
- The thickness should be around 12% of the airfoil.

Having considered all the characteristics of the various airfoils analyzed in relation to the design considerations for an effective vane, NACA 0012 offers the best overall performance,

and for that reason, NACA 0012 was chosen for this work. Also, the vane was designed matching the shape of NACA 0012 to avoid a rise in pressure distribution with no flow separation at a low deflection angle.

The vanes were designed to take advantage of the propeller free stream air measured and presented in section 3.1 by providing the maneuvering force required to rotate the aircraft and also aid it in taking off prematurely. To maximize the flow stream, two sets of vanes of span 145 mm and chord 103 mm with an aspect ratio of 1.4078 and 220 mm and 103 mm with an aspect ratio of 2.184 were designed. Notably, two sets of the smaller vanes are fixed on the shaft to be mounted at the upper and lower part of the shroud while the two bigger vanes are mounted at the centre of the shroud, showing that the splitting of the vanes is designed to give room for structural support to avoid breakage of the shaft during operation.

4.4 Shroud Specifications and Design

Performance enhancement of an aircraft to be equipped with a shrouded propeller thrust vectoring system, being considered here can only be possible if the shroud can produce thrust capable of moving the vehicle forward - overcoming the weight it added to the system. To make this possible, Pereira (2008) presents a perfect design parameters combination, although it is intended for a mini aerial vehicle (MAV) shown in Figure 4.11.

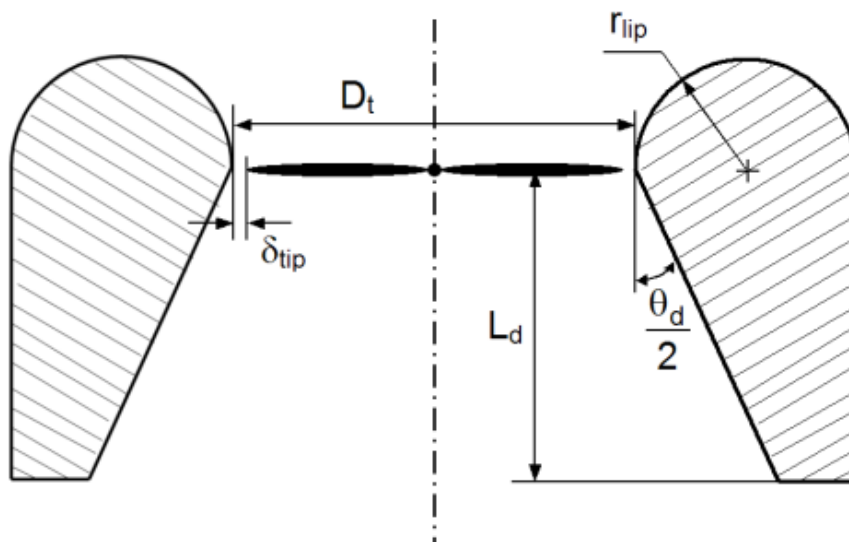


Figure 4.7: Design parameters of a shroud (Pereira, 2008)

The shroud employed for this work was chosen in conformation to the shroud used by Parlett (1955) in his research to test the effect of rip radius on lift, drag and pitching moment of a

shrouded propeller at a different deflection angle. The shroud is a uniform cylinder in which the inner surface is flat to ensure same tip clearance along the entire length. The shroud diameter D_t is 485 mm to ensure a nominal tip clearance δ_{tip} (gap between the tip of the propeller and the shroud wall) of $0.01R$ (0.001778 m). The shroud length is 300 mm which was found to have a minimal effect on the performance of the system according to Parlett. Table 4.1 summarizes the geometrical properties of the shroud. The tip clearance was carefully chosen to improve the performance by minimizing the thrust reduction by tip vortices as noted by Pereira (2008). However, to avoid the propeller blades striking the wall of the shroud during operation due to vibration, the gap was limited to the size used. The uniform diameter shroud of Parlett was chosen to allow the incorporation of vectoring vanes inside the shroud and to manage the thickness to reduce the weight penalty of integrating the system onto the airframe.

Table 4.1: Geometric properties of the propeller shroud

Characteristics	Value (mm)
Shroud inner diameter (D_t)	485
Shroud length (L)	300
Propeller tip clearance (δ_{tip})	0.001778

4.4.1 TVCS CAD Geometry Creation

The geometry can be created in any of the available drawing packages and then transferred into design modeler in ANSYS software where Boolean operation is carried out to remove the solid bodies (in this case shroud and vanes) from the solid domain. This forms the fluid domain (virtual wind tunnel) to be used for analysis. Due to the complex shape comprising of multi bodies involved in this work, the geometry as well as the fluid domain was conceptualized and designed with Solidworks. The Boolean operation was also done in Solidworks.

Figure 4.8 shows the CAD model for this work. The geometry is broken down into different parts comprising of the shroud (4), vanes (3), vane guide (2), and vane rod (1). The vanes are designed in conformity with NACA 0012 airfoil shape and having a zero-lift airfoil at zero deflection angle due to its symmetrical shape, round leading edge and sharp trailing edge. The vane guide is an auxiliary feature meant for structural integrity and holds the vane rod to prevent it from breakage during operation. The auxiliary features (vane guide and bearing casing (5)) were removed from the CAD model to prepare and make fluent simulation simpler as they will not have any effect on the actual parameters to be studied.

4.4.1.1 Vane Distance Selection

The vanes are carefully spaced to achieve optimum performance, utilizing the full airflow drawn into the shroud and accelerated by the propeller when the vanes are deflected. As shown in Figure 4.5, the flow from the propeller is at maximum at a distance 100 mm from the tip. This flow pattern governs the choice of the vane spacing from the centre of the propeller. The propeller (20 x 10) is 260 mm long from tip to centre with a blade length of about 220 mm and the holder 40 mm. Based on this measurement, the vanes were placed at 150 mm distance from the centre of the propeller as shown in Figure 4.10. From the principle of operation of airflow in a duct (shroud) as studied by Bernoulli's, the propeller draws air into the shroud, the air is divided into two (upper and lower parts) by a streamline. Upon hitting the surface of the propeller, it is accelerated and pushes it forward to create the necessary thrust required to push the aircraft forward. Even though both the shroud and the propeller have their stagnation point at the centre, the centre vane is placed so that when deflected, it will utilize the reasonable free flowing air stream at some distance from the optimum point of the propeller

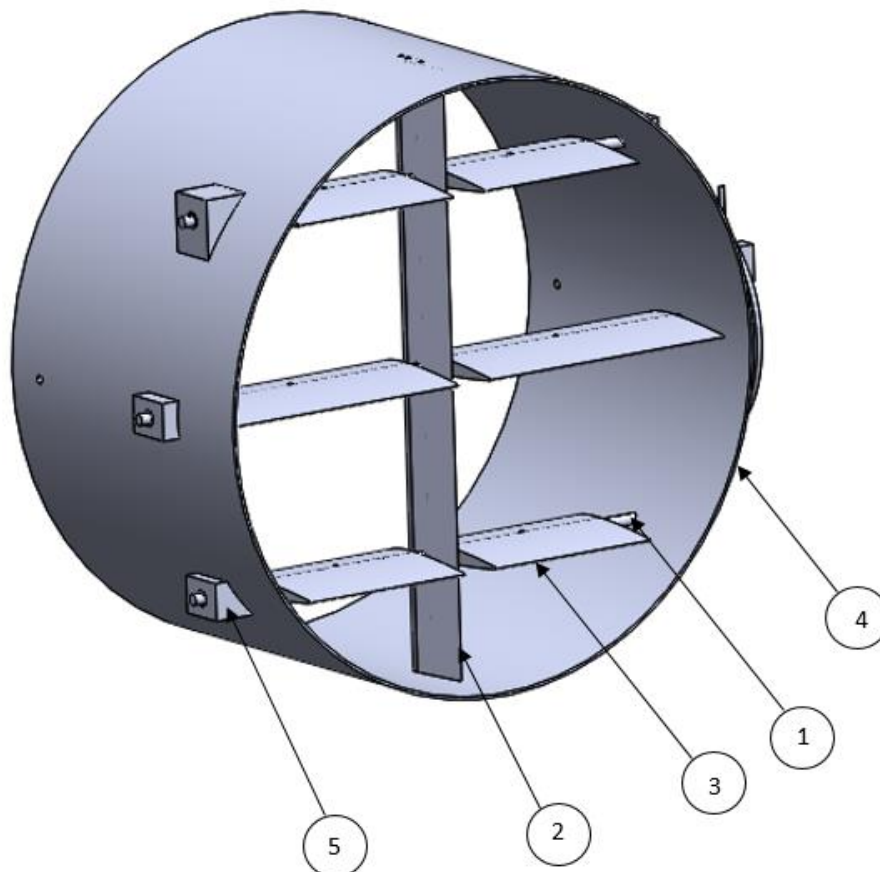


Figure.4.8: Thrust vectoring geometry model

(1. Vane rod, 2. Vane guide, 3. Vane, 4. Shroud, 5. Bearing casing)

flow. To avoid clashing with the shroud, the upper and bottom vanes are positioned closer to the vane guide to give room for a wider deflection angle.

There are six vanes separated by the vane guide as shown in the designed TVC system. The vanes instead of three sets with each spanning across the diameter of the shroud are split into. The six vanes are meant to be deflected together or independently. During take-off runs, the six vanes are deflected uniformly to an angle necessary to generate the desired lift to augment the lift generated by the wings. Also, the vanes can be deflected independently depending on the operational requirement at that point in time.

However, the operational requirement could be to counteract the forces generated that is causing instability of the UAV. That means, some sets of the vanes can be deflected downward, and some sets deflected upward. Figure 4.11a and Figure 4.11b show the side view of the designed TVC system and the vane deflection angles respectively. Figure 4.11b shows the range of angle investigated I the work.

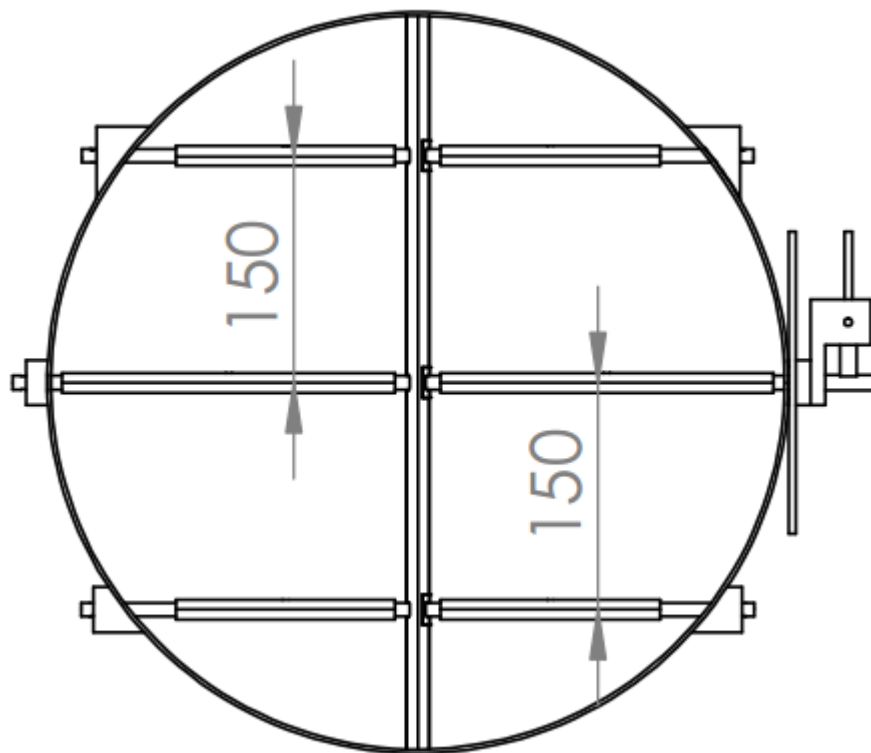


Figure.4.9: 2D TVCS showing the vane positioning within shroud

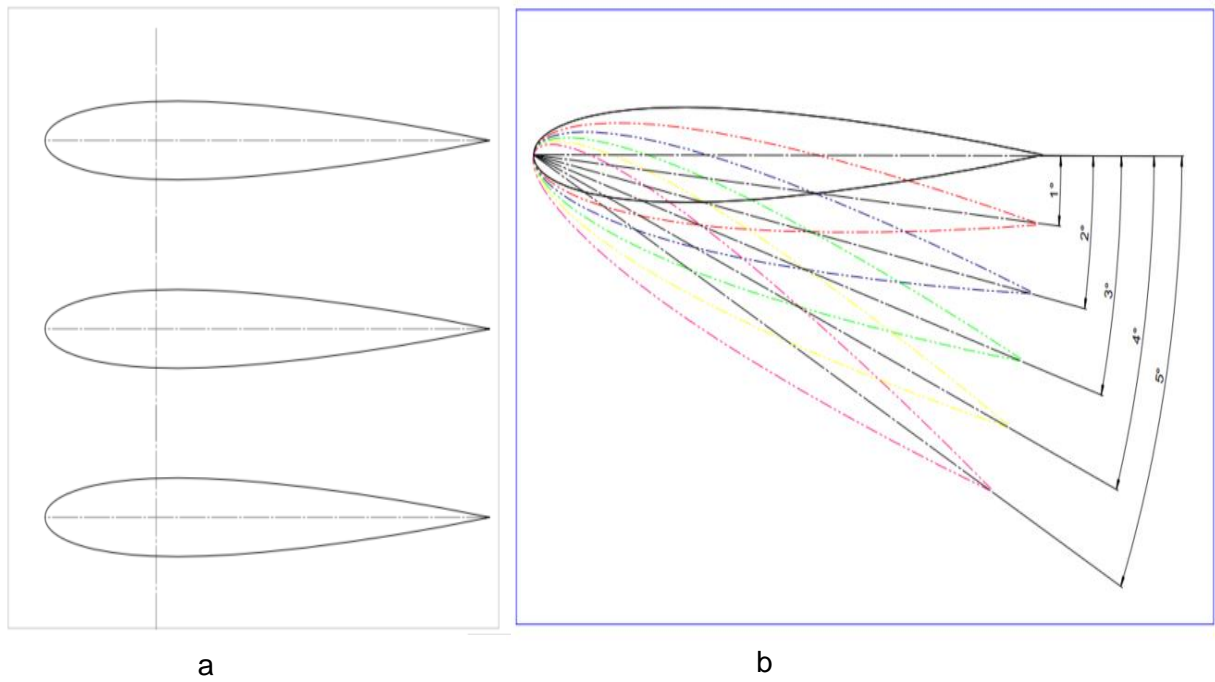


Figure 4.10 Vane deflection angles

4.4.1.2 Simplified TVC Design for CFD Analysis

To reduce the computational cost and the system requirement, the CAD model was simplified and sliced into half as shown in Figure 4.12 since it is asymmetrical object. Due to the complexity of the geometry, the fluid domain was created, and Boolean operation was done within the cad system before it was imported into ANSYS for meshing operation.

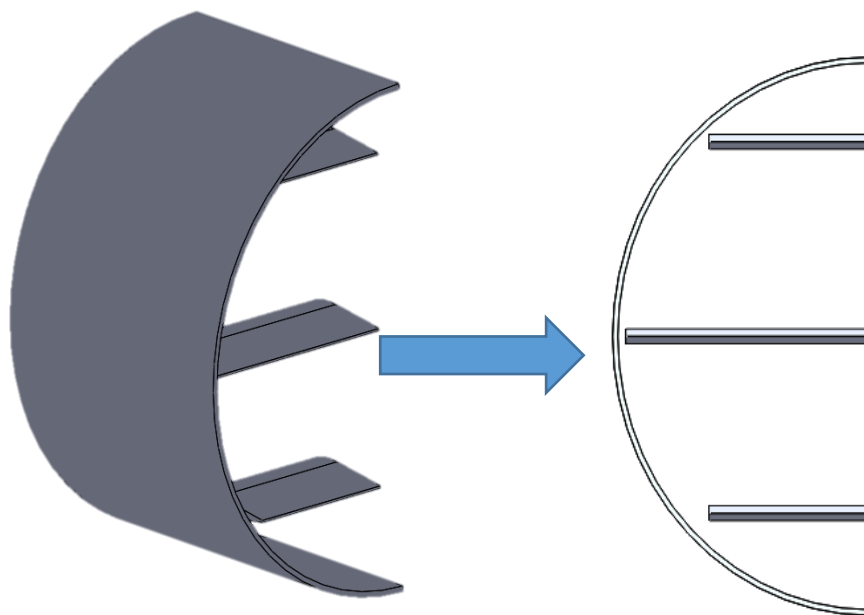


Figure 4.11 Simplified and sliced model for fluent simulation

4.4.2 Computational Domain

There are several opinions as to what the size of the computational domain should be. But generally, the size of computational domain use for CFD simulation depends on the size of the geometry and the boundary conditions. For this work, the computational domain created was large enough to handle the flow effect between the model and boundaries as stipulated in ANSYS user guide (ANSYS, 2012). The model was located at distances in relation to the length and diameter of the shroud. The inlet was located 1500 mm from the model which is $5L$ of the model, the outlet 3000 mm which is $10L$, upper and lower boundaries were located 990mm which is $2D$ as shown in Figure 4.13 - while L and D are the length and diameter of the model, which are 300 mm and 495 mm respectively.

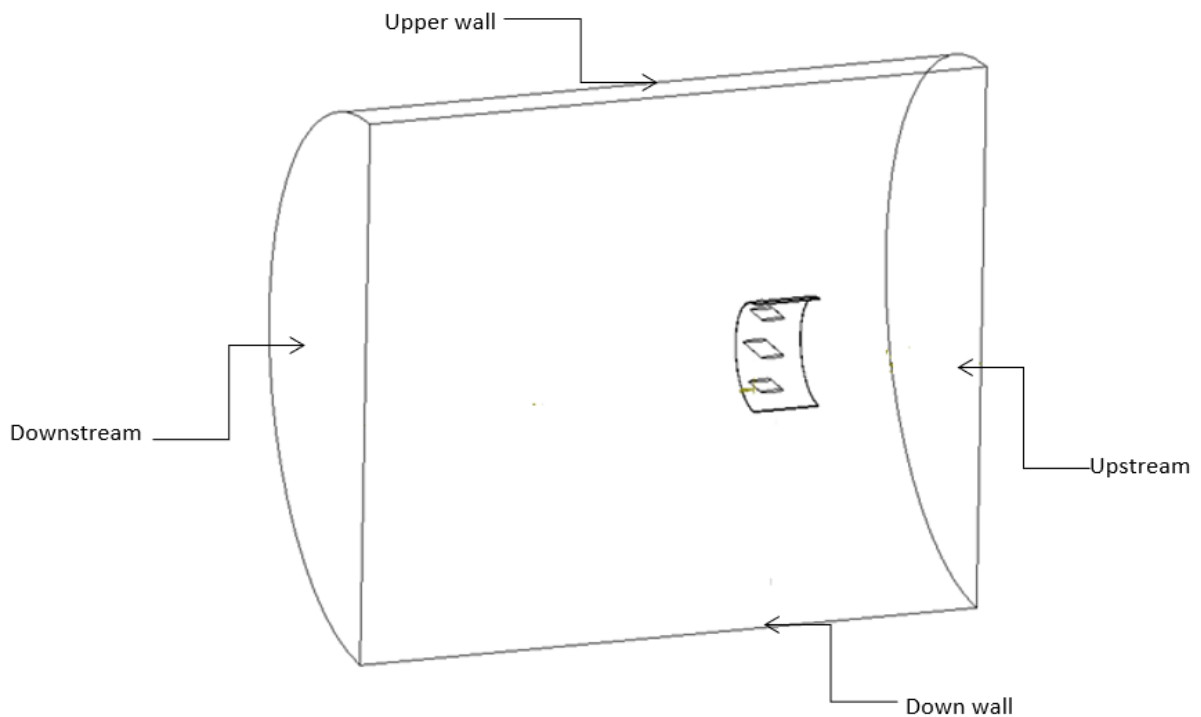


Figure 4.12 Computational domain

CHAPTER FIVE: CHARACTERIZATION OF THRUST VECTORING CONCEPTS

This chapter accounts for the CFD FLUENT analysis performed on a CAD model described in section 4.3 using parameters obtained from the velocity profile experiment detailed in section 4.4. The chapter also describes the set-up processes employed in characterizing the designed TVC system to establish the drag, lift coefficient, force and pitching moment generated when the vanes are deflected at a different vane deflection angle.

5.1 Characterized TVCS CFD Analysis

CFD simulation performed in this work followed the three different stages involved in a typical CFD simulation namely pre-processor, solution analysis, and post-processor. The activities involved in each stage are discussed in details below.

5.1.1 Pre-processor

Pre-processing involves the definition of the problem, geometry creation, meshing and finally checking for the regime of the flow. One could check for the regime of the flow using the Reynolds number equation as shown below to determine whether the flow is laminar or turbulent.

$$Re = \frac{\rho VL}{\mu} = \frac{LV}{\nu} = \frac{\rho VD}{\mu} \quad (\text{Anderson Jr. et al, 2009}) \quad \text{Equation 5.1}$$

Where ρ is the density of the fluid which in this case is air, V is the velocity of the flowing fluid, D is the characteristic diameter of the system, L is the characteristic length of the system, ν is the kinematic viscosity of the fluid and μ is the dynamic viscosity of the fluid. Using the Reynolds number equation, it can be determined that the lowest Reynolds number for this flow considered is 8.9×10^4 and the highest is 1.63×10^5 which is greater than 2300. Any flow regime for which Reynolds number is greater than 2300, as in this case, is a full turbulent flow. Therefore, during the simulation involved in this work, turbulent model was the choice model.

5.1.2 Mesh Generation

Basically, this process is regarded as the most important process in CFD pre-processing and in fact for the entire CFD simulation. The quality of a mesh plays a pivotal role in determining the accuracy of the solution. The percentage quality of the mesh determines the percentage accuracy of the solution, that is, the higher the mesh quality, the higher the result accuracy

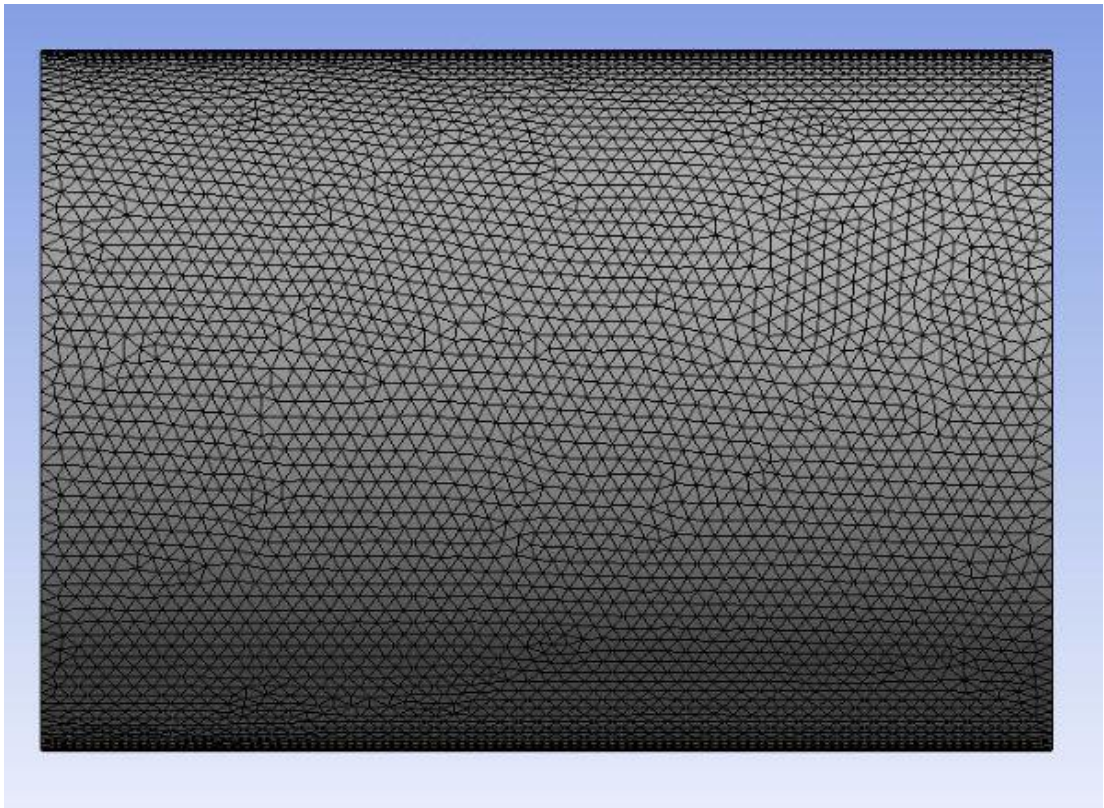
and vice versa. Meshing involves discretizing and breaking the entire computational domain into smaller control volumes (cells). The numerical studies are then carried out on the control volumes at constant intervals to simulate the passage of time since the numerical analysis can only give results at discrete points at a defined time interval.

There are different ways to generate a computational mesh for CFD application. Firstly, one could employ an external source software which generates unstructured mesh; alternatively, one could use a software which can generate a structured mesh. There is a computational advantage in generating unstructured mesh as they are easy to generate, and they have a lower computational cost. However, they are of lower quality when compared to structures mesh. On the other hand, the structured mesh is more tedious to generate and it incurs more computational cost. However, it yields a very high-quality mesh.

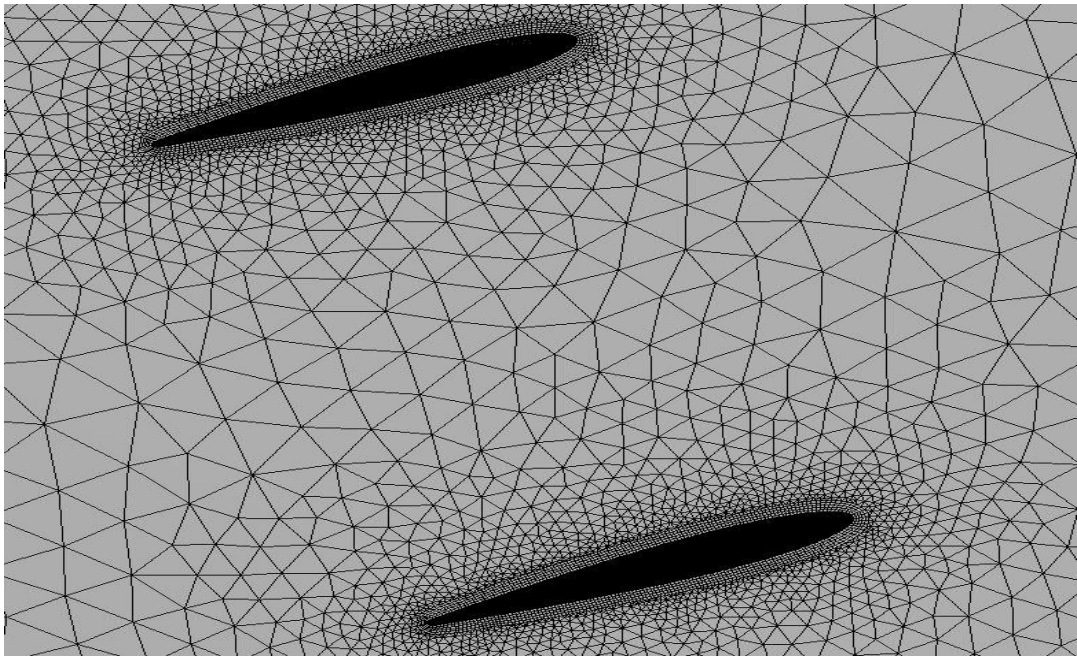
Mesh for this work was generated using ANSYS mesh generator. Due to the computer capacity available for this work, and the complexity of the geometry, an unstructured triangular mesh was generated as the generation of a structured quadrilateral mesh was not possible. This being an automatic mesh generation has a minimum face size of 1.806mm, a maximum face size of 180.560mm growth rate of 1.20, mesh quality of 0.15091, and mesh statistic of 3.8million cells. To obtain a good quality mesh which in turn would yield a good simulation result, further refinement was carried out by adjusting the minimum and maximum face size until an optimum value was obtained - resulting in a higher mesh quality. Figure 5.1(a and b) and 5.2 show the mesh obtained after refinement.

5.1.2.1 Mesh Quality

This is an essential parameter in CFD simulation. It plays an important role in ensuring a good and accurate result of a solution. A finer mesh will produce a more accurate result than a medium mesh, while a medium mesh will produce a better result than a coarse mesh. The quality of a mesh is defined by its orthogonality. Three factors are used to measure the quality of a mesh are the maximum cell skewness, the maximum aspect ratio, and the maximum cell squish. For a proper and accurate simulation, low orthogonal quality and high skewness are not recommended, meaning an orthogonal quality of less than or equal to 0.1 or skewness of greater or equal to 0.95 should be avoided. This implies that obtaining an orthogonal quality of greater than 0.1 and skewness of less than 0.95 is desirable and highly recommended. However, orthogonal quality and skewness may differ depending on the physics and the location of the cell. Table 5.1 and Table 5.2 show skewness and orthogonal quality spectrum which serves as a guide to judge mesh quality.



a



b

Figure 5.1: Generated mesh view

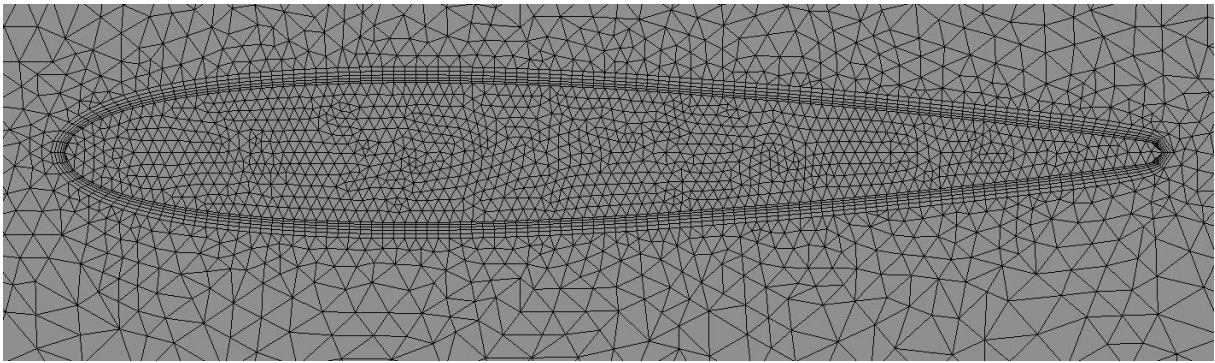


Figure 5.2: Generated mesh sowing inflation around the vane

Table 5.1: Skewness mesh metric spectrum

Excellent	Very good	Good	Acceptable	Bad	Unacceptable
0 - 0.25	0.25 – 0.50	0.50 – 0.80	0.80 – 0.94	0.95 – 0.97	0.98 – 1.00

Table 5.2: Orthogonal quality mesh metric spectrum

Unacceptable	Bad	Acceptable	Good	Very good	Excellent
0 – 0.001	0.001- 0.14	0.15 – 0.20	0.20 – 0.69	0.70 – 0.95	0.95 – 1.00

Based on the metric spectrum given which is to be used for quality check, the mesh quality of this work is 0.17037 which falls under the acceptable quality region. This is presented in Table 5.3 which shows the orthogonal quality of the mesh obtained in this work.

Table 5.3: Mesh quality

Quality	
Check Mesh quality	Yes, Errors
Target Skewness	Default (0.900000)
Smoothing	High
Mesh metric	Orthogonal Quality
Min	0.17037
Max	0.99775
Average	0.75415
Standard Deviation	0.14782

5.2 TVC System Solution Analysis

All the important and sophisticated work of CFD simulation is done here. The parameters such as turbulence models, boundary conditions (inlet velocity, outlet velocity etc.), solver type (pressure-based or density-based), the solution method for velocity- pressure coupling etc. required for simulation are defined. The flow governing equations are solved iteratively here to determine the flow variables as the iteration time elapse.

5.2.1 Fluent Analysis

ANSYS FLUENT is Computational Fluid Dynamic (CFD) software used for simulation of the fluid flow in this work. The software is suited to high-performance computing and can perform a simulation model on two-dimensional and three-dimensional structures which exist as laminar, turbulent, compressible and incompressible flow. It is a computational package widely used in industries to proffer a solution to industrial related problems and also for research purposes. CFD is used in all stages of the engineering process, conceptual studies of new designs, detailed product development, optimization, troubleshooting and redesign. CFD analysis compliments testing and experimentation by reducing the total effort and cost required for experimentation and data acquisition.

The turbulent flow field is modeled using steady Reynolds- Average Navier Stoke equation in combination with turbulent models which are widely in use in the field of CFD, k - ω (k - ω SST) model. To account for the compressibility effect, pressure-based, and density-based solver was chosen, analyzed and their result compared. Moreover, the second upwind scheme for both gradient, pressure and momentum discretization was applied to numerically solve the flow equation. Under relaxation, factors were set for pressure, density, body forces, momentum, turbulent kinetic energy, turbulent dissipation rate, turbulent viscosity and energy as 0.5, 1, 1, 0.8, 0.8, and 1 respectively.

The working fluid is air treated as standard density gas, with properties listed in the Table 5.4 below.

Table 5.4: Working parameters property list

Properties	Values
Air	Standard
Density	1.225kg/m ³
Viscosity (constant)	1.7894 x 10 ⁻⁵ kg/m-s

Inlet boundary condition	Mass flow inlet
Outlet boundary condition	Pressure outlet

5.2.1.1 Solution Procedure

Fluent activities are numerous and systematic. Fluent activities entail the settings and process of calculations that determine whether a solution will produce an accurate result or not. The accuracy of the result produced thereby depends on careful, thoughtful, and accurate settings of individual components making up the solution procedure, and it thus demands great attention. Solution procedure involves the selection of solution parameters, initialization, convergence and an accuracy check. These activities were carefully performed across these procedures during the process of this work and were reported in this section.

5.2.2 Solution Parameters

This involves the selection and setting of appropriate solver (pressure based) for the solution which depends on the type of simulation (compressible) involved and on setting the spatial discretization scheme.

5.2.2.1 Solver

Solvers are formulated algorithms (numerical techniques) designed to solve a system of partial differential equation relating to fluid flow using a computer. Solvers employ different numerical techniques (like finite difference method, finite volume method, finite element method, Runge-Kutta methods, Taylors series, Eulerian expansion, forward/backward scheme and Newton-Rapson scheme) used in solving mathematical equations. The numerical technique(s) formulated into a solver, however, depend(s) on the associated problem to be solved. Two solvers are employed in ANSYS FLUENT and are used to proffer a solution to fluid flow problems - these are pressure-based, and density-based coupled solver.

Pressure Based Solver

This solver considers momentum and pressure correction. It makes use of algorithms which solve pressure equations derived from continuity and momentum equations to achieve mass conservation of velocity field through an iterative process. This is done until all governing equations are solved to give a converged solution. A pressure-based solver was originally developed for incompressible and mild compressible flow but has since been improved upon

to accommodate high compressible flow. Furthermore, two pressure-based algorithms are available in fluent. They are:

- A Segregated solver: Here, the pressure correction and momentum are solved sequentially in a decoupled manner. It is memory efficient as the governing equations are discretized and solve one at a time. However, the solution convergence is relatively slow in that it solves momentum and pressure equations using the recently updated pressure and velocity field.
- A Coupled solver (PBCS): As the name implies, and unlike the segregated solver, it solves the governing equation in a coupled manner, meaning the equations are solved simultaneously. Convergence is achieved faster here but the memory requirement is high.

Density-Based Coupled Solver (DBCS)

DBCS employs vector form in solving continuity, momentum, energy, and species equations. These equations are solved in a coupled manner but later will be segregated to solve additional scalar equations. DBCS is highly recommended where there is strong coupling or interdependence between density, energy, momentum and species. Two algorithms are also available for density-based solver in fluent. They are:

- Implicit algorithm: This employs mathematical methods like point-implicit Gauss-Seidel, symmetric block Gauss-Seidel or an incomplete lower upper (ILU) factorization scheme to solve for variables. Each set of governing equations are linearized implicitly, and the unknown variables pressure, u-, v-, w- velocity and temperature field (p, u, v, w and T) are solved simultaneously (at once).
- Explicit algorithm: This uses a multi-step Runge-Kutta explicit time integration scheme to tackle a system of governing equations. The governing equations are linearized explicitly in this algorithm and the unknown variables are solved using the update from the existing field variables, causing the unknown variables to be computed independently.

5.2.3 Spatial Discretization Scheme

Numerically, governing equations are reduced to a solvable form by developing a stable, consistent and accurate algebraic equation capable of replacing them. Control-volume techniques is used by ANSYS FLUENT to achieve its discretization purpose by integrating the governing (transport) equations about each control volume.

$$\frac{\partial}{\partial t} \int_V \rho \phi dV + \oint_A \rho \phi V \cdot dA = \oint_A \Gamma_\phi \nabla \phi \cdot dA + \int_V S_\phi dV \quad \text{Equation 5.2}$$

(Versteeg & Malalasekera, 2007)

Essentially, the field variables are interpolated to the faces of control volume through the following equation by obtaining the value of ϕ

$$\frac{\partial \rho \phi}{\partial t} V + \sum_f^{N_{face}} \rho_f \vec{v}_f \phi_f \vec{A}_f = \sum_f^{N_{face}} \Gamma_\phi \nabla \phi_f \vec{A}_f + S_\phi V \quad \text{Equation 5.3}$$

(Cyklis & Młynarczyk, 2016)

Furthermore, different spatial discretization schemes are available in fluent; gradient, pressure, momentum, turbulent kinetic energy and specific dissipation rate scheme. The following discretization methods are available in fluent for momentum, turbulent viscosity and specific dissipation rate.

- First-order upwind: This has the advantage of converging easier than any other discretization scheme. However, accuracy is not guaranteed in all simulation cases especially when the grids are not aligned with the flow like in a case where tetrahedron mesh is involved. It is however acceptable when the flow is laminar and is modeled with hexahedral or quadrilateral grid.
- Second-order upwind: This gives second order accuracy but is slow in convergence. It handles more accurately any simulation work which involves trihedral and tetrahedral mesh, and when the flow is not aligned with the grid. For this work, second order upwind was selected as an ideal discretization method due to the high order of accuracy required and due to the tetrahedron mesh involved.
- Power law: This works better when the Reynolds number is less than five (5). It is more accurate than the first-order upwind scheme.
- Quadratic Upwind Interpolation (QUICK): This is applicable and produces more accurate results than the second order upwind in a simulation that has to do with rotating or swirling flow. However, it does not differ in accuracy from second order upwind in areas where second-order is enough to produce an accurate result. It usually does better in rotating or swirling flow on a quadrilateral or hexahedral simulation.
- Monotone Upstream-Centred Schemes for Conservation Laws (MUSCL): A third order convective scheme developed from a blend of second-order upwind and central differencing scheme. It is usually applicable to both structured and unstructured mesh with improved spatial accuracy and reduced numerical diffusion.

In ANSYS FLUENT, discrete values of scalars ϕ are deposited at the cell centres and the face values ϕ_f are interpolated using the cell centre values. Depending on the simulation type being done, one of the above discussed discretization schemes can be selected. As stated also above, second-order upwind was selected for this application as it provides a better result for tetrahedral mesh generated in this investigation.

Gradient discretization is required in any simulation to give the gradient solution of the flow variables needed to estimate the diffusive fluxes and velocity derivatives. The gradient of a given variable is used to calculate the convective and diffusion term in a flow equation. Three gradient discretization methods are used to compute variable gradient in ANSYS FLUENT. They include Green-Gauss cell based, Green-Gauss node based, and Least-Square cell based.

The Green-Gauss theorems compute gradient of scalar ϕ from the centre of cell in form:

$$(\nabla\phi)_{c0} = \frac{1}{V} \sum_f \bar{\phi}_f \vec{A} \quad \text{Equation 5.4}$$

- The Green-Gauss Cell-Based: This method computes the value of a cell on wall ϕ_f as a mean value from values of nearby cells using equation 5.5. It has a record of being intensive in terms of the computational cost, but the solution is likely to contain false diffusions.

$$\bar{\phi}_f = \frac{\phi_{c0} + \phi_{c1}}{2} \quad \text{Equation 5.5}$$

- The Green-Gauss Node-Based: The result obtained here is more accurate, but it is obtained at a higher computational cost. However, false diffusion is minimal in this method, and it is recommended for unstructured mesh. Moreover, the value of a cell is computed by this method as a mean value from the nodes of a given wall(s) using equation 5.6.

$$\bar{\phi}_f = \frac{1}{N_f} \sum_n^{N_f} \phi_n \quad \text{Equation 5.6}$$

The Green-Gauss Node-Based was selected for this simulation.

- The Least-Squares Cell-Based: This method has equal accuracy and properties to the Node-based Gradients scheme but with less computational cost in terms of its simulation time. This scheme is usually recommended to be used in polyhedral cell

Initialization

For fluent to perform some iterations, the starting point must be set to serve as the basis for the simulation iterations. The setting of initial value to serve the purpose of a starting point for

iteration is known as initialization. This initial value required in order to start iteration must exist for every quantity that takes part in the simulation. CFD codes use this initial value for the first iteration; and then in the second iteration, it uses the first iteration value. Two initialization methods existing in ANSYS FLUENT are standard initialization, and hybrid initialization.

- **Standard Initialization:** This initialization method enables users to enter the variables (x-velocity, y-velocity, z-velocity, pressure, and temperature) which properly define the simulation environment and conditions. After defining the initial variables, a specific point (inlet) from which the initial iteration calculations will be made was chosen.
- **Hybrid Initialization:** This method does not require the user to specify the initial point from which to calculate, however, it gives a quick approximation of flow field using some methods. To perform initialization, this method solves Laplace's equation to determine the pressure and velocity field to be used for the simulation.

Based on the description given above, an appropriate solution parameter(s) was selected and applied in the present work. Table 5.5 contains the summary of the solution parameters used.

Table 5.5: Solution parameters

Solution Parameters	Selected Numerical Algorithm
Flow domain	Symmetrical shroud thrust vectoring system
Selected grid size	5.377×10^6 elements
Simulation fluid	Air at standard condition (See table 5.4)
Turbulent models	SST- $k-\omega$
Pressure and velocity coupling	Coupled algorithm
Spatial discretization and pressure interpolation scheme	Second order upwind
Initialization method	Standard initialization
Solution monitored parameter	Lift coefficient, Drag coefficient, moment and force

Convergence

Convergence monitors and criteria were employed to ensure that the result of the simulation performed in the work converged to the desired tolerance. In this case, three convergence monitors were set. The residual of all the governing equations, as well as the turbulent model equations, were monitored until they fell between three orders of magnitude (10^{-3}) and six orders of magnitude (10^{-6}) or even lower than 10^{-6}) after which the system was considered converged. Figure 5.3 shows the residual plot showing the convergence of the simulation. The continuity equation falls below 10^{-3} , x and z velocity fall below 10^{-5} while the turbulent model equation and the y velocity fall below 10^{-7} . The second convergence monitor employed will be to monitor the C_L and C_d values around the vanes until the solution becomes stable without any changes in the simulation result (values) even at some further iterations.

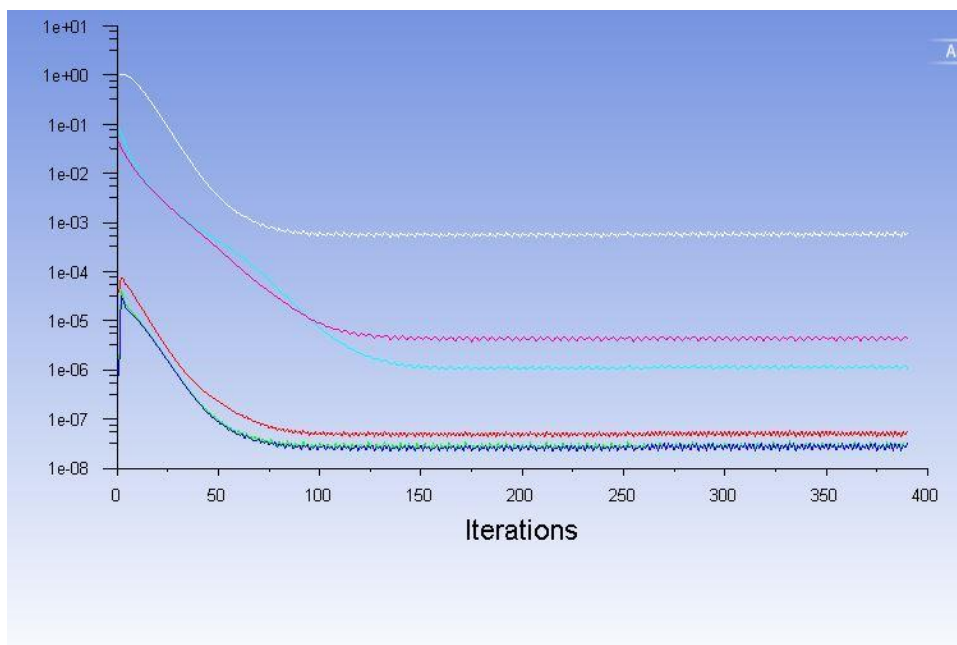


Figure 5.3: Convergence residual plot

5.2.4 Virtual Environment Boundary condition

In setting the boundary conditions, it is imperative that the set conditions resemble the actual scenario being modeled. If the boundary conditions do not depict the actual system and conditions for compressible flow simulation, the result will not match the actual experimental result. For this project, the simulation has one inlet, one outlet, and a symmetrical plane boundary condition.

Since the system testing was taken to be done in a wind tunnel, hence the system boundary conditions were set up to meet the wind tunnel standard. The wind speed surrounding an

aircraft to be tested in a wind tunnel is usually uniform across all surfaces of the aircraft. To meet the requirement of experimental analysis and to reduce the cost of experimentation in engineering, simulation is required. On this note, a virtual wind tunnel system was employed with ANSYS FLUENT chosen as the platform for the virtual analysis. Based on this, the wind speed in and out of the shroud of the TVC system was taken to be uniform. But this does not remove the fact that the analysis is centred on the aircraft control parameters which the vanes can generate when deflected into the air from the propeller. The boundary conditions used in this work will be discussed shortly.

5.2.5 Mass Flow Inlet

In a mass flow boundary condition, either the mass flow rate or the mass flux is specified at the inlet. As much as the analysis permits, the total pressure is allowed in the mass flow inlet to vary across the boundary. The mass flow BC set for this thesis ranged between 11.173 kg/s and 21.329 kg/s which was obtained from an airflow velocity experiment of a spinning propeller running at the speed ranging from 2000 rpm to 4000 rpm as described in section 3.1.

The inlet BC (Mass flow rate) was computed using equation 5.7

$$\dot{M} = V \cdot \rho \cdot A$$

Equation 5.7

Where V is the velocity of the air, ρ is the density of the air and A is the cross-sectional area of the shroud.

Area of the shroud which is the area containing the airflow was calculated using the equation 5.8

$$A = 2\pi r h + 2\pi r^2$$

Equation 5.8

Based on conditions for using a symmetrical plane, half of the calculated mass flowrate was used as the inlet flow boundary condition.

5.2.5.1 Virtual Environment Boundary Condition

Since the system testing was taken to be done in a wind tunnel, hence the system boundary conditions were set up to meet the wind tunnel standard. The wind speed surrounding an aircraft to be tested in a wind tunnel is usually uniform across all surfaces of the aircraft. To meet the requirement of experimental analysis and to reduce the cost of experimentation in engineering, simulation is required. On this note, a virtual wind tunnel system was employed

with ANSYS FLUENT chosen as the platform for the virtual analysis. Based on this, the wind speed in and out of the shroud of the TVC system was taken to be uniform. However, this does not remove the fact that the analysis is centred on the aircraft control parameters which the vanes can generate when deflected into the air from the propeller.

5.2.5.2 Flow Inlet Mass Flowrate Profile

As discussed in detail in section 4.4.1 and shown in Figure 3.5, the air velocity along the length of a spinning propeller is not constant, therefore, in order to accurately represent the real practical scenario, a mass flow profile was developed. However, for the reason stated in section 5.2.5.1, the author did not use the profile for the analysis. The profile shown in Appendix E considers the mass flow of the air at the various propeller rotation speeds considered in this work at a different point (x,y coordinates) across the shroud diameter.

5.2.5.3 Pressure Outlet

In the pressure outlet boundary condition, the static pressure was calculated using thearcy-Weisbach equation (Kiijarvi, 2011) shown in equation 5.9 to obtain the pressure at the shroud exit. When this is known, it allows the mass flow/velocity of the process to vary in order to make the solution stable. The pressure at the shroud exit is also expected to vary relative to the mass flowrate, hence a pressure profile shown in Appendix E was also developed.

$$\Delta p = f \frac{L}{D} \frac{\rho V^2}{2} \quad \text{Equation 5.9}$$

Where

- Δp is the pressure loss
- f the Darcy friction factor
- L length of shroud
- D inner diameter
- ρ density of air
- V flow velocity

5.3 Post-processing

After performing the CFD analysis, the next step was to visualize and qualitatively process and report the important result effectively. Post-processing comes into play in graphically presenting the result of the simulation as contours of velocity, pressure and temperature. It also becomes operative when displaying the velocity vectors and the streamlines which show the direction and flow pattern. The results can also be presented by x-y plots, by a histogram, as well as by tables.

Figure 5.4 shows a summary of the steps in a CFD simulation starting from pre-processing to post-processing.

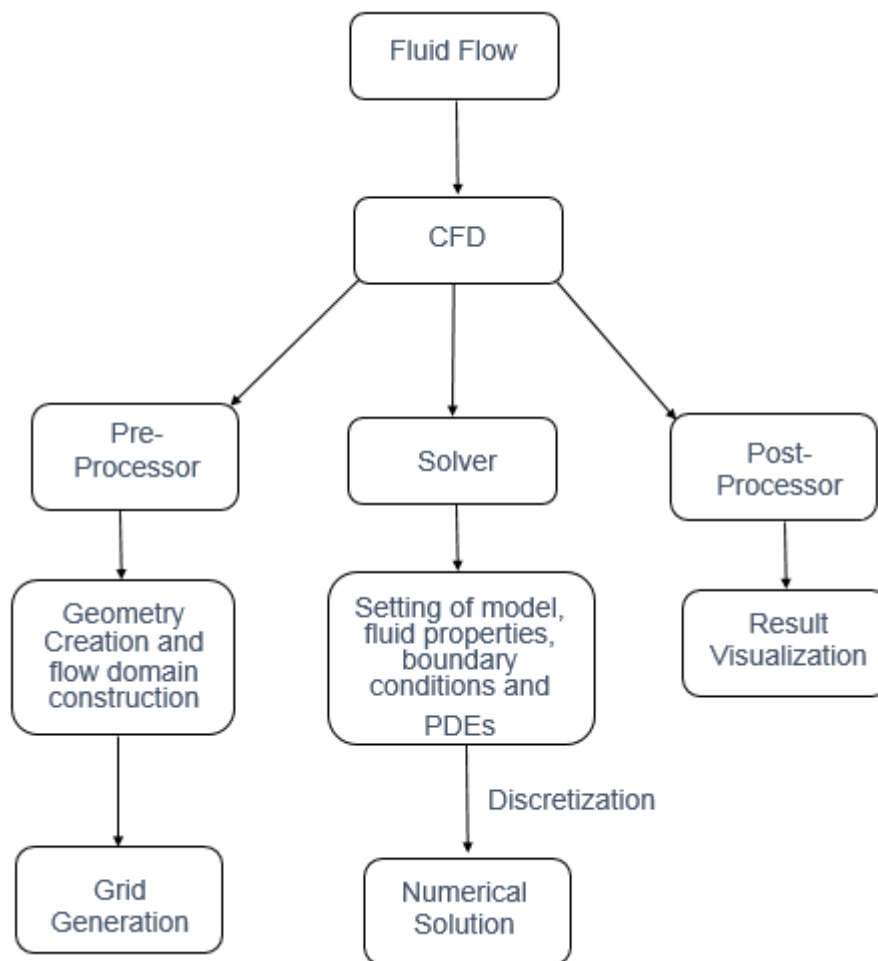


Figure 5.4: Overview of CFD

CHAPTER SIX: ANALYSIS, RESULT PRESENTATION AND DISCUSSION

The chapter presents the characterization result of the TVC system. It shows the percentage increase in lift, drag, and moment of the aircraft. The chapter also presents the calculation and percentage reduction in S_g , power and rate of climb. Overall, it explains the proof of the effectiveness of TVC system in giving the GII UAV STOL capabilities.

6.1 Simulation Analysis

The thrust vectoring system as already stated throughout this work is meant to assist the entire aircraft in its maneuverability at the early stage of operation. To reduce the ground roll, CFD analysis was performed on a conceptual CAD model of TVCS at vane deflection angle ranging from 0° to 5° . Mass flow rate was specified as the inlet boundary condition. This was computed using equation 5.7 and 5.8 with the air velocity obtained from an experiment detailed in section 4.4 as the input parameter. From the shape of the vane designed to match an airfoil, some lift was generated. The generated lift is expected to augment the total lift generated by the wings of the aircraft needed for its flight. Although the propeller air velocity experiment reveals that the air velocity across the length of a propeller varies from the tip, where it is zero, to about 100 mm along the propeller where it is maximum, and then decreases to zero again towards the propeller core centre. But an assumption of a constant velocity field was made in this work, implying that the airflow was taken to be uniform across the propeller length. This assumption was made to mimic a wind tunnel environment which usually have a constant air velocity around the object to be analyzed. The range of vane deflection angle chosen for simulation was enough to establish the actual effect of the thrust vectoring system on the performance of the aircraft at low speed when the control surfaces are yet to acquire their full forces.

Commercial CFD software (ANSYS FLUENT) was employed to study the flow characteristics around vanes within a shroud system. The lift, drag, pitching moment and force were studied, and the quantitative and qualitative result analysis are presented in the next section (section 6.2).

6.2 Spatial Distribution of Aerodynamic Parameters

A detailed result of the analysis is presented in this section. The analysis in section 6.2.1 gives the qualitative result obtained from the simulation, while section 6.2.2 gives the quantitative result of the analysis. The qualitative result is a display of the behavioural pattern and distribution of the quantities of interest around the system being studied. It shows the magnitude of the quantities as a function of position on the geometry; while the quantitative

result gives the quantified variable graphically for a clear graphical interpretation of the functionality of the system.

6.2.1 Qualitative Result Analysis

6.2.1.1 Velocity Distribution

A total of 25 analyses were performed covering the vane deflection angle 0-5° and the propeller speeds of 2000 – 4000 rpm. The velocity distribution around the TVC system follows the same trend across the range of propeller speeds and vane deflection angle analyzed. The results obtained from the analyses are presented in Figure 6.1(a-f). The figures are randomly selected velocity profile (velocity contour) of the TVC system since they are all identical in terms of air velocity interaction with the geometry but only differ in magnitude. As shown from the figure, the air velocity upstream, inside, below, top and downstream of the shroud varies at the different rotational speeds of the propeller (increasing air velocity). Figure 6.1 (a), and (e) show the velocity behaviour at 2000 rpm and 4000 rpm prop speed at vane deflection angle of 1°. It can be deduced from the figure that the airspeed around the shroud (the orange distributions areas) is relatively the same. The aerodynamic explanation of this is that the lifting of the TVC system is not possible as the forces and the air pressure around the shroud balances (or cancels out) hence the system will be in the state of equilibrium. This condition is only desirable at the cruising stage of an aircraft and not at this stage (take-off) under consideration. Figure 6.1(b), (c), (d), and (f) show the velocity distribution at 2000 rpm, 3000 rpm, 3500 rpm, 4000 rpm, and at angles 5°, 3°, 5°, 5° respectively. The figures clearly show increasing air velocity above the shroud and around the vanes as the propeller rotational speed and the vane deflection angle increases. At the downstream of the shroud and below the vanes, it shows that the air velocity decreases (the yellow areas). Following the principles of aerodynamics and laws that govern the lifting off of any object heavier than air; the higher the velocity, the lower the pressure; and the high velocity must be above the object to necessitate this action. The high velocity builds up around the vanes and adds to the operational advantage of the TVC system, and thus proves that the author's choice of employing airfoil shape for the vane design is correct. The velocity along the vanes and around the shroud shows the same trend across the speeds analyzed. The velocity first decreases to a distance of 0.18 m before stabilizing to a uniform value across the length of the vane as shown in Figure 6.2.

Based on the result obtained, the TVC system design proves to be a good support system. In isolation, it can generate lift to aid the aircraft in achieving its mission of taking off prematurely. The graphical plot supporting this claim is presented in section 6.2.2.

6.2.1.2 Pressure Distribution

The display of pressure during the operation of the designed TVC system are displayed in Figure 6.4 (a-f). The distribution, both at the upper and lower surface of the vanes are the same at a low propeller speed but they start to separate as the speed and vane deflection angle

increase. The separation of the pressure around the vanes is an indication of a drop caused by an increase in air velocity due to the increasing and high rotational speed of the propeller. Figure 6.3 shows the behaviour of the pressure with respect to prop speed along the x-axis which is the direction of airflow (aircraft course). It shows an initial almost uniform decrease of pressure along the width of the vane as we move from 0 to 0.18 m at all the prop speed tested. Beyond 0.18 m, the pressure increased relatively but its inverse relation with velocity as explained in section 6.2.1.1 can be observed. Between 0.18 m and 0.26 m, the pressure on the vanes is low. The scientific explanation of the pressure distribution is that the system will generate lift both by the vanes and by the shroud.

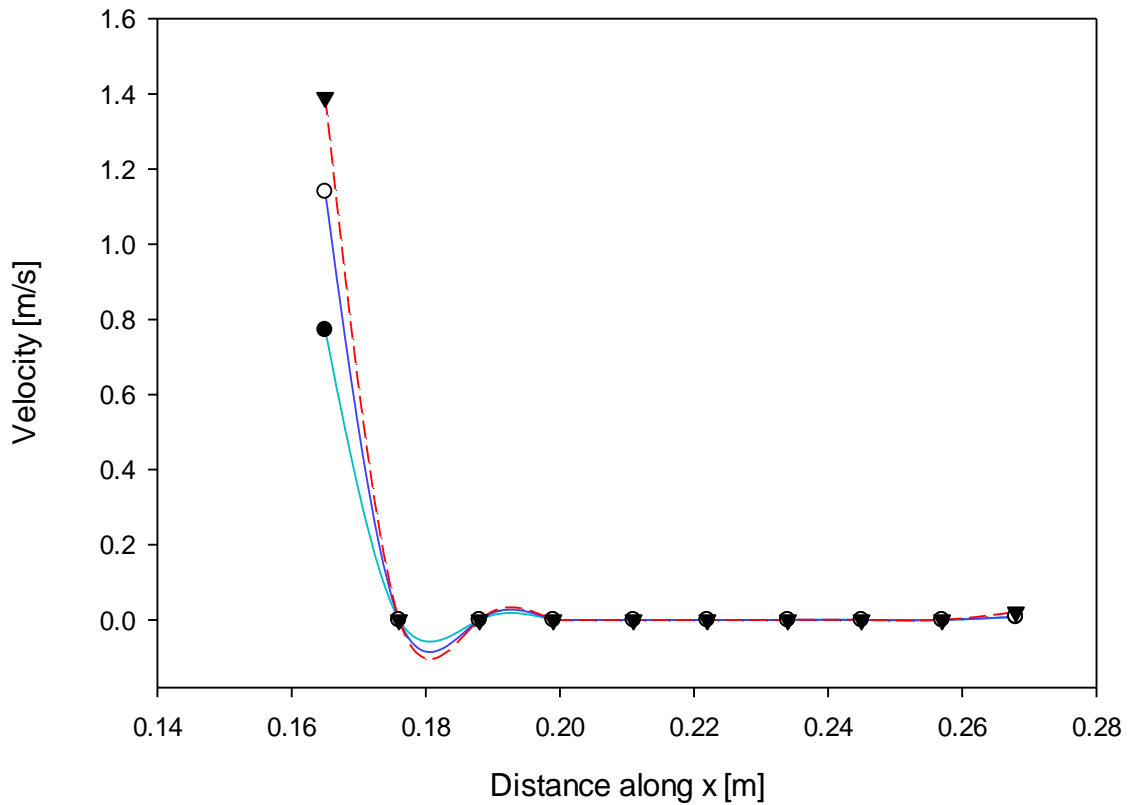


Figure 6.1: Velocity magnitude along the x-axis of the vane

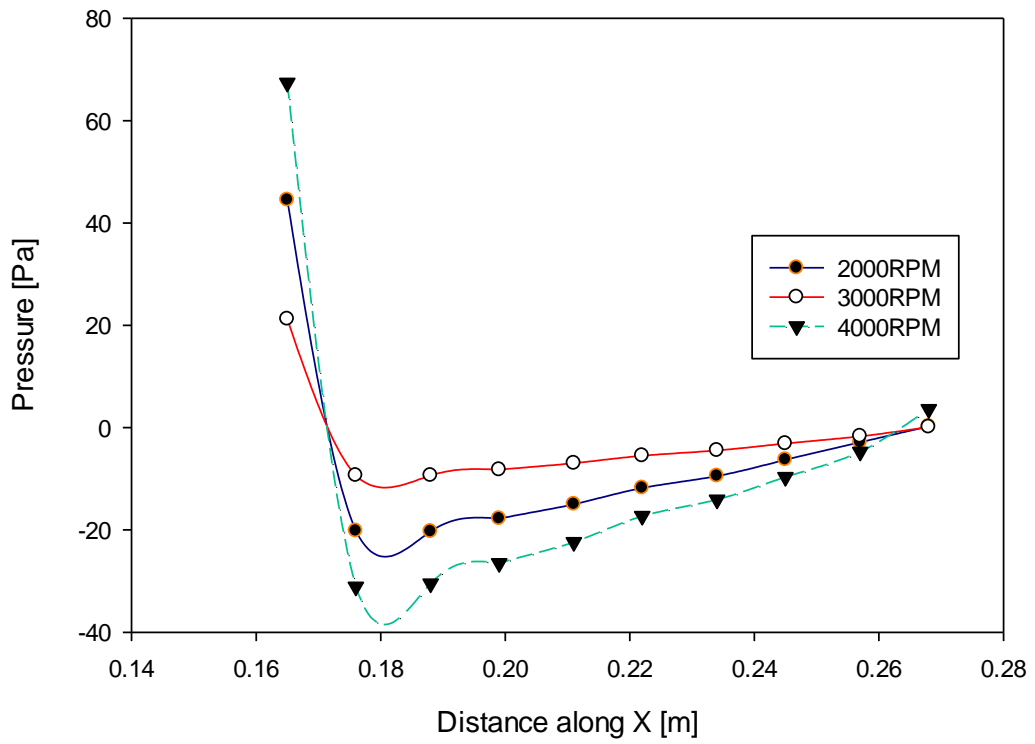


Figure 6.2: Pressure magnitude long x-axis of vanes

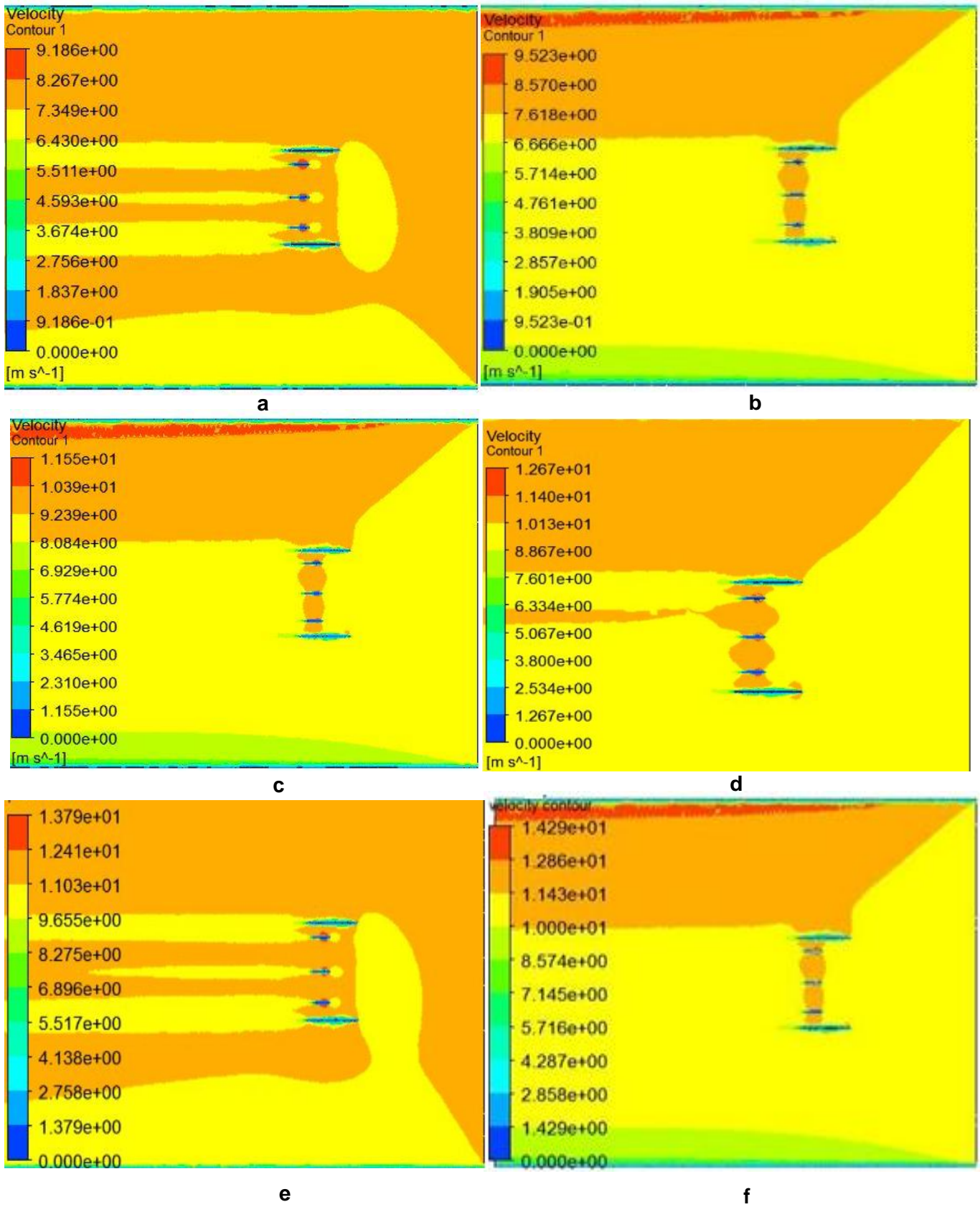


Figure 6.3 Velocity contour at different speed and vane deflection angle showing: (a) 2000 rpm, angle 1° ; (b) 2000 rpm, angle 5° ; (c) 3000 rpm, angle 3° ; (d) 3000 rpm, angle 5° ; (e) 4000 rpm, angle 1° ; and (f) 4000 rpm, angle 5°

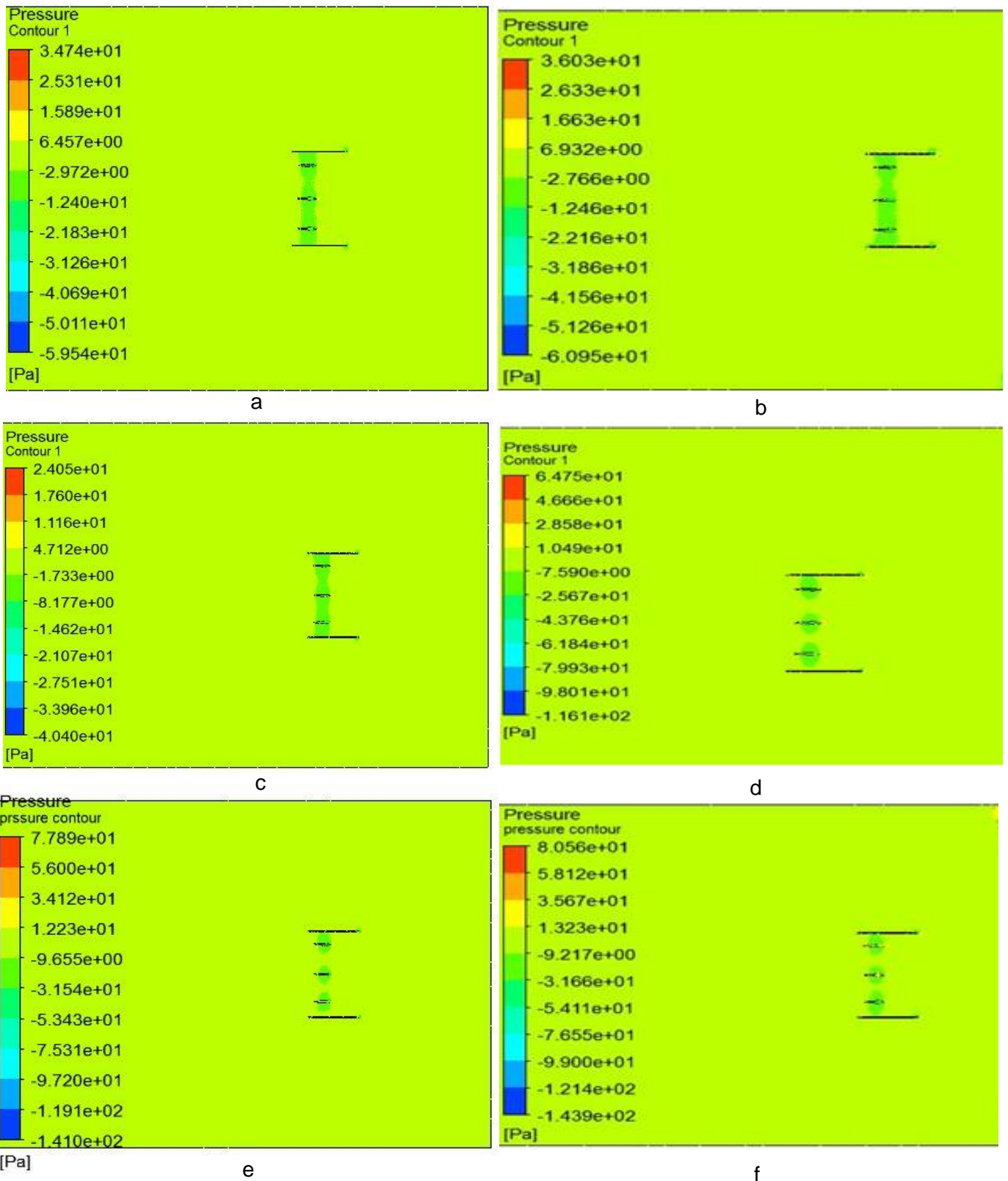


Figure 6.4 Pressure contour at different speed and vane deflection angle showing: (a) 2000 rpm, angle 1°; (b) 2000 rpm, angle = 5°; (c) 3000 rpm, angle = 3°; (d) 3000 rpm, angle = 5°; (e) 4000 rpm, angle = 1°; and (f) 4000 rpm, angle = 5°

6.2.2 Quantitative Result Analysis

This section discusses and gives details of the lift, drag, and moment characteristics of the designed TVC system. The analysis gives an insight into the possible outcome of the system in supporting the mission of shortening the ground roll distance of an aircraft causing it to take off earlier than normal. The section also explains the behavioural pattern of the system at the different rotational speeds of the propeller either to aid the rotation of or the lifting off the ground of the aircraft.

Since this aircraft can operate in different conditions which include rainy season and dry season where the environmental conditions differ, the author chooses to present the dimensionless result parameters (C_L and C_D) of the work. The reason being that it fits into the different conditions characterized by the density of the fluid.

6.2.2.1 TVCS Lift Characteristics Analysis

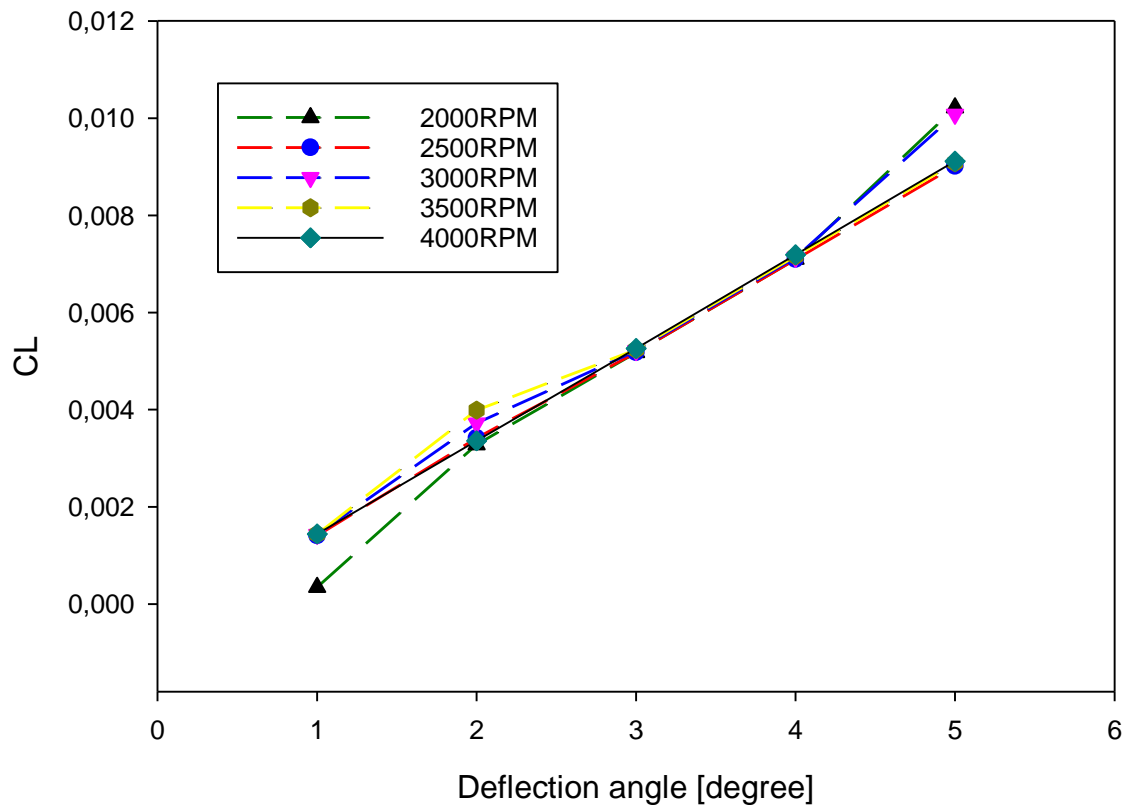


Figure 6.5 Coefficient of lift as a function of deflection angle

Figure 6.5 shows the lift characteristics of the TVC system analyzed. With the airfoil shaped vanes used as vectoring material, lift is anticipated, and the curve clearly shows that the TVC system was able to generate a considerable amount of lift. The lift generated increases with the propeller speed and vane deflection angles. However, the result revealed a close lift margin

between the speeds analyzed. The figure shows that the system lift generation was unstable from 1° deflection angle up until about 3° from which stability is observed up until 5°.

6.2.2.2 TVCS Drag Characteristics Analysis

The effect of vane deflection at angles of 0° to 5° generating a drag is shown in Figure 6.6. The system shows an increase in drag with an increase in vane deflection angle as anticipated. However, it is interesting to note that the drag generated at the speed of 4000 rpm is lower than that generated at 2000 rpm. This shows that the system can perform very well at full throttle of the vehicle.

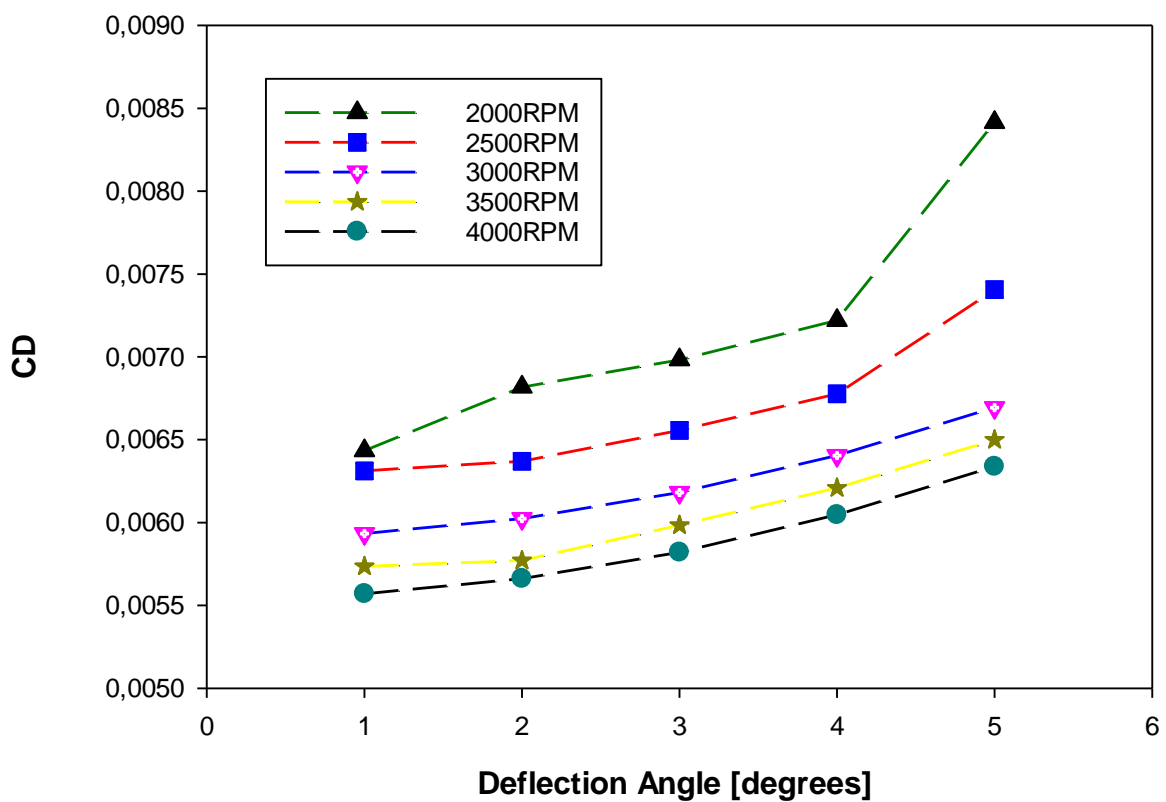


Figure 6.6: Coefficient of drag as a function of deflection angle

6.2.2.3 TVCS Pitching Moment Characteristics Analysis

The TVC system has a slight effect on the pitching moment and the result is displayed in Figure 6.7 for a deflection angle of 0° to 5°. Just like the lift, the analysis also records some significant pitching moment which increases with the increasing vanes deflection angle. From the speed of 2500 rpm to 4000 rpm, the moments generated are closely tied especially at a deflection angle of 3° from which the stability sets in. This stability range agrees with that shown in lift and drag characteristics.

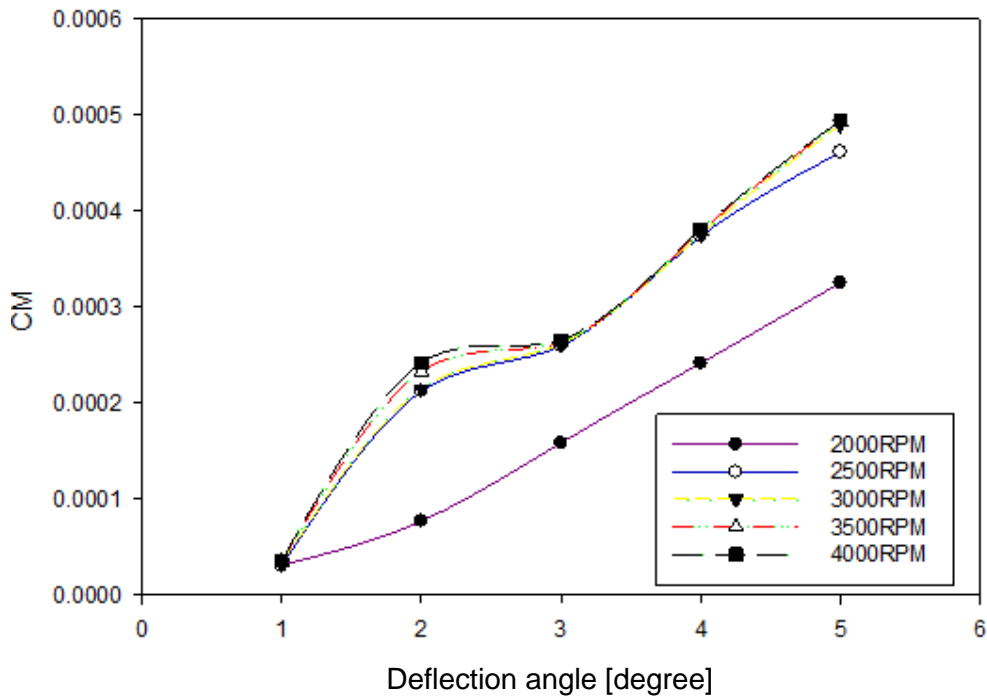


Figure 6.7: Moment coefficient of as a function of deflection angle

6.3 GII Operational Characteristics

Table 6.1 and Table 6.2 shows the operational characteristics of the GII UAV as obtained by Petersen (2010) in his research. He investigated the effect of morphing wings of the aircraft in the take-off and climb phase of the aircraft. This result presented here serves as the basis for the analysis of the current work. The present work was geared towards obtaining operational characteristics to augment one obtained by Petersen in his analysis work on the GII aircraft. Table 6.1 gives the maximum C_L and C_D at V_{LOF} of GII at different flaps angles. It also presents the power ratio and the power at the same flaps angles. Table 6.2 presents the climb operational parameters. The result of the current work presented in section 6.4 to 6.5 is the sum of the result presented in section 6.2.2.

Table 6.1 GII operational result 1 (Petersen, 2010)

	C_L (max)	CD	$C_L^{3/2} / CD$	Pr(W)
0 flaps/twist	0.43340512	0.04847896	5.895406	169.4339
5 flaps (CON)	0.5131869	0.06003207	6.144495	162.5653
10 flaps (CON)	0.58282592	0.07336955	6.086917	164.1031
15 flaps (CON)	0.64649101	0.08890013	5.854151	170.628

Table 6.2 GII operational result 2 (Petersen, 2010)

	CL	CD	$C_L^{3/2} / CD$	R/C (m/s)
0° Deflection	0.68	0.079	7.098005	6.910256

6.4 Aircraft Ground Roll and Take-off Performance Result

The analyses were aimed at generating lift to augment the AMTL UAV's entire lift and moment to aid quick rotation, take-off, and climb. All these were geared towards initiating take-off before the normal designed distance for the aircraft. A range of vane deflection angles and mass flowrates generated from propeller speeds was considered at normal configuration of the aircraft to ascertain the effect of the thrust vectoring system. The angles of 0° to 5°, mass flowrate 11.173kg/s to 23.329kg/s (Propeller speed 2000 rpm to 4000 rpm) analyzed gave a sense of the TVC system's performance and proves its usability as an add-on component to the aircraft. These range of vane deflection angles were analyzed on CON wing at a flaps angle of 0° to 15°. The system was run at both take-off and climb configuration using the sets of data mentioned above.

6.4.1 Take-off Performance of the Aircraft with TVC Configuration

The main aim of this designed work is to achieve a quick take-off of the AMTL UAV at the present designed configurations of 12kg gross take-off weight (GTOW) with a maximum of 60 N wing load. The TVC unit must be able to aid the take-off at a shorter ground roll and quick to attain safe clearance height of 15 m.

To determine these performances of the CPUT AMTL UAV, the general equations of motion and the associated equations presented in equation 1.1 to 1.9 were used. It is important to note that there are different approaches to deriving take-off equation of an aircraft. The different approaches give rise to different formulas used to calculate the ground roll.

6.4.1.1 Ground roll Distance of The Aircraft with TVC Configuration

The ground roll distance of an aircraft is dependent on factors such as the amount of lift generated by the wings, environmental factors, the runway conditions etc. The effectiveness and how quick the wings are in generating the needed lift to overcome the weight and then lift off the UAV is another important factor. The wings of the GII UAV has been designed and optimized, hence to achieve this short take-off capabilities, the author designed this TVC system under investigation. From the analysis, at 0° flaps configuration of the wing, the analysis yielded a significant result presented in Table 6.3. The GII aircraft (UAV) generates a maximum lift coefficient of 0.43089607 (Table 6.1) at $V_{stall} = 25.39$ m/s, and $V_{LO} = 30.468$ m/s at the point

of take-off. The designed TVC system generated 0.08% increase in the lift coefficient at the conditions of 0° flaps angle, 2000 rpm, and 1° vane deflection angle; and 2.07% at the conditions of 5° vane deflection angle and 4000 rpm. It has a corresponding drag with an increase of 11.72% and 11.56% respectively to the drag of the airframe. For vane deflection angles of 2 - 5° and flaps angles 5°, 10°, and 15°, the percentage increase in lift and drag are shown in Appendix C and D. Just like a typical aerodynamic system, the analysis proves that the system obeys the principles of aerodynamic expected of an airfoil shaped designed vanes. The TVC system generated lift at the deflection angles, propeller speeds and flaps angle analyzed. The lift generated supports the airframe lift to aids its early take-off by reducing the ground roll distance (S_g). Table 6.3 shows the total coefficients of lift (GII coefficients lift plus TVC system coefficient of lift) at flaps angle = 0°. It can be seen from the table that the C_L increases with propeller speed and vanes deflection angle as presented graphically in section 6.2.2, Figure 6.2 (TVC system lift coefficient only). The corresponding total drag is presented in Table 6.4 which also shows that the drag coefficient (C_D) is higher at higher propeller speed and vanes deflection angle. This also agrees with what was presented in section 6.2.2, Figure 6.6 (TVC system drag coefficient only). Furthermore, Table 6.5 to Table 6.10 show the lift and drag coefficient at 5°, 10°, and 15° flaps angle. In relation to the lift, drag, and moment characteristics presented in section 6.2.2, the yellow box in the Table 6.3 – 6.10 below bounds the range of data at which system operation became stable. The range within the red box is the optimal operation point of the system. The optimal points here imply the range at which the system is most stable and capable of supporting the aircraft mission target with TVC system.

Table 6.3 Total lift coefficient (GII & TVC) at 0° flap

	2000 RPM	2500 RPM	3000 RPM	3500 RPM	4000 RPM
Vane angle (degree)					
1	0,43124489	0,43230502	0,43232651	0,43233419	0,43233719
2	0,43417492	0,43431146	0,43461979	0,43488724	0,43425489
3	0,43607885	0,43607841	0,43611334	0,43613619	0,43615989
4	0,43799662	0,43799135	0,43803128	0,43805948	0,43808757
5	0,44111055	0,43990993	0,44097227	0,4399788	0,44001131

Table 6.4 Total drag coefficient (GII & TVC) at 0° flap

	2000 RPM	2500 RPM	3000 RPM	3500 RPM	4000 RPM
Vane angle (degree)					
1	0.05491296	0.05478996	0.05441196	0.05421396	0.05404896
2	0.05529796	0.05484796	0.05450296	0.05424996	0.05413996
3	0.05546296	0.05503496	0.05465996	0.05446296	0.05429896
4	0.05569996	0.05525596	0.05488296	0.05468796	0.05452496
5	0.05989496	0.05588496	0.05517196	0.05497796	0.05481696

Table 6.5 Total lift coefficient (GII & TVC) at 5° flap

	2000 RPM	2500 RPM	3000 RPM	3500 RPM	4000 RPM
Vane angle (degree)					
1	0,5111370	0,51219713	0,43232651	0,43233419	0,43233719
2	0,51406703	0,51420357	0,43461979	0,43488724	0,43425489
3	0,51597096	0,51597052	0,43611334	0,43613619	0,43615989
4	0,51788873	0,51788346	0,43803128	0,43805948	0,43808757
5	0,52100266	0,51980204	0,44097227	0,4399788	0,44001131

Table 6.6 Total drag coefficient (GII & TVC) at 5° flap

	2000 RPM	2500 RPM	3000 RPM	3500 RPM	4000 RPM
Vane angle (degree)					
1	0.06646607	0.06634307	0.06596507	0.06576707	0.06560207
2	0.06685107	0.06640107	0.06605607	0.06580307	0.06569307
3	0.06701607	0.06658807	0.06621307	0.06601607	0.06585207
4	0.06725307	0.06680907	0.06643607	0.06624107	0.06607807
5	0.07144807	0.06743807	0.06672507	0.06653107	0.06637007

Table 6.7 Total lift coefficient (GII & TVC) at 10° flap

	2000 RPM	2500 RPM	3000 RPM	3500 RPM	4000 RPM
Vane angle (degree)					
1	0,58058299	0,58164312	0,58166461	0,58167229	0,58167529
2	0,58351302	0,58364956	0,58395789	0,58422534	0,58359299
3	0,58541695	0,58541651	0,58545144	0,58547429	0,58549799
4	0,58733472	0,58732945	0,58736938	0,58739758	0,58742567
5	0,59044865	0,58924803	0,59031037	0,58931690	0,58934941

Table 6.8 Total drag coefficient (GII & TVC) at 10° flap

	2000 RPM	2500 RPM	3000 RPM	3500 RPM	4000 RPM
Vane angle (degree)					
1	0.07980355	0.07968055	0.07930255	0.07910455	0.07893955
2	0.08018855	0.07973855	0.07939355	0.07914055	0.07903055
3	0.08035355	0.07992555	0.07955055	0.07935355	0.07918955
4	0.08059055	0.08014655	0.07977355	0.07957855	0.07941555
5	0.08478555	0.08077555	0.08006255	0.07986855	0.07970755

Table 6.9 Total lift coefficient (GII & TVC) at 15° flap

	2000 RPM	2500 RPM	3000 RPM	3500 RPM	4000 RPM
Vane angle (degree)					
1	0,64289656	0,64395669	0,64397818	0,64398586	0,64398861
2	0,64582659	0,64596313	0,64627146	0,64653891	0,645906561
3	0,64773052	0,64773008	0,64776501	0,64778786	0,647811564
4	0,64964829	0,64964302	0,64968295	0,64971115	0,649739237
5	0,65276222	0,6515616	0,65262394	0,65163047	0,651662978

Table 6.10 Total drag coefficient (GII & TVC) at 15° flap

	2000 RPM	2500 RPM	3000 RPM	3500 RPM	4000 RPM
Vane angle (degree)					
1	0.09533413	0.09521113	0.09483313	0.09463513	0.09447013
2	0.09571913	0.09526913	0.09492413	0.09467113	0.09456113
3	0.09588413	0.09545613	0.09508113	0.09488413	0.09472013
4	0.09612113	0.09567713	0.09530413	0.09510913	0.09494613
5	0.10031613	0.09630613	0.09559313	0.09539913	0.09523813

6.4.1.2 Percentage Reduction of the Take-off Distance

There was a significant reduction in the take-off distance observed across the vane deflection angles, flaps angles, and the propeller speed analyzed. This section describes the overall reduction of *the S_g* with due consideration to the whole factors contributing to the reduction. This is shown in Figure 6.9, 6.10 and 6.11 at α value of 0.000, 0.008 and 0.024 respectively. These figures show the effect of propeller speed and vane deflection angle on *S_g*. As shown, *S_g* reduction drops with increase in deflection angle at all propeller speeds analyzed. At 0° flaps angle, 2000 rpm and 1° deflection angle, *S_g* was reduced by 78.16% and 78.69% at the same vanes and flaps deflection angle but at 4000 rpm propeller speed.

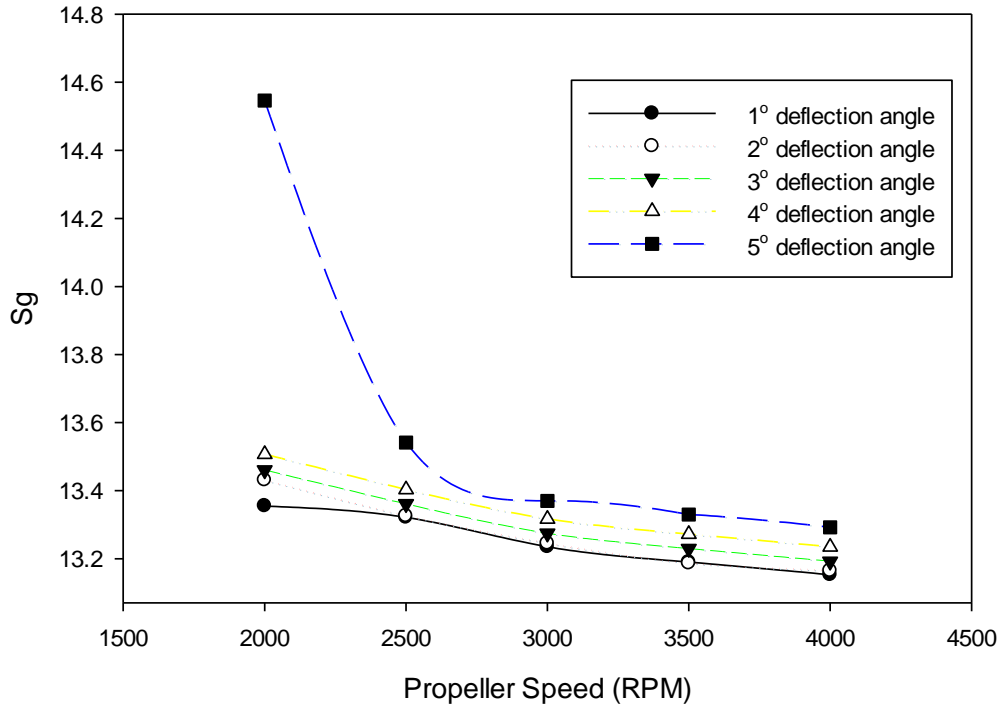


Figure 6.8 Enlarged plots of S_g v. propeller speed

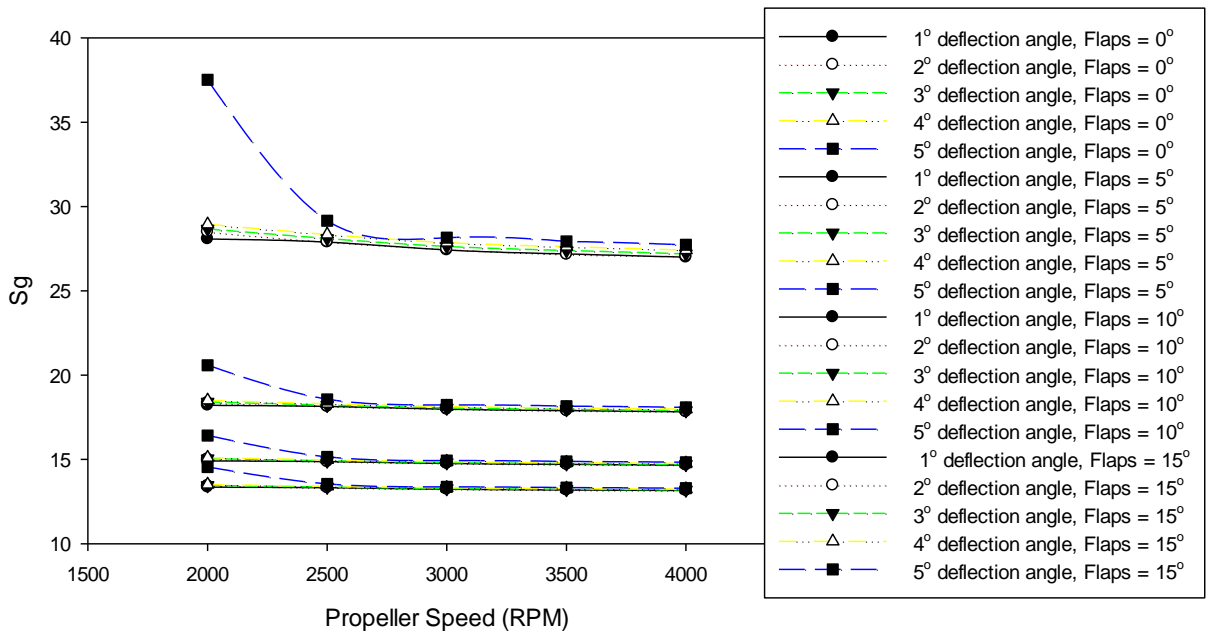


Figure 6.9 Take-off distance (S_g) reduction at $\alpha = 0.000$

At 5° degree vanes deflection angles, 2000 rpm, and 0° flaps angle; S_g is reduced by 75.21%, and 78.32% at 4000 rpm at the same 5° vane deflection angle. At 4000 rpm propeller speed, and 15° flaps, the system reduces S_g by 78.01%. From Figure 6.11, at α value 0.008, the

reduction is 75.94% at 2500 rpm, and 76.10% at 3500 rpm when the vanes are maintained at 3° and 4° respectively, and at 10° flaps. The aircraft acquires 0.89% and 1.22% increase in C_{Lmax} to achieve the above-mentioned percentage in reduction. However, the increase in C_{Lmax} came with 8.20% and 7.80% increase in drag at 2500 rpm and 3500 rpm respectively. This trend in S_g reduction holds the same in all the angles analyzed as shown in Figure 6.12 and other graphs in appendix B

Meanwhile, the system supports short take-off better at 1° vane deflection angle and increases with increase in propeller speed, but the result displayed in Figure 6.5 (section 6.2.2) shows some level of instability at the propeller speeds from 2000 rpm and vane deflection angles of 3° and below. The stability of the system starts from 3° and 2500 rpm and above, hence the operation of the TVC system should be maintained as from 3° and above, depending on the operational parameters at the disposal of the pilot.

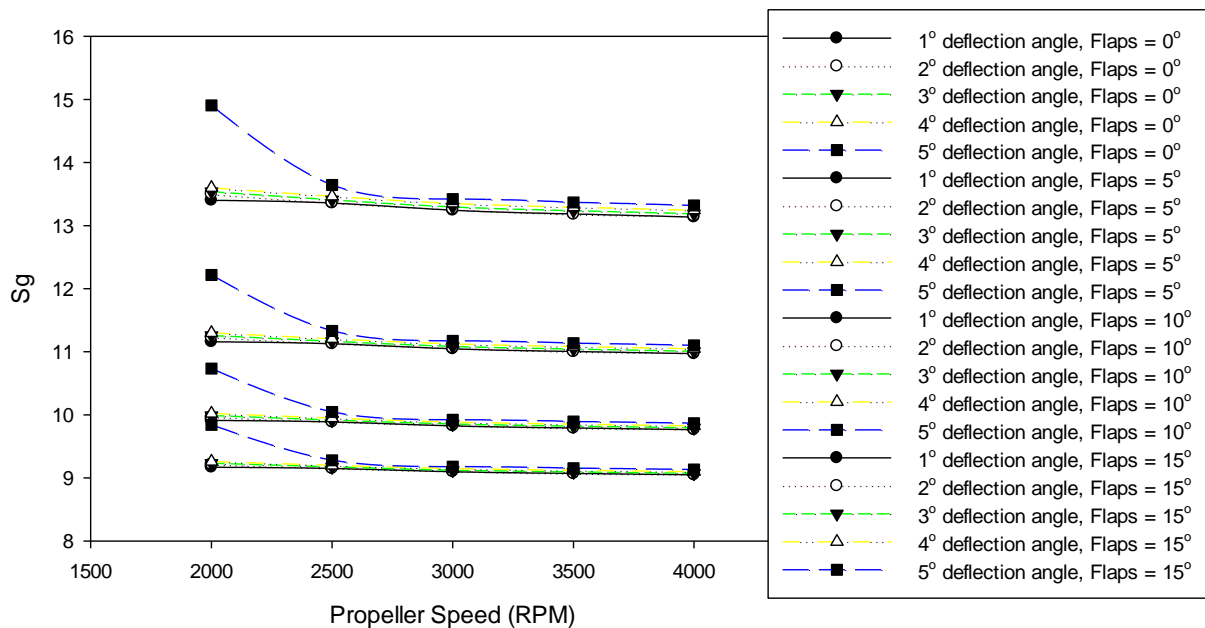


Figure 6.10 Take-off distance (S_g) reduction at $\alpha = 0.008$

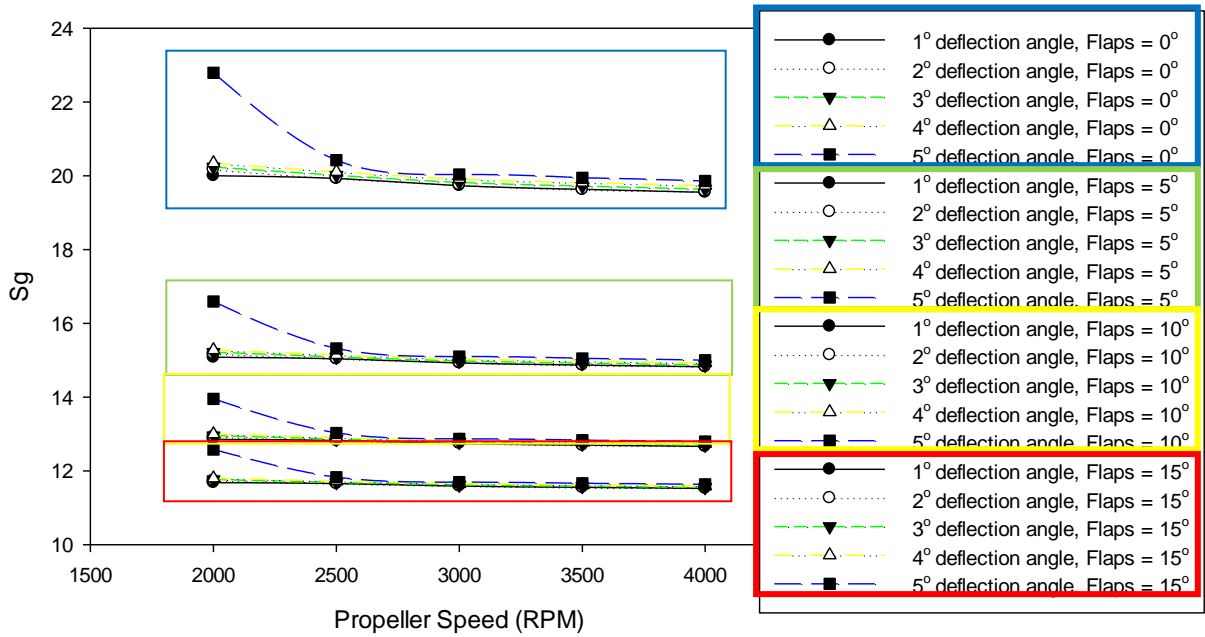


Figure 6.11 Take-off distance (Sg) reduction at a = 0.024

The trend of reduction of the Sg with respect to the vane deflection angles, propeller speed, and the flaps angles is uniform across all the groups of quantities analysed. The behavioural pattern is shown in Figure 6.12 with the trend lines displayed.

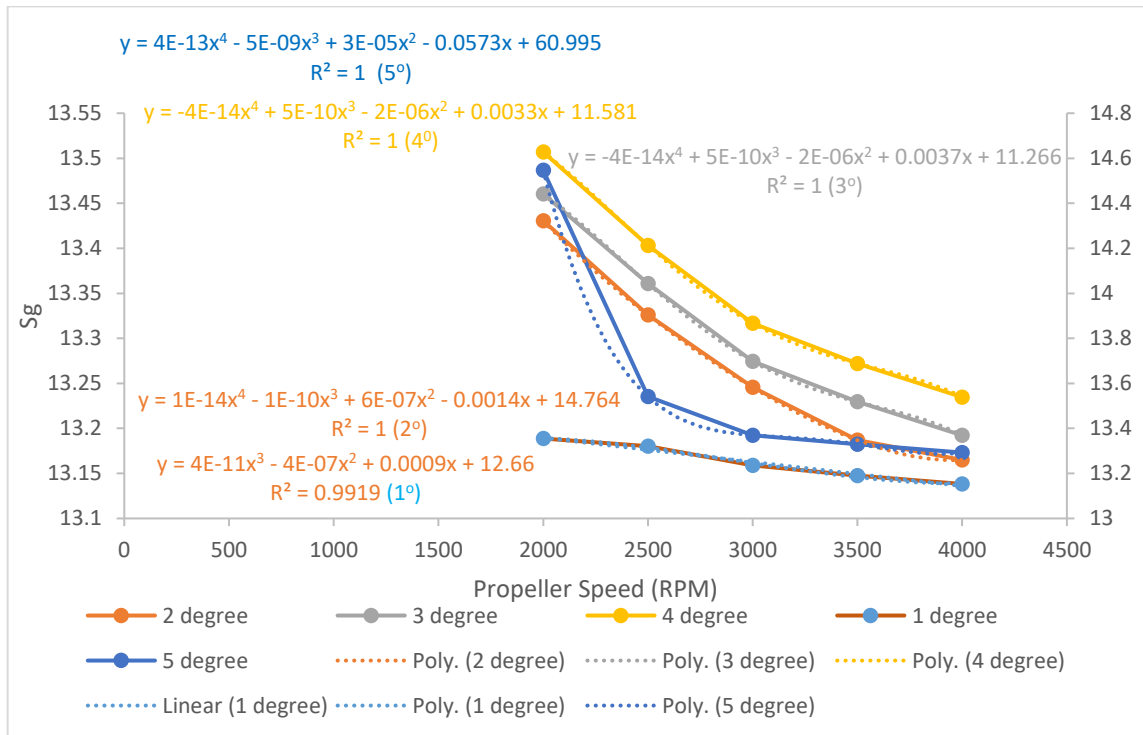


Figure 6.12 Take-off distance reduction pattern of TVC system

The trendline shows that the generated equation accurately fit the behavioural pattern of S_g dependent on the propeller speed. A polynomial equation of 4th degree order fits the curve for 2°, 3°, 4°, and 5° accurately with a close match of power values and slight difference in the constants of the equation. Due to the close linearity of the behavioural pattern of 1° curve, a 3rd degree order polynomial equation perfectly fit the curve. The general fourth order polynomial equation governing the ground roll reduction behavioural pattern when it is matched against the propeller speed is shown below.

$$y = ax^4 - bx^3 - cx^2 - dx + e \quad \text{Equation 6.1}$$

The most important factor showing the accuracy of the curve fit is the R square value. This value shows how the curve equation captures the points, it hence can be used as a mathematical model to calculate S_g when the propeller speed and the vane deflection angles are known.

6.4.1.3 Aircraft Thrust Value Study Analysis

The performance of an aircraft during operation and most especially at take-off phase is dependent on the thrust generated by the propulsion system. The difference between the thrust at take-off and the static thrust either shortens or extends the ground roll (S_g) distance of the aircraft before take-off. The performance of the vehicle and its endurance is determined by how quick it can take off from the ground into the air. The shorter the S_g , the more an aircraft such as the CPUT demonstrator is desired. For an aircraft to take off at a shorter distance, the difference between the total thrust and the static thrust must be large. The take-off thrust is calculated from equation 1.7, as repeated below.

$$T = T_0 - \alpha V^2 \quad \text{Equation 1.7}$$

Where T is total thrust at take-off, T_0 is the static thrust, and α is a constant which can be either positive or negative.

The larger the thrust difference at a constant speed of the aircraft, the smaller the value of α , and the shorter the S_g . That means the distance an aircraft will roll before take-off is dependent on the value of α and their relationship is directly proportional. The study conducted for α value

of α from -0.002 to 0.0402 reveals that S_g reduces with a reduction in α value and vice visa. However, the configuration gives an undesirable result at any value beyond 0.03129. This finding holds true irrespective of the flaps angle, vane deflection angle and the propeller speed. Figure 6.8 shows a relationship and effect of α value on S_g . From the figure, we can deduce that S_g of an aircraft increases with increase in the α value. That means, for an optimum take-off of an aircraft at short ground roll distance, the thrust generated by the propulsion system up to the point of take-off must be high as the high thrust creates a wider difference between the thrust at lift-off and the static thrust, thereby making the α value large. The curve shows that S_g increases with increase in α value until a point where the S_g changes with further change in α value. It then suggests that the difference in thrust has a limit to which it influences the S_g after which S_g increases to infinity without further change in thrust. Figure 6.14 shows the change in response time of the aircraft at different thrust value. The shaded area represents the time difference at take-off, at different thrust, and at different vanes deflected angles. The time saves amounts to the ground roll reduction and the increase in the aircraft endurance.

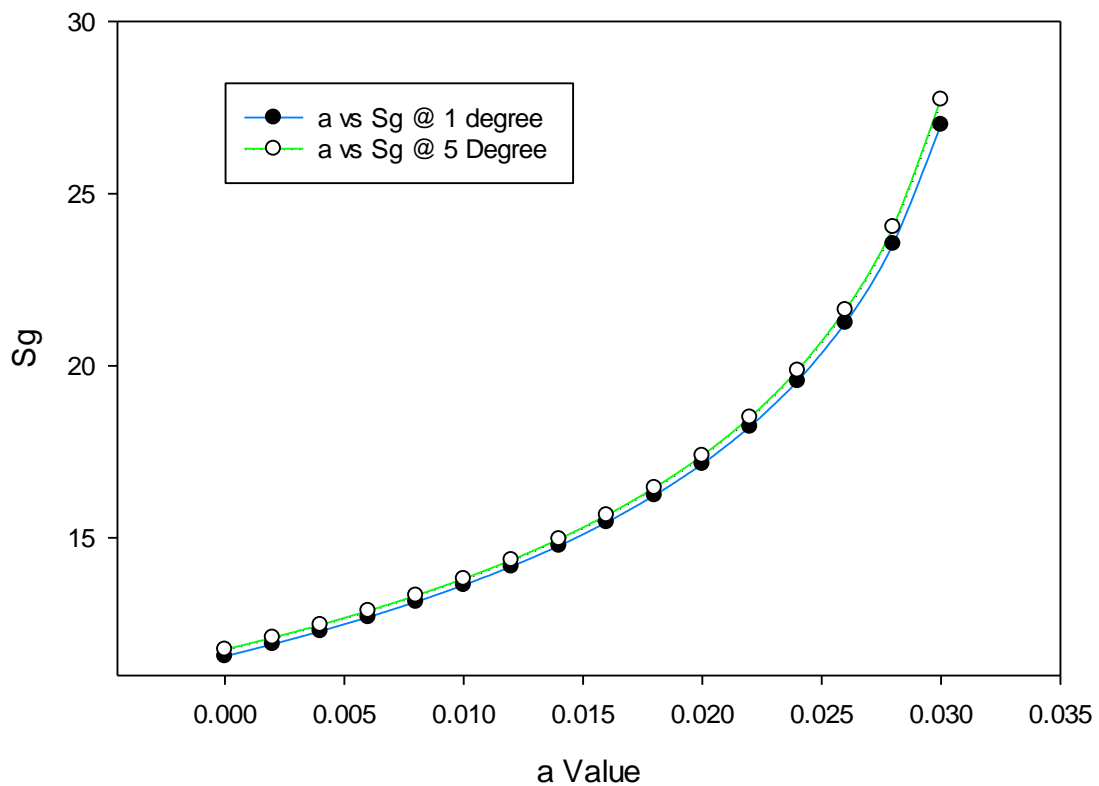


Figure 6.13 S_g v α value @ 4000 rpm

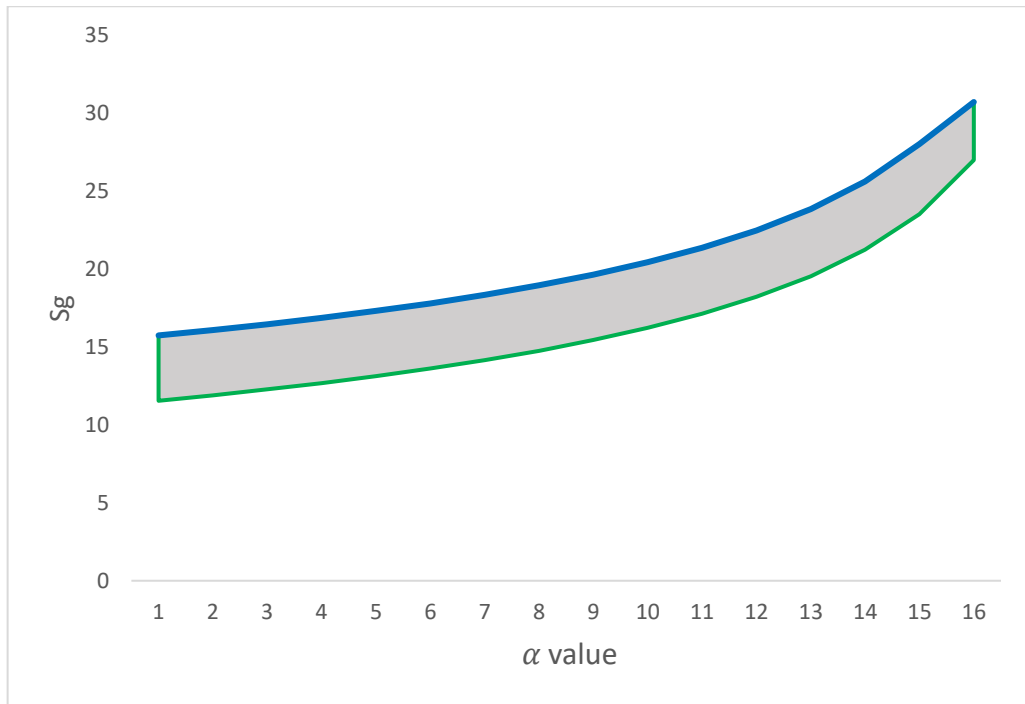


Figure 6.14 Sg reduction behavioural curve

6.5 Aircraft Climb Performance Analysis

The analyses were aimed at generating enough aerodynamic characteristics to get the aircraft to get the aircraft to the cruise height after a quick rotation and lift off. It can be inferred that a quick climb rate improves the aircraft performance and endurance. Furthermore, it reduces the fuel consumption and extends the flight time to support a long mission objective. To get the aircraft up as quick as possible, the power consumption must be low, and this means that the power ratio ($C_L^{3/2}/C_D$) must be high. Based on the range of parameters (11.173kg/s to 23.329kg/s (Propeller speed 2000 rpm to 4000 rpm)) analyzed, the system shows a reduction in power usage when an aircraft is equipped with TVC system. In a nutshell, the power usage during the first two phases of the aircraft operation was obtained by using equation 6.2.

$$P_r = \sqrt{\frac{2W^3 C_D^2}{\rho_\infty S C_L^3}} \left(\frac{C_D}{C_L^{3/2}} \right) \quad \text{Equation 6.2}$$

Table 6.11 to Table 6.18 present the values of the power (P_r) usage and the percentage reduction of the current system to that of GII without TVC system. As shown in Table 6.12, at flaps angle 0°, the percentage reduction of the power usage increases from 59.89% at vane deflection angle of 1° to 60.60% at 4° vane deflection angle before it drops to 55.39% at a

propeller speed of 2000 rpm. This trend of percentage drop only happens at 200 rpm and 2500 rpm propeller speed. From 3000 rpm to 4000 rpm, the power usage increases steadily with the propeller speed and the vane deflection angle. This trend holds same in flaps angle 5°, 10° and 15° as shown in Table 6.14, Table 6.16, and Table 6.18.

Table 6.11 Power at different propeller speed and at 0° Flaps Angles

		2000 RPM	2500 RPM	3000 RPM	3500 RPM	4000 RPM
Flaps angle (degree)	Vane deflection (degree)					
0	1	67.9602884	67.1625215	66.2291796	65.7445688	65.3436394
	2	67.5386316	66.3815946	65.4105185	64.6858613	64.7040299
	3	67.0612971	66.0304843	65.1181463	64.6395024	64.2403874
	4	66.7561131	65.6984496	64.7968419	64.3248584	63.9297543
	5	75.5760457	66.3322071	64.1869335	64.1665946	63.77727

Table 6.12 Power Percentage Reduction at different propeller Speed and at 0° Flaps Angles

		2000 RPM	2500 RPM	3000 RPM	3500 RPM	4000 RPM
Flaps angle (degree)	Vane deflection (degree)					
0	1	59.89%	60.36%	60.91%	61.20%	61.43%
	2	60.14%	60.82%	61.39%	61.82%	61.81%
	3	60.42%	61.03%	61.57%	61.85%	62.09%
	4	60.60%	61.22%	61.76%	62.04%	62.27%
	5	55.39%	60.85%	62.12%	62.13%	62.36%

Table 6.13 Power at different propeller speed and at 5° Flaps Angles

		2000 RPM	2500 RPM	3000 RPM	3500 RPM	4000 RPM
Flaps angle (degree)	Vane deflection (degree)					
5	1	24.4429383	24.3297989	24.3275127	24.3266955	24.3263766
	2	24.1319354	24.1175717	24.085178	24.0571263	24.1235216
	3	23.9326697	23.9327156	23.9290803	23.926702	23.9242362
	4	23.7341654	23.7347079	23.7305988	23.727697	23.7248068
	5	23.4164977	23.5383048	23.4304842	23.5312946	23.5279867

Table 6.14 Power Percentage Reduction at different propeller Speed and at 5° Flaps Angles

		2000 RPM	2500 RPM	3000 RPM	3500 RPM	4000 RPM
5	Vane deflection (degree)					
	1	84.96%	85.03%	85.04%	85.04%	85.04%
	2	85.16%	85.16%	85.18%	85.20%	85.16%
	3	85.28%	85.28%	85.28%	85.28%	85.28%
	4	85.40%	85.40%	85.40%	85.40%	85.41%
	5	85.60%	85.52%	85.59%	85.53%	85.53%

Table 6.15 Power at different propeller speed and at 10° Flaps Angles

		2000 RPM	2500 RPM	3000 RPM	3500 RPM	4000 RPM
10	Vane deflection (degree)					
	1	28.2477543	28.0700757	27.8709481	27.7671487	27.6810731
	2	28.135005	27.8872689	27.6763984	27.5178689	27.5271057
	3	28.0183254	27.7977306	27.6010691	27.4974202	27.4107214
	4	27.9380351	27.7109554	27.5158854	27.4132796	27.3271195
	5	29.7604445	27.8321792	27.3595	27.3631321	27.2779855

Table 6.16 Power Percentage Reduction at different propeller Speed and at 10° Flaps Angles

		2000 RPM	2500 RPM	3000 RPM	3500 RPM	4000 RPM
10	Vane deflection (degree)					
	1	82.79%	82.89%	83.02%	83.08%	83.13%
	2	82.86%	83.01%	83.13%	83.23%	83.23%
	3	82.93%	83.06%	83.18%	83.24%	83.30%
	4	82.98%	83.11%	83.23%	83.30%	83.35%
	5	81.86%	83.04%	83.33%	83.33%	83.38%

Table 6.17 Power at different propeller speed and at 15° Flaps Angles

		2000 RPM	2500 RPM	3000 RPM	3500 RPM	4000 RPM
15	Vane deflection (degree)					
	1	29.8048664	29.6396846	29.463051	29.3709865	29.2946584
	2	29.683614	29.4629935	29.2737416	29.1311605	29.1439928
	3	29.5664194	29.3707617	29.1960335	29.103895	29.0267815
	4	29.4814521	29.2799822	29.1065498	29.0152563	28.9385543
	5	31.0758002	29.3738921	28.9465763	28.956908	28.8810431

Table 6.18 Power Percentage Reduction at different propeller Speed and at 15° Flaps Angles

		2000 RPM	2500 RPM	3000 RPM	3500 RPM	4000 RPM
15	Vane deflection (degree)					
	1	82.53%	82.63%	82.73%	82.79%	82.83%
	2	82.60%	82.73%	82.84%	82.93%	82.92%
	3	82.67%	82.79%	82.89%	82.94%	82.99%
	4	82.72%	82.84%	82.94%	83.00%	83.04%
	5	81.79%	82.78%	83.04%	83.03%	83.07%

The power usage across all the flaps angles analysed varies between $\pm 0.01\%$ and $\pm 0.1\%$. The significant point noticed is that the power usage is constant at the following conditions: 3° and 4° vane deflection at 2000 rpm to 3500 rpm, and from 5°-15° flaps angles. The most stability is recorded at 15° flaps angle.

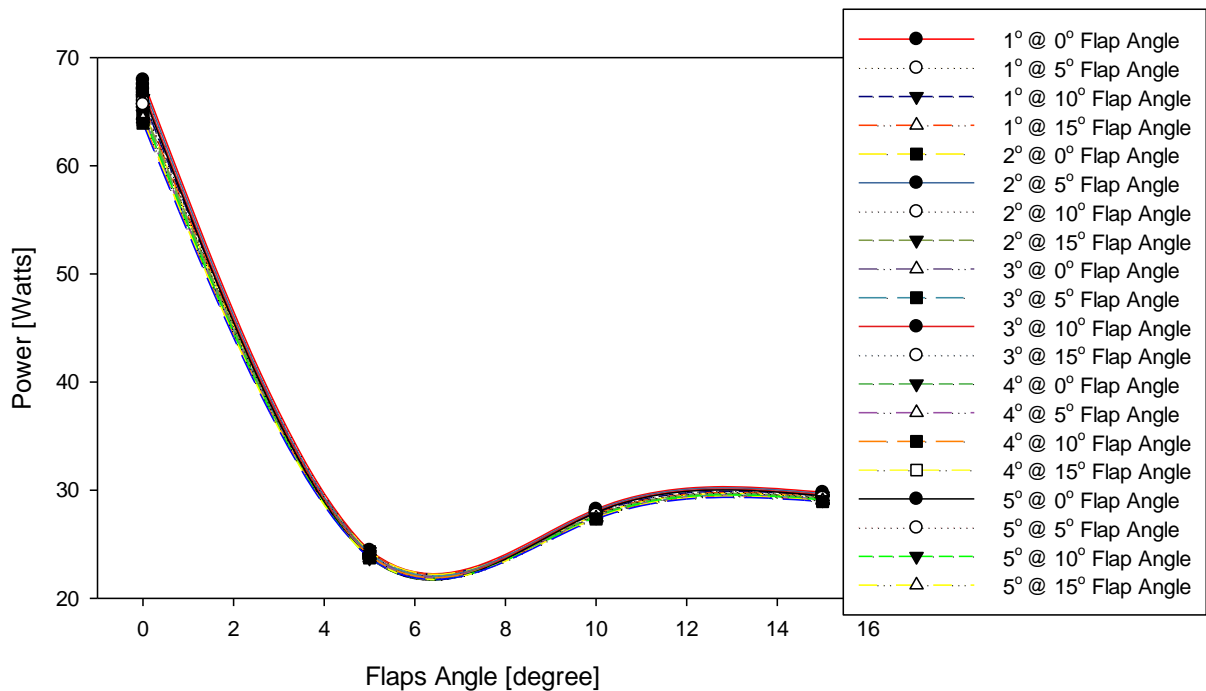


Figure 6.15 GII with TVCS power at 2000 rpm - 4000 rpm

Moreover, The P_r dependent on the flaps angle and the vane deflection angles is shown in Figure 6.15. It can be deduced that P_r usage drops as the flaps angle increase between 0° and 6° before a slight increase between 6° and 10° before it normalized at constant P_r . That means, with this system fitted on GII UAV, the power usage does not change with an increase in flaps angle. An important trend noticeable from Figure 6.15 is that power usage is constant across

the propeller speeds analyzed. The power usage behaviour can be related with the velocity variation across the length of the vane as shown in Figure 6.2 (section 6.2). Another important thing to note is that a stable/constant power obtained at between angle 3 and 4° and propeller speed of 2000 rpm and 3500 rpm as shown in Table 6.17. That shows the optimal point to maintain this UAV operation when controlled by TVC system so as to avoid an increase in power that does not amount to increase in operational efficiency.

In relation to the TVC system vane deflection angles, Figure 6.16 shows that P_r usage decreases with increase in vanes deflection angles and an increase in propeller speed. However, the stability is obtained from 3000 rpm to 4000 rpm and vane deflection angles of 3° to 5°. This agrees with all the presentations made in terms of the lift, drag, and moment in section 6.2.2

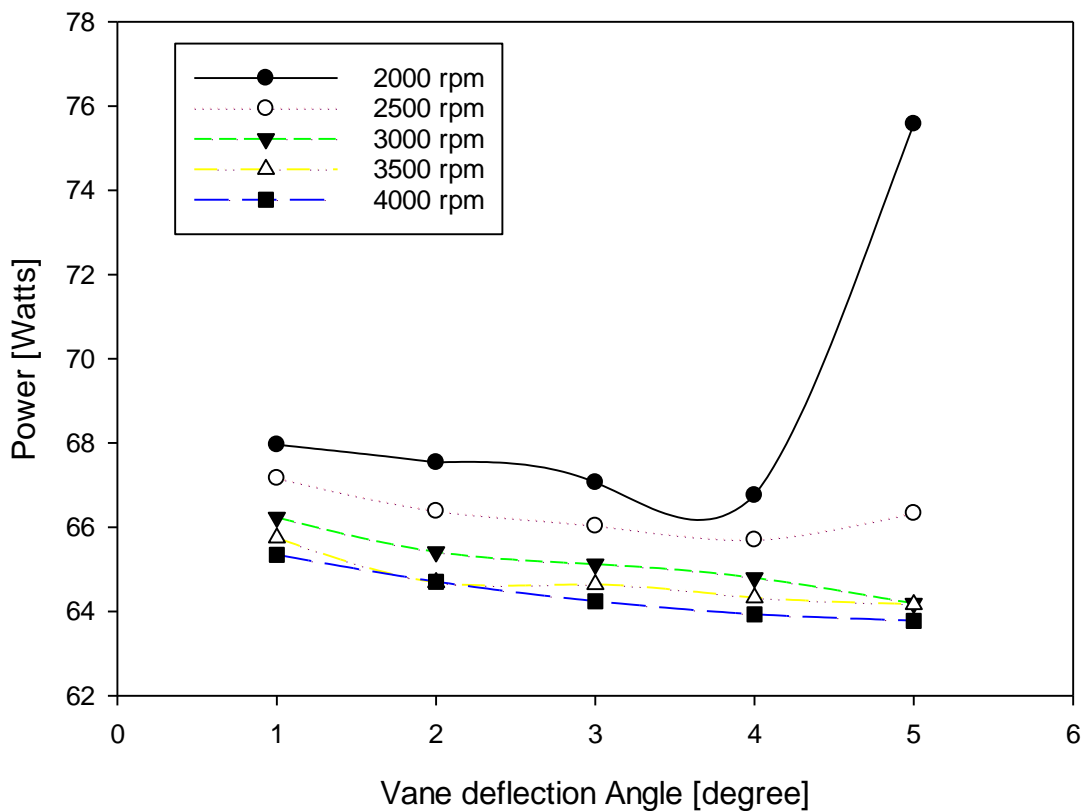


Figure 6.16 GII power at 0° flaps angle

The power usage has direct effect on the time taken for the aircraft to clear obstacle and begin to cruise. The equation 6.3 used to obtain the rate of climb shows that the drag polar of the system affects the performance of the aircraft. This translates into the power ratio $(C_L^{3/2}/C_D)$ which determines the aircraft rapid response and performance at all stages of the flight.

Table 6.19 Power difference across the vane angle and propeller speed

	Vane Angles	2000 RPM	2500 RPM	3000 RPM	3500 RPM	4000 RPM
15	2-1	0.0007	0.0010	0.0011	0.0014	0.0009
	3-2	0.0007	0.0005	0.0005	0.0002	0.0007
	4-3	0.0005	0.0005	0.0005	0.0005	0.0005
	5-4	-0.0093	-0.0006	0.0009	0.0003	0.0003
		0.0003	0.0001	0.0003	-0.0005	-0.0009
		-0.0001	-0.0001	-0.0003	0.0005	-0.0007
		0.0000	0.0000	0.0000	0.0000	-0.0005
		0.0088	0.0015	-0.0006	0.0000	-0.0003

$$R/C = \frac{TV_{climb}}{W} - \left(\frac{C_D}{C_L^{3/2}} \right) \sqrt{\frac{2}{\rho_\infty} \frac{W}{S}} \quad \text{Equation 6.3}$$

Figure 6.17 and Figure 6.18 show the relationship between rate of climb, flaps angle, and the vane deflection angle. The rate of climb increases with flaps angle to a maximum at around 6° to 8° before it drops until it reaches a flaps angle of 10° before maintaining a steady rate of climb at further increase in flaps angle (Figure 6.17). In relation to the vane deflection angles, the rate of climb increases with propeller speed and vane deflection angles (Figure 6.18).

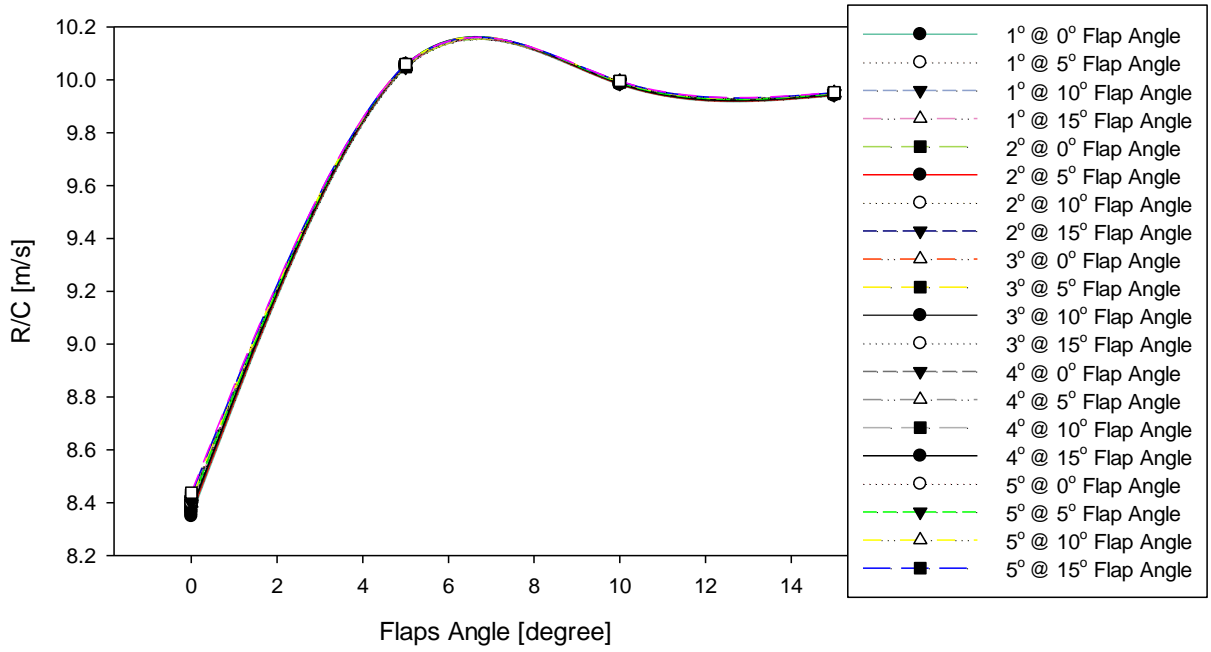


Figure 6.17 Rate of Climb to the Flaps Angles @ 2000 – 4000 rpm

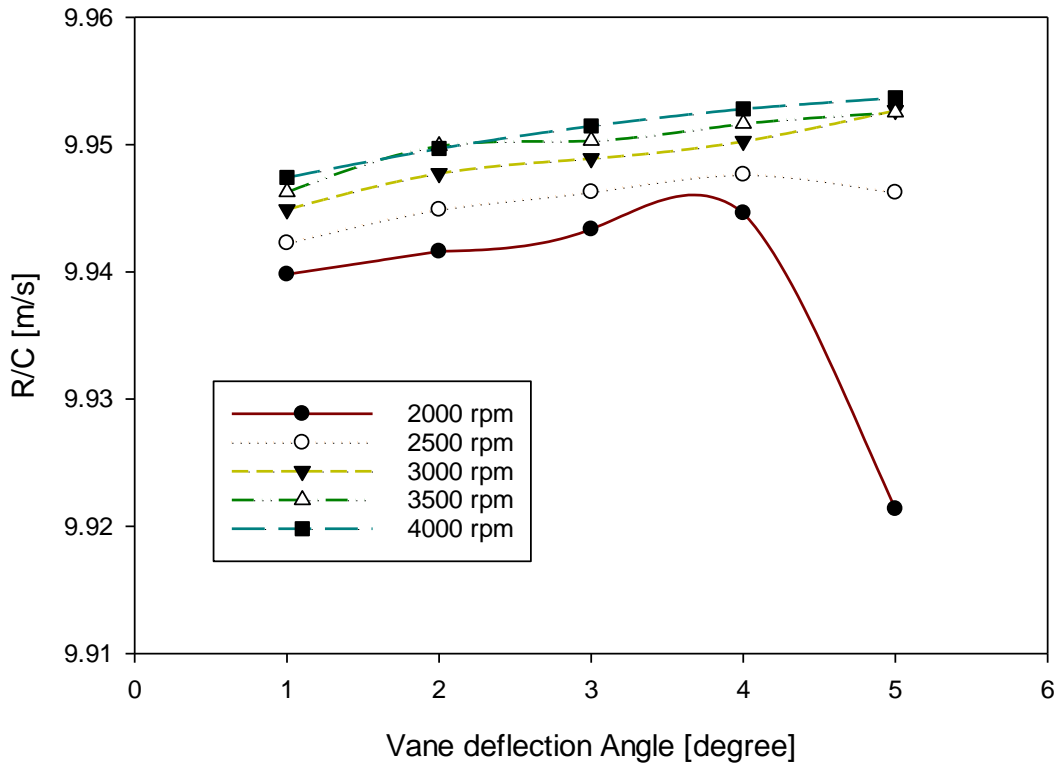


Figure 6.18 Rate of climb to the vane deflection angles

6.6 Result Summary

It is evident from the plots presented in Figure 6.6, Figure 6.7, and Figure 6.8 that the TVC system did generate some aircraft operation characteristics capable of maneuvering the vehicle. These operational characteristics are meant to augment that generated by the aircraft control surfaces. From the plots, it is noticeable that the lift and moment generated differ at different propeller rotational speed and vane deflection angles. However, the stability of the parameters occurs from 3° - 4° vane deflection angles and propeller speed from 3000 rpm – 4000 rpm. Hence this range of vane angle is the optimum to be maintained at take-off operations to achieve its purpose of augmenting the control surfaces of the aircraft for premature take-off. The angle to maintain between 3° and 4° will depend on the environmental conditions (wind speed, runway condition, humidity, temperature, etc.) available at pilot's disposal and how they affect the aircraft performance irrespective of the aircraft operating speed. Furthermore, the stable angle range is also evident on the moment, power, and rate of climb. As shown from figures presented in section 6.3 – 6.5, The UAV attains its optimum performance in terms of the power required for the take-off runs and the climbing operation at this range of vane angles and propeller speed.

CHAPTER SEVEN: CONCLUSION AND RECOMMENDATION

7.1 Conclusion

This work presents a successful conceptual design of a thrust vectoring control system to be integrated onto the CPUT AMTL developed UAV technology demonstrator. This project is the first stage of the design process towards achieving a STOL UAV for multipurpose application.

The main aim of the project was to design a TVC system and test its ability to affect the attitude of the UAV at the take-off and climb phase of the flight operation whilst Analyzing it to determine how it causes the quick rotation, the ground roll and the lifting off in order to get into the air as quick as possible. This is geared towards making the UAV application possible as a vehicle for parcel delivery, agricultural activities, medical emergency, search and rescue, security surveillance and numerous other possible areas of application. The concluding results are presented, focusing on $3^\circ - 5^\circ$ vane deflection angle, and 3000 – 4000 rpm propeller speed which are mostly important.

7.1.1 Thrust Vectoring Method Selection

For successful design of the thrust vectoring system suitable for a propeller UAV, it requires a careful investigation and selection of the existing methods of vectoring a propulsion system thrust. Consequently, an iterative selection study was carried out and based on criteria; weight, suitability, ease of integration, and easy to construct. Among the methods studied (with details in section 2.11), one of the most likely method to achieve the maneuverability on a propeller aircraft would be by swivelling either the entire engine or the propeller. However, this method was discarded due to the yaw motion caused which the control surfaces could not counteract (Carstens, 2017). Finally, jet vane thrust vectoring was given a higher rating and was thus chosen as the best method suitable for a push propeller driven UAV as it gave an optimal result and an easy to integrate configuration. This can be attributed to the fact that it can be incorporated into a shroud system conceived to be the best add-on to the airframe to make the thrust vectoring possible. The remainder of the work confirmed that jet vane thrust vectoring was the preferred choice and it yielded the right result expected.

7.1.2 TVC Conceptual Design

During the take-off phase under consideration in this project, the control surfaces were ineffective to maneuver the UAV. All the factors that would encourage a proper, stable and successful operation were duly considered at the design stage. The design of the TVC system was in three phases namely the vane design, the shroud design, and the geometry assembly.

Based on the result of the preliminary CFD analysis presented in section 4.1 and the condition mentioned in section 4.3, NACA 0012 was selected and used to design the vanes. The vanes were made in airfoil shape in order to achieve the dual purpose of maneuvering the UAV as well

as generating lift to augment the lift generated by the wings. This was aimed at achieving earlier take-off of the aircraft, and it was achieved using six vanes arranged in parallel formation and when integrated to the UAV, could be operated simultaneously or independently to cause a change in the attitude of the aircraft.

The shrouded propeller (ducted fan) system proposed by Parlett (1950) and presented in section 2.4 was conceived and designed as the most stable and suitable method to channel the free stream air from the propeller unto vanes to be placed at the exit of the shroud. The design was made using the propulsion design characteristics of the GII UAV. The result of the TVC system characterization proves that shroud system enhances propeller performance. It also contributes to the lift generation, a requirement for the system designed.

The final design (Figure 4.8) presented in section 4.4.1 was made by designing some other auxiliary components and assembling of the vanes in the shroud.

7.1.3 Thrust Vectoring System Characterization

7.1.3.1 Propeller Air Velocity Measurement

For proper design and analysis of the TVC system, it was necessary to ascertain the actual air velocity of a propeller in a shroud when operated at some speed. A propeller air velocity profile experiment was therefore conducted on a designed and manufactured laboratory test bench (section 3.1). The test bench was designed to handle a C6374 – 200 brushless electric motor or an internal combustion engine with a rating of 7.5 kW or less capable of driving a three-bladed propeller of up to 27 inches at a variable speed of up to 6000 rpm. The design was in accordance with the requirements of the CPUT AMTL UAV technology demonstrator for which this system is designed. The experiment was able to measure the air velocity of the propeller at various speeds and provided the input data necessary for the other stages of the thrust vectoring design and characterization. It can be inferred that the experiment measures and proves that the propeller air velocity varies from 0 m/s at the tip and increases along propeller to the maximum of 20.5 m/s at the centre before decreasing to 0 m/s at the core (Appendix A).

7.1.3.2 TVCS CFD Characterization

Chapter 5 presented the successful CFD characterization process of the TVC system in ANSYS Fluent 2019R using the experimental data from the propeller velocity profile experiment (mass flowrate obtained by calculation using equation 5.7) as the inlet boundary condition. The result of this analysis shows the possibility of the design to generate operational characteristics (lift, drag and moment) to augment the forces of the GII platform. This provides that when the TVC system is integrated onto the GII UAV can reduce the S_g and the rate of climb.

7.1.3.3 TVC Effect on Ground Roll Distance

The maneuverability purpose and desire of the design were to control and augment the GII UAV control surfaces. This desired nature of control is to reduce the ground roll distance bring about early take-off. The ground roll distance depends on the time it takes the wing to generate the lift forces enough to overcome the limiting forces (weight and drag) to allow lifting. As soon as the desired lift is acquired, the aircraft can take-off irrespective of the distance covered. Based on the qualitative and quantitative result presented in section 6.2, the TVC system shows a positive sense in generating the UAV operational forces required to augment the wings and support early take-off and climb. As presented in section 6.3, the TVC system reduces the S_g to a minimum of 47.26% and a maximum of 65.19% when compared to the GII UAV without TVC system.

Section 6.3.1.3 presented the thrust value that best supports the operation of the UAV when TVC system is integrated onto it. It shows that with a low α value, the TVC system will provide better support to the UAV.

7.1.3.4 TVC Effect on the Rate of Climb and Power Usage

Section 6.4 presented the support of the TVC system to reduce the rate of climb and overall power required for the UAV operation. A minimum of 17.23% and a maximum of 31.33% reduction of the rate of climb was recorded with TVC system on the UAV. The total power needed to propel the UAV from V_0 to the point when it clears obstacles was reduced to a minimum of 62.37% and a maximum of 85.53%.

7.1.3.5 TVC Effect on the Attitude of the Aircraft

The maneuverability of the aircraft to change the attitude was achieved. The results presented in section 6.1 to 6.5 show in different magnitude to which the TVC system affected the operation of the GII UAV living it with the desired short take-off and quick climb capabilities.

7.2 Recommendation

The computational analysis proved that the designed system is capable to achieve the purpose of shortening the take-off distance of the aircraft by enabling it to generate lift, moment, and less drag. However, through the process of conducting this research work, several problems were encountered, and some observations were made. Based on these problems and observations, the following set of recommendations are made for consideration, and for future work and research:

1. At the point of selecting the airfoil to use for the vane design, the author based his decision on the thin airfoil theory and structural stability. However, it is recommended that further work should be done using the NACA 0006 which gives the best result from the analysis not minding the thin airfoil theory and structural integrity. This theory and

structural strength were found by the author to be considered when dealing with the wings which supports the weight of the aircraft.

2. This designed system was analyzed in isolation to ascertain its workability, hence there is a need to integrate the system unto the airframe and then analyze the complete system to determine its performance when incorporated to the host frame.
3. The result presented does not take the weight of the TVC system into account hence further work and the analysis should consider the weight as it contributes to the total weight of the UAV.
4. There is a need to optimize the entire components of the system to increase the drag polar thereby improving the performance of the system.

REFERENCES

- A Gogoi, R Vashistha, S V Singh, S. hankar. 2013. Design and CFD Analysis of Yaw Thrust Vectoring in Rectangular Nozzle of Tail-less Aircraft. *AIAA Journal*, (September 2013).
- Abbott, I.H. & Von Doenhoff, A.E. 1959. Theory of Wing Sections: Including a Summary of Airfoil data. *Press*, 11: 693. http://www.amazon.com/Theory-Wing-Sections-Including-Summary/dp/0486605868/ref=pd_sim_b_90.
- Abrego, A. & Bulaga, R. 2002. Performance Study of a Ducted Fan System. *AHS Aerodynamics, Aeroacoustic ...*: 1–6. <https://ntrs.nasa.gov/search.jsp?R=20020052231> 9 December 2019.
- AGARD. 1974. Take-off and Landing. In *44th meeting of the flight mechanics panel of AGARD*. 6–6.
- Airfoiltools. Airfoil tool generator. <http://airfoiltools.com/airfoil/naca4digit> 10 May 2018.
- Akturk, A. 2010. *Ducted Fan Inlet/Exit and Rotor Tip Flow Improvements for Vertical Lift System*. Cambridge: Cambridge University Press. http://ezproxy.net.ucf.edu/login?url=http://search.proquest.com/docview/1427926684?accountid=10003%5Cnhttp://sfx.fcla.edu/ucf?url_ver=Z39.88-2004&rft_val_fmt=info:ofi/fmt:kev:mtx:dissertation&genre=dissertations+&+theses&sid=ProQ:ProQuest+Dissertations+&+
- Akturk, A. & Camci, C. 2010. Influence of tip clearance and inlet flow distortion on ducted fan performance in VTOL UAVs. In *Annual Forum Proceedings - AHS International*. 1443–1453. http://www.personal.psu.edu/~users/c/x/cxc11/papers/AHS_2010_Forum66_AA_CC.pdf 4 July 2019.
- Amick, K.G. 2005. *The next great engine war analysis and recommendations for managing the Joint Strike Fighter Engine competition*. <http://hdl.handle.net/10945/1854> 15 July 2020.
- Anderson, John David, J. 1984. *Fundamentals of Aerodynamics*. McGraw-Hill Companies.
- Anderson, J. 2013. *Fundamentals of Fundamentals of*.
- ANSYS. 2012. ANSYS FLUENT User ' s Guide. *Knowledge Creation Diffusion Utilization*, 15317(October): 724–746.
- AOE. Take-off and Landing performance.
- AviationNepal. 2017. Future of thrust vectoring. <http://aviationnepal.com/blogs/future-of-thrust-vectoring/> 31 May 2018.

- aviationsmilitaires. 2017. History of the device Doak VZ-4. <https://www.aviationsmilitaires.net/v2/base/view/Model/1961.html> 12 December 2019.
- Ball, T.M. 2008. CFD as Applied to the Design Of Short Take-off and Landing Vehicles Using Circulation Control. , (June).
- Baokai, Z. 1995. Preliminary Study On Effects Of Thrust Vectoring. *Feixing Lixue*, 12: 23–27.
- Bates, L.B. & Young, D.T. 2012. Developmental Testing of Electric Thrust Vector Control Systems for Manned Launch Vehicle Applications. In *Proceedings of 41st Aerospace mehanism, jet propulsion laboratory*. Huntsville, AL Proceedings:* NASA George C. Marshall Space Flight Centre: 181–194.
- BERRIER, B. & TAYLOR, J. 1990. *Internal performance of two nozzles utilizing gimbal concepts for thrust vectoring*. <http://www.csa.com/partners/viewrecord.php?requester=gs&collection=TRD&recid=N9019200AH>.
- Carstens, J. 2017. Torque generated by swiveling or tilting the engine causes yaw and roll motion (personal interview).
- Carter, B.R. 2005. *Time-Optimization of High Performance Combat Manovers*. NAVAL POSTGRADUATE SCHOOL, MONTEREY, CALIFORNIA.
- Chan, M. 2020. China's stealth fighter Agility. <https://www.scmp.com/news/china/military/article/3092839/chinas-stealth-fighter-goes-mass-production-after-thrust> 16 July 2020.
- Chandra Murty, M.S.R. & Chakraborty, D. 2015. Numerical characterisation of jet-vane based thrust vector control systems. *Defence Science Journal*, 65(4): 261–264.
- Clarke, A.J. 2011. *The Conceptual Design of Novel Future UAV's Incorporating Advanced Technology Research Components*. Cranfield University.
- Connors, J. 2010. The Engine of Pratt and Whitney: A Technical History. *American Institute of Aeronautics and Astronautics, Inc*: 1–29.
- Cycon, J., Rosen, K. & Whyte, A. 1992. Unmanned flight vehicle including counter rotating rotors positioned within a toroidal shroud and operable to provide all required vehicle flight controls. *US Patent 5,152,478*: 1–7. <http://www.google.com/patents/US5152478>.
- Cyklis, P. & Młynarczyk, P. 2016. The Influence of the Spatial Discretization Methods on the Nozzle Impulse Flow Simulation Results. In *Procedia Engineering*. 396–403.
- Daidzic, N.E. 2016. Optimization of Take-offs on Unbalanced Fields using Take-off

- Performance Tool. *International Journal of Aviation, Aeronautics, and Aerospace*, 3(3): 7–18. <https://doi.org/10.15394/ijaaa.2016.1129> 27 June 2020.
- Daljil Majil, D. 2016a. Design and Analysis of Jet Vane Thrust Vectoring Nozzle using CFD and Optimization of Nozzle Parameters. *Indian Journal of Science and Technology*, 9(39). <http://www.indjst.org/index.php/indjst/article/view/100778>.
- Daljil Majil, D. 2016b. Design and Analysis of Jet Vane Thrust Vectoring Nozzle using CFD and Optimization of Nozzle Parameters. *Indian Journal of Science and Technology*, 9(39). <https://indjst.org/articles/design-and-analysis-of-jet-vane-thrust-vectoring-nozzle-using-cfd-and-optimization-of-nozzle-parameters>.
- Defenseissues. 2013. Usefulness of thrust vectoring. <https://defenseissues.net/2013/04/13/usefulness-of-thrust-vectoring/> 15 September 2016.
- Dhawan, S. 2014. How is the thrust vectoring system on the Sukhoi PAK-FA different from the F-22. <https://www.quora.com/How-is-the-thrust-vectoring-system-on-the-Sukhoi-PAK-FA-different-from-the-F-22>.
- Dinç, A. 2015. Sizing of a turboprop unmanned air vehicle and its propulsion system. *Isi Bilimi Ve Teknigi Dergisi/ Journal of Thermal Science and Technology*, 35(2): 53–62.
- Diseno-art. 2014. DOAK Model 16 VZ-4 VTOL Aircraft. http://www.diseno-art.com/encyclopedia/strange_vehicles/doak_model_16_vz-4.html 12 December 2019.
- Filippone, A. 2012. *Advanced Aircraft Flight Performance*. Cambridge: Cambridge University Press. <http://ebooks.cambridge.org/ref/id/CBO9781139161893>.
- Fleming, J., Jones, T., Ng, W., Gelhausen, P. & Enns, D. 2003. Improving control system effectiveness for ducted fan VTOL UAVs operating in crosswinds. In *2nd AIAA 'Unmanned Unlimited' Conference and Workshop and Exhibit*.
- Forghany, F., Taeibe-Rahni, M. & Asadollahi-Ghohieh, A. 2018. Numerical investigation of freestream flow effects on thrust vector control performance. *Ain Shams Engineering Journal*, 9(4): 3293–3303. <https://doi.org/10.1016/j.asej.2017.12.004>.
- Gologan, C. & Schmitt, D. 2010. Comparison of Powered-Lift Turbofan Aircraft With Conventional Turboprop. In *27TH INTERNATIONAL CONGRESS OF THE AERONAUTICAL SCIENCES*.
- Ikaza, D. 2000a. Thrust Vectoring Nozzle for Military Aircraft Engines. *22nd Congress of International Council of the Aeronautical Sciences*: 1–10.

- Ikaza, D. 2000b. Thrust Vectoring Nozzle for Modern Military Aircraft. *NATO R&T Organization Symposium*, (May): 8–11. <http://oai.dtic.mil/oai/oai?verb=getRecord&metadataPrefix=html&identifier=ADP011109>.
- Jones, W.P. & Launder, B.E. 1972. The prediction of laminarization with a two-equation model of turbulence. *International Journal of Heat and Mass Transfer*, 15(2): 301–314.
- Joslin, R.D. & Miller, D.N. 2009. *Fundamentals and Applications of Modern Flow Control*. American Institute of Aeronautics and Astronautics.
- Kayne, A. & Agarwal, R. 2013. Computational Fluid Dynamics Modeling of Mixed Convection Flows in Building Enclosures. In *ASME 2013 7th International Conference on Energy Sustainability*. V001T01A004. <http://proceedings.asmedigitalcollection.asme.org/proceeding.aspx?doi=10.1115/ES2013-18026>.
- Kijjarvi, J. 2011. Darcy Friction Factor Formulae in Turbulent Pipe Flow. *Lunowa Fluid Mechanics Paper*. 1–11. <http://www.kolumbus.fi/jukka.kijjarvi/clunowa/clunowa.html> 28 June 2019.
- Li, L. 2011. *Numerical and Experimental Studies of Fluidic Thrust Vectoring*. Muroran institute of technology.
- Mair, W.A. & Edwards, B.J. 1965. A Parametric Study of Take-Off and Landing Distances for High-Lift Aircraft. *Aeronautical Research Council*, (C. P. No. 823).
- Mason, M. & Crowther, W. 2004. Fluidic Thrust Vectoring for Low Observable Air Vehicles. In *2nd AIAA Flow Control Conference*. Reston, Virginia: American Institute of Aeronautics and Astronautics: 10–12. http://www.geocities.ws/m_mason007/Paper.pdf.
- Menter, F.R. 1994. Two-equation eddy-viscosity turbulence models for engineering applications. *AIAA Journal*, 32(8): 1598–1605. <http://arc.aiaa.org/doi/10.2514/3.12149>.
- Menter, F.R., Kuntz, M. & Langtry, R. 2003. Ten Years of Industrial Experience with the SST Turbulence Model. *Turbulence Heat and Mass Transfer* 4, 4: 625–632. http://cfd.mace.manchester.ac.uk/flomania/pds_papers/file_pds-1068134610Menter-SST-paper.pdf.
- Michalcová, V., Lausová, L., Skotnicová, I. & Pospíšil, S. 2017. Computational Simulations of the Thermally Stratified Atmospheric Boundary Layer above Hills. In *Procedia Engineering*. 134–139.
- Mort, Kenneth W & Yaggy, P.F. 1962. *Aerodynamic Characteristics of a 4-foot-diameter Ducted Fan Mounted on the Tip of a Semispan Wing*.

- <https://ntrs.nasa.gov/search.jsp?R=20020052382> 14 December 2019.
- Mort, Kenneth W. & Yaggy, P.F. 1962. *Aerodynamic Characteristics of a 4-foot-diameter Ducted Fan Mounted on the Tip of a Semispan Wing*. <https://ntrs.nasa.gov/search.jsp?R=19620001045> 14 December 2019.
- MoTIS, V. 2007. TEST ZONE PRESENTATIONS. <http://www.motivirtualjetdesign.com/MoTISTESTZONE.htm> 15 July 2020.
- Nasa. Gimbaled thrust vectoring. <https://spaceflight systems.grc.nasa.gov/education/rocket/gimbaled.html> 20 January 2018.
- Noaman, H.R., Tang, H. Bin & Khalil, E. 2019. Numerical Simulation on the Influence of Injection Location, Injection Angle, and Divergence Half Angle on SITVC Nozzle Flow Field. *International Journal of Aerospace Engineering*, 2019: 1–16. <https://www.hindawi.com/journals/ijae/2019/7392497/>.
- Omics. 2014. Doak VZ-4 Development. http://research.omicsgroup.org/index.php/Doak_VZ-4 12 December 2019.
- Oppermann, R.H. 1937. National advisory committee for aeronautics: physical Chemistry. *Journal of the Franklin Institute*, 223(3): 403. <https://linkinghub.elsevier.com/retrieve/pii/S0016003237907403>.
- Parlett, L.P. 1950. Aerodynamic Characteristics of a Small-scale Shrouded propeller at Angles of attack from 0 to 90. *NACA Technical Note 3547*, (April). <https://apps.dtic.mil/dtic/tr/fulltext/u2/a377337.pdf> 5 July 2019.
- Pereira, J. 2008. HOVER AND WIND-TUNNEL TESTING OF SHROUDED ROTORS FOR IMPROVED MICRO AIR VEHICLE DESIGN Jason L . Pereira Doctor of Philosophy , 2008 Professor Inderjit Chopra Department of Aerospace Engineering. *Doctor*.
- Petersen, M. 2010. *DEVELOPMENT OF A SEAMLESS MORPHING*. Cape Peninsula University of Technology, Cape Town South Africa.
- Petrescu, I.R.& F. 2013. *Aircraft II Color*.
- Platt Jr, R.J. 1948. Static Tests of a Shrouded and Unshrouded Propeller. *Library*. <https://apps.dtic.mil/dtic/tr/fulltext/u2/a800783.pdf> 28 June 2019.
- Pope, S. 2000. *Turbulent Flows*. Cambridge University press.
- Pope, S.B. 2000. *Turbulent Flows*. Cambridge University press.
- Prasath, K., Prasanth, C., Rakesh, P. & Abinaya, R. 2020. CFD ANALYSIS OF DUAL THROAT

THRUST VECTORING WITH CHEVRON NOZZLE. : 3822–3826.

- Prez-Segarra, C.D., Lehmkuhl, O. & Jaramillo, J. 2009. Turbulence modelling and numerical issues: from RANS to DNS and LES. *Actas da III Conferência Nacional em Mecânica de Fluidos, Termodinâmica e Energia (MEFTE - BRAGANÇA 09) resumos.*, (January 2015): 15–16.
- Revolv. 2016. Thrust vectoring. [https://www.revolv.com/main/index.php?s=Thrust vectoring&item_type=topic](https://www.revolv.com/main/index.php?s=Thrust+vectoring&item_type=topic) 20 April 2016.
- Rockwell-MBBX-31. 1990. No Title.
http://www.militaryfactory.com/aircraft/detail.asp?aircraft_id=1583 2 July 2016.
- Sacks, A.H. & Burnell, J.A. 1962. Ducted propellers—a critical review of the state of the art. *Progress in Aerospace Sciences*, 3(C): 85–135.
<https://linkinghub.elsevier.com/retrieve/pii/0376042162900179>.
- Sadraey, M.H. 2017. *Aircraft performance; An Engineering Approach*. Third Edition. | New York: Routledge, 2017. | Revised edition of the author's: Routledge.
<https://www.taylorfrancis.com/books/9781317170358/chapters/10.4324/9781315570662-7>.
- Sankar, S. & Sreejith, K. V. 2018. CFD Analysis of a Thrust Vectoring Nozzle. : 4899–4904.
- Schaefermeyer, M.R. 2011. *AERODYNAMIC THRUST VECTORING FOR ATTITUDE CONTROL FOR A VERTICALLY THRUSTING JET ENGINE*. UTAH STATE UNIVERSITY Logan, Utah.
<https://digitalcommons.usu.edu/cgi/viewcontent.cgi?article=2221&context=etd>.
- Sez, E. 2019. Abort Authority; Abnormal Procedures.
https://code7700.com/abort_authority.htm 15 July 2020.
- Skybrary. 2016. Factors Affecting Aircraft Performance During Take-off and Climb.
https://www.skybrary.aero/index.php/AP4ATCO_-_Factors_Affecting_Aircraft_Performance_During_Take-off_and_Climb 14 June 2019.
- SQUIRE, H.B. 1957. Theory of Flight. *Nature*, 179(4557): 446–446.
<http://web.mit.edu/16.00/www/aec/flight.html> 3 July 2019.
- Sumathy, L.A.K. 2015. *Analysis and Fabrication of a Rocket Simulator Prototype For Thrust Vectoring Stabilization*. Luleå University of Technology.
- Taylor, R.T. 1943. National Advisory Committee for Aeronautics. *Journal of Applied Physics*, 14(8): 399–405. <http://aip.scitation.org/doi/10.1063/1.1715007>.

- Tesla, N. 1898. Methods of and apparatus for controlling mechanism of moving vessels or vehicles. : 1–13.
<http://www.google.com/patents/US613809?printsec=abstract#v=onepage&q&f=false>.
- Versteeg, H.K. & Malalasekera, W. 2007. *An Introduction to Computational Fluid Dynamics*.
- Vinayagam, A. & Sinha, N.K. 2014. An assessment of thrust vector concepts for twin-engine airplane. *Proceedings of the Institution of Mechanical Engineers, Part G: Journal of Aerospace Engineering*, 228(6): 960–979.
<http://journals.sagepub.com/doi/10.1177/0954410013485697>.
- Vinayagam, A.K. & Sinha, N.K. 2014. An assessment of thrust vector concepts for twin-engine airplane. *Proceedings of the Institution of Mechanical Engineers, Part G: Journal of Aerospace Engineering*, 228(6): 960–979.
- Vinayagam, A.K. & Sinha, N.K. 2013. Optimal aircraft take-off with thrust vectoring. *The Aeronautical Journal*, 117(1197): 1119–1138.
https://www.cambridge.org/core/product/identifier/S0001924000008733/type/journal_article.
- Wang, W., Zhu, J. & Kuang, M. 2017. Design, modelling and hovering control of a tail-sitter with single thrust-vectorized propeller. *IEEE International Conference on Intelligent Robots and Systems*, 2017-Sept: 5971–5976.
- Wang, Y. & Wang, D. 2016. Variable thrust directional control technique for plateau unmanned aerial vehicles. *Science China Information Sciences*, 59(3): 033201:1-033201:4.
- Williams, J. 1972. Aircraft Performance - Prediction Methods And Optimization. In *Lecture Series of Fluid Dynamics Panel of AGARD and the von Kärman Institute*.
 c:%5CICT%5CEILS%5CHypergole Systeme%5C1973 Rep Effect of Pressure on Ignition of Hypergolic Liquid Propellants.pdf TS - RIS.
- Zhao Baokai. 1995. 19951023 091. *Feixing Lixue*, 12: 23–27.
- Zhiyin, Y. 2015. Large-eddy simulation: Past, present and the future. *Chinese Journal of Aeronautics*, 28(1): 11–24.
- Živković, S., Milinović, M. & Adamec, N. 2014. Experimental and numerical research of a supersonic planar thrust vectoring nozzle via mechanical tabs. *FME Transaction*, 42(3): 205–211. <http://scindeks.ceon.rs/Article.aspx?artid=1451-20921403205Z>.

Appendix A:

Distance	1000 RPM	1100 RPM	1200 RPM	1300 RPM	1400 RPM	1500 RPM	1600 RPM	1700 RPM	1800 RPM	1900 RPM	2000 RPM	2100 RPM	2200 RPM	2300 RPM	2400 RPM	2500 RPM	2600 RPM	2700 RPM	3000 RPM	3500 RPM	4000 RPM
0	4	4	3	3	3	4	4	5	3,5	4	4	3,5	3,5	3,5	4	4,5	3,5	2,5	4,5	4,5	5
15	4,5	4,5	3,5	3,5	3,5	4	4,5	5	4	4,5	4,5	4	4	3,5	5	4,5	5	4,5	6,5	5	5,5
30	4,5	4,5	4	3,5	4,5	5,5	5	6	4	6	5,5	6	5,5	4,5	5,5	6	7	7,5	7	7	8
45	5	5,5	4,5	5	5	6	6	6	6	8,5	8	9	10	10	9	10	11	10,5	11,5	11	14
60	6	6	6	7	7	8	8	8,5	8,5	10,5	10,5	11,5	12	13	12,5	13,5	14,5	14	14,5	17,5	18,5
75	6,5	7	6,5	7	8	8,5	9	9,5	10	11	11,5	12	12,5	13	13	13,5	15,5	15	16	19	20,5
90	6,5	7	6,5	8	8	9	9	10	10	11	11,5	12	12,5	13	13,5	14	14,5	15,5	17	19	21
105	6,5	6,5	6,5	7,5	8	8,5	9,5	10	10,5	11	11,5	12	12,5	13	13,5	14	14,5	15	17	18,5	21
120	6,5	6,5	7	7	8	8,5	9	10	10,5	10,5	11	11,5	12	13	13	13,5	14,5	14,5	17	18,5	20
135	6,5	6,5	7	7	7,5	8	9	9,5	10	10	10,5	11	11,5	12	12,5	13	13,5	13,5	15,5	18	19,5
150	6	6,5	6,5	7	7,5	8	8,5	9	9,5	9	10	10,5	11	12	11,5	11,5	12,5	12,5	14,5	17	17,5
165	6	6,5	6	7	7	8	8	8,5	8,5	8,5	9,5	9	10	10,5	11	11	11,5	11	13,5	15,5	16
180	5,5	6	5	6	6,5	7	7	7	6,5	7,5	8	8	8	9	8,5	9,5	9,5	9	12	13	15

Appendix B: Take-off distance reduction at different α value

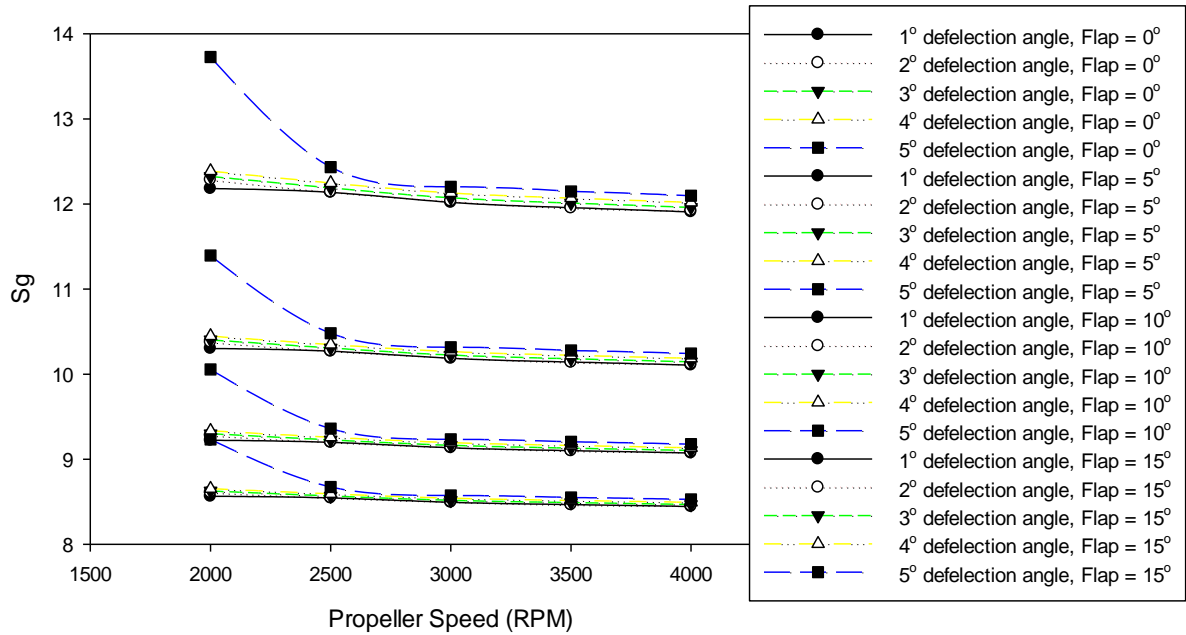


Figure B.1 Take-off distance (S_g) reduction at $\alpha = 0.002$

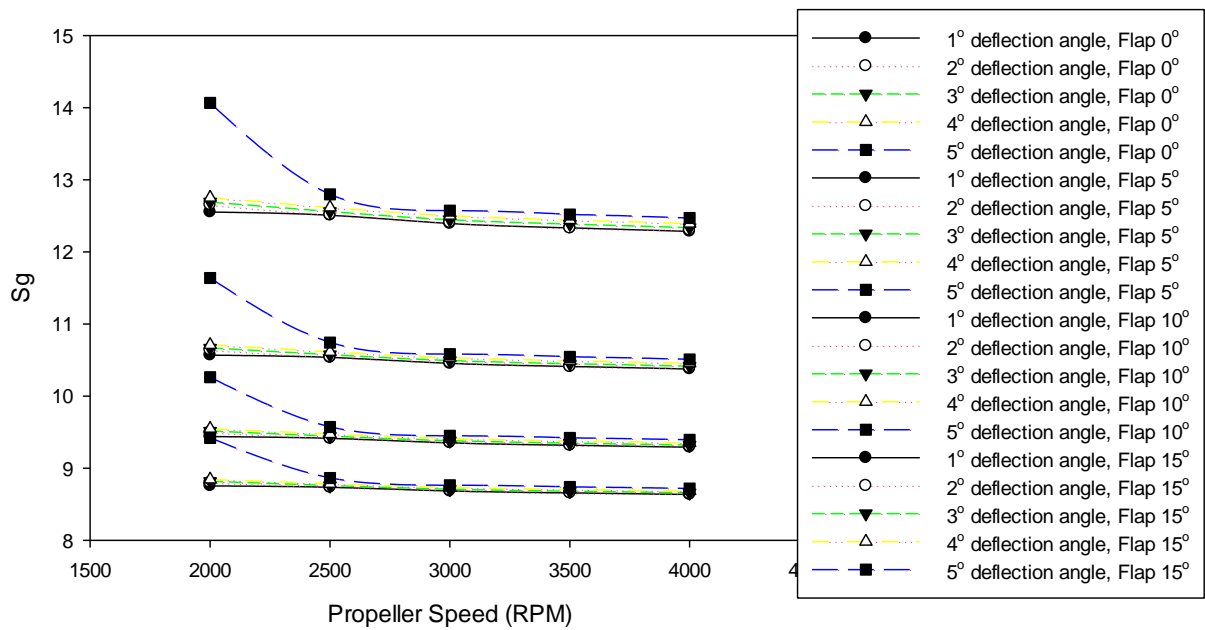


Figure B.2 Take-off distance (S_g) reduction at $\alpha = 0.004$

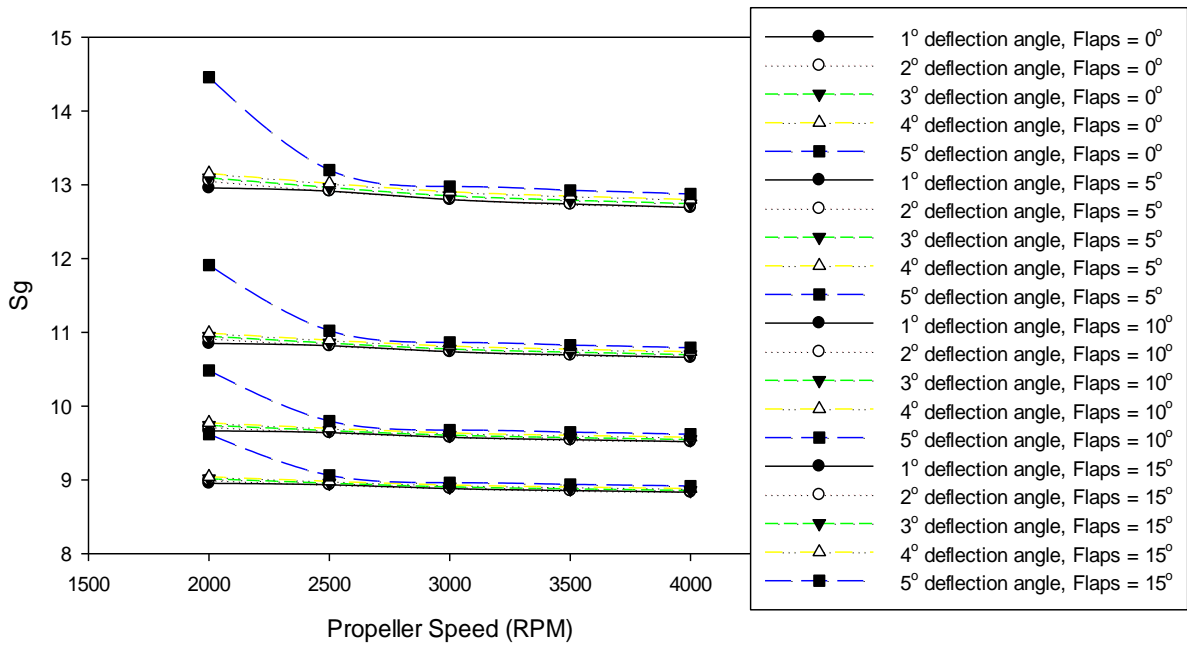


Figure B.3 Take-off distance (Sg) reduction at $\alpha = 0.006$

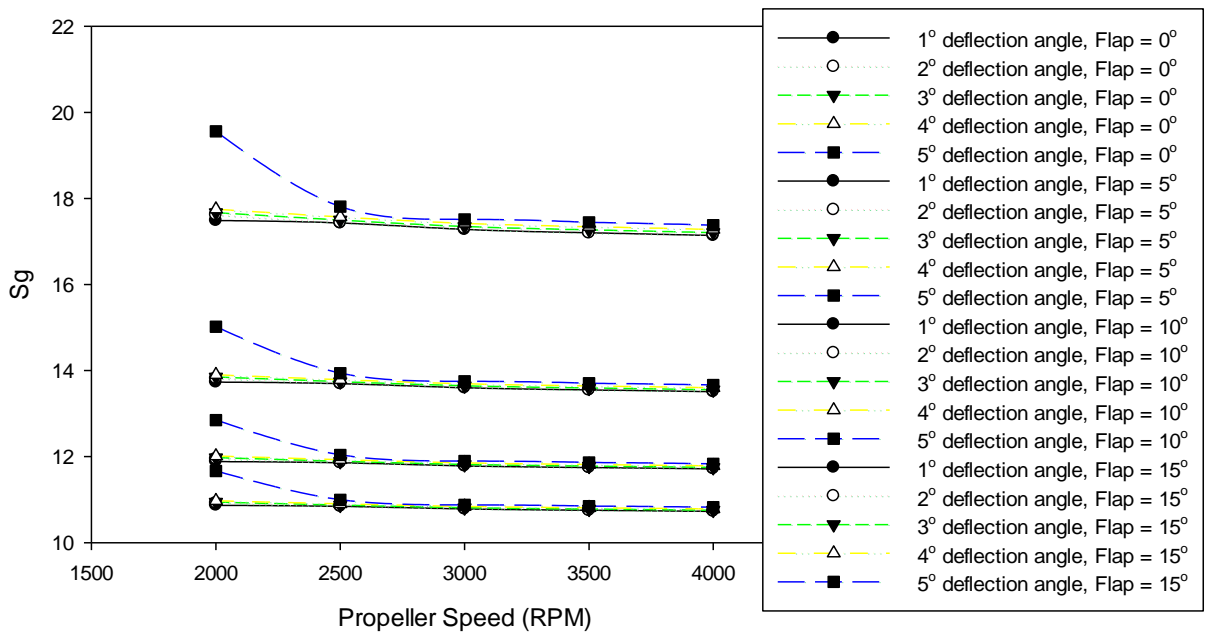


Figure B.4 Take-off distance (Sg) reduction at $\alpha = 0.02$

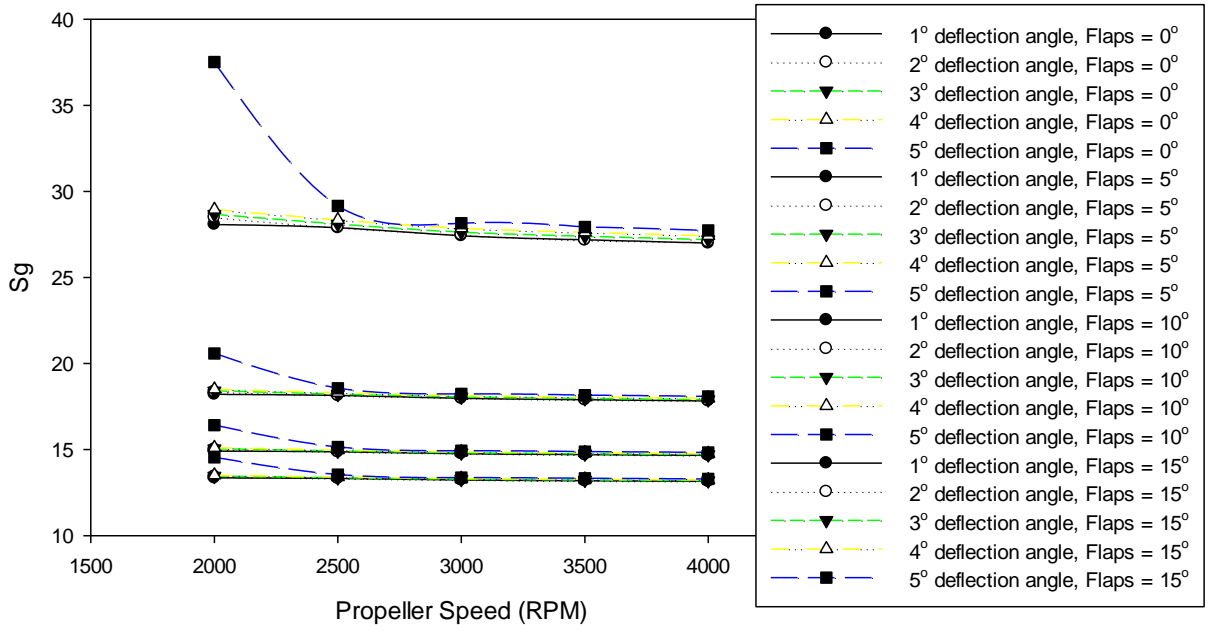


Figure B.5 Take-off distance (Sg) reduction at $\alpha = 0.03$

Appendix C: Percentage Increase in Aircraft Coefficient of Lift

Table C.1 Percentage increase in aircraft coefficient of lift at flaps = 0°

	2000 RPM	2500 RPM	3000 RPM	3500 RPM	4000 RPM
Vane deflection angle (degree)					
1	0.08%	0.33%	0.33%	0.33%	0.33%
2	0.76%	0.79%	0.86%	0.92%	0.77%
3	1.19%	1.19%	1.20%	1.20%	1.21%
4	1.62%	1.62%	1.63%	1.64%	1.64%
5	2.32%	2.05%	2.28%	2.06%	2.07%

Table C.2 Percentage increase in aircraft coefficient of lift at flaps = 5°

	2000 RPM	2500 RPM	3000 RPM	3500 RPM	4000 RPM
Vane deflection angle (degree)					
1	0.07%	0.28%	0.28%	0.28%	0.28%
2	0.64%	0.66%	0.72%	0.78%	0.65%
3	1.00%	1.00%	1.01%	1.02%	1.02%
4	1.37%	1.37%	1.38%	1.38%	1.39%
5	1.96%	1.73%	1.93%	1.75%	1.75%

Table C.3 Percentage increase in aircraft coefficient of lift at flaps = 10°

	2000 RPM	2500 RPM	3000 RPM	3500 RPM	4000 RPM
Vane deflection angle (degree)					
1	0.06%	0.24%	0.25%	0.25%	0.25%
2	0.56%	0.59%	0.64%	0.68%	0.58%
3	0.89%	0.89%	0.89%	0.90%	0.90%
4	1.21%	1.21%	1.21%	1.22%	1.22%
5	1.73%	1.53%	1.71%	1.54%	1.55%

Table C.4 Percentage increase in aircraft coefficient of lift at flaps = 15°

	2000 RPM	2500 RPM	3000 RPM	3500 RPM	4000 RPM
Vane deflection angle (degree)					
1	0.05%	0.22%	0.22%	0.22%	0.22%
2	0.51%	0.53%	0.58%	0.62%	0.52%
3	0.80%	0.80%	0.81%	0.81%	0.81%
4	1.09%	1.09%	1.10%	1.10%	1.11%
5	1.56%	1.38%	1.54%	1.39%	1.40%

Appendix D: Percentage increase in Aircraft Coefficient of Drag**Table D.1 Percentage increase in aircraft coefficient of drag at flaps = 0°**

	2000 RPM	2500 RPM	3000 RPM	3500 RPM	4000 RPM
Vane deflection angle (degree)					
1	11.72%	11.52%	10.90%	10.58%	10.31%
2	12.33%	11.61%	11.05%	10.64%	10.46%
3	12.59%	11.91%	11.31%	10.99%	10.72%
4	12.96%	12.26%	11.67%	11.35%	11.09%
5	19.06%	13.25%	12.13%	11.82%	11.56%

Table D.2 Percentage increase in aircraft coefficient of drag at flaps = 5°

	2000 RPM	2500 RPM	3000 RPM	3500 RPM	4000 RPM
Vane deflection angle (degree)					
1	9.68%	9.51%	8.99%	8.72%	8.49%
2	10.20%	9.59%	9.12%	8.77%	8.62%
3	10.42%	9.85%	9.34%	9.06%	8.84%
4	10.74%	10.14%	9.64%	9.37%	9.15%
5	15.98%	10.98%	10.03%	9.77%	9.55%

Table D.3 Percentage increase in aircraft coefficient of drag at flaps = 10°

	2000 RPM	2500 RPM	3000 RPM	3500 RPM	4000 RPM
Vane deflection angle (degree)					
1	8.06%	7.92%	7.48%	7.25%	7.06%
2	8.50%	7.99%	7.59%	7.29%	7.16%
3	8.69%	8.20%	7.77%	7.54%	7.35%
4	8.96%	8.46%	8.03%	7.80%	7.61%
5	13.46%	9.17%	8.36%	8.14%	7.95%

Table D.4 Percentage increase in aircraft coefficient of drag at flaps = 15°

	2000 RPM	2500 RPM	3000 RPM	3500 RPM	4000 RPM
Vane deflection angle (degree)					
1	6.75%	6.63%	6.26%	6.06%	5.90%
2	7.12%	6.69%	6.35%	6.10%	5.99%
3	7.28%	6.87%	6.50%	6.31%	6.14%
4	7.51%	7.08%	6.72%	6.53%	6.37%
5	11.38%	7.69%	7.00%	6.81%	6.65%

Appendix E: Input and Output Boundary Conditions

E.1: 2000 RPM

E.1.1: Mass Flowrate Profile

((distancemassflowrate-prof 169)

(x

-2.45 -2.45 -2.45 -2.45 -2.45 -2.45 -2.45 -2.45 -2.45 -2.45 -2.45 -2.45 -2.45 -2.45 -2.45 -2.45
-2.45 -2.45 -2.45 -2.45 -2.45 -2.45 -2.45 -2.45 -2.45 -2.45 -2.45 -2.45 -2.45 -2.45 -2.45 -2.45
-2.45 -2.45 -2.45 -2.45 -2.45 -2.45 -2.45 -2.45 -2.45 -2.45 -2.45 -2.45 -2.45 -2.45 -2.45 -2.45
-2.45 -2.45 -2.45 -2.45 -2.45 -2.45 -2.45 -2.45 -2.45 -2.45 -2.45 -2.45 -2.45 -2.45 -2.45 -2.45
-2.45 -2.45 -2.45 -2.45 -2.45 -2.45 -2.45 -2.45 -2.45 -2.45 -2.45 -2.45 -2.45 -2.45 -2.45 -2.45
-2.45 -2.45 -2.45 -2.45 -2.45 -2.45 -2.45 -2.45 -2.45 -2.45 -2.45 -2.45 -2.45 -2.45 -2.45 -2.45

0.1633 0.20413 0.24496 -0.245 -0.20417 -0.16334 -0.12251 -0.08168 -0.04085
 -2E-05 0.04081 0.08164 0.12247 0.1633 0.20413 0.24496 -0.245 -0.20417
 -0.16334 -0.12251 -0.08168 -0.04085 -2E-05 0.04081 0.08164 0.12247
 0.1633 0.20413 0.24496 -0.245 -0.20417 -0.16334 -0.12251
 -0.08168 -0.04085 -2E-05 0.04081 0.08164 0.12247 0.1633
 0.20413 0.24496 -0.245 -0.20417 -0.16334 -0.12251
 -0.08168 -0.04085 -2E-05 0.04081 0.08164 0.12247 0.1633
 0.20413 0.24496 -0.245 -0.20417 -0.16334 -0.12251
 -0.08168 -0.04085 -2E-05 0.04081 0.08164 0.12247 0.1633
 0.20413 0.24496 -0.245 -0.20417 -0.16334 -0.12251 -0.08168
 -0.04085 -2E-05 0.04081 0.08164 0.12247 0.1633 0.20413 0.24496-
 0.245 -0.20417 -0.16334 -0.12251 -0.08168 -0.04085 -2E-05
 0.04081 0.08164 0.12247 0.1633 0.20413 0.24496 -0.245
 -0.20417 -0.16334 -0.12251 -0.08168 -0.04085 -2E-05 0.04081
 0.08164 0.12247 0.1633 0.20413 0.24496 -0.245 -0.20417
 -0.16334 -0.12251 -0.08168 -0.04085 -2E-05 0.04081 0.08164
 0.12247 0.1633 0.20413 0.24496 -0.245 -0.20417 -0.16334
 -0.12251 -0.08168 -0.04085 -2E-05 0.04081 0.08164 0.12247
 0.1633 0.20413 0.24496

)

(z

-0.245 -0.245 -0.245 -0.245 -0.245 -0.245 -0.245 -0.245 -0.245 -0.245 -0.245
 -0.245 -0.245 -0.2245 -0.2245 -0.2245 -0.2245 -0.2245
 -0.2245 -0.2245 -0.2245 -0.2245 -0.2245 -0.2245
 -0.2245 -0.2245 -0.204 -0.204 -0.204 -0.204 -0.204 -0.204 -0.204
 -0.204 -0.204 -0.204 -0.204 -0.204 -0.204 -0.1835 -0.1835 -0.1835

-0.1835	-0.1835	-0.1835	-0.1835	-0.1835	-0.1835	-0.1835	-0.1835	-0.1835	-0.1835	-0.1835
-0.1835	-0.1835	-0.1835	-0.1835	-0.1835	-0.1835	-0.163	-0.163	-0.163	-0.163	-0.163
-0.163	-0.163	-0.163	-0.163	-0.163	-0.163	-0.163	-0.163	-0.163	-0.163	-0.1425
-0.1425	-0.1425	-0.1425	-0.1425	-0.1425	-0.1425	-0.1425	-0.1425	-0.1425	-0.1425	-0.1425
-0.1425	-0.1425	-0.1425	-0.1425	-0.1425	-0.1425	-0.122	-0.122	-0.122	-0.122	-0.122
-0.122	-0.122	-0.122	-0.122	-0.122	-0.122	-0.122	-0.122	-0.122	-0.122	-0.122
-0.1015	-0.1015	-0.1015	-0.1015	-0.1015	-0.1015	-0.1015	-0.1015	-0.1015	-0.1015	-0.1015
-0.1015	-0.1015	-0.1015	-0.1015	-0.1015	-0.1015	-0.1015	-0.1015	-0.1015	-0.081	-0.081
-0.081	-0.081	-0.081	-0.081	-0.081	-0.081	-0.081	-0.081	-0.081	-0.081	-0.081
-0.081	-0.0605	-0.0605	-0.0605	-0.0605	-0.0605	-0.0605	-0.0605	-0.0605	-0.0605	-0.0605
-0.0605	-0.0605	-0.0605	-0.0605	-0.0605	-0.0605	-0.0605	-0.0605	-0.0605	-0.0605	-0.0605
-0.04	-0.04	-0.04	-0.04	-0.04	-0.04	-0.04	-0.04	-0.04	-0.04	-0.04
-0.04	-0.04	-0.0195	-0.0195	-0.0195	-0.0195	-0.0195	-0.0195	-0.0195	-0.0195	-0.0195
-0.0195	-0.0195	-0.0195	-0.0195	-0.0195	-0.0195	-0.0195	-0.0195	-0.0195	-0.0195	-0.0195
-0.0195	-0.0195	0	0	0	0	0	0	0	0	0
0	0	0	0	0	0					

)

(pressure

0.059	0.155	0.266	0.377	0.478	0.558	0.614	0.641	0.637	0.603	0.540	0.454
0.351	0.059	0.155	0.266	0.377	0.478	0.558	0.614	0.641	0.637	0.603	0.540
0.454	0.351	0.059	0.155	0.266	0.377	0.478	0.558	0.614	0.641	0.637	0.603
0.540	0.454	0.351	0.059	0.155	0.266	0.377	0.478	0.558	0.614	0.641	0.637
0.603	0.540	0.454	0.351	0.059	0.155	0.266	0.377	0.478	0.558	0.614	0.641
0.637	0.603	0.540	0.454	0.351	0.059	0.155	0.266	0.377	0.478	0.558	0.614
0.641	0.637	0.603	0.540	0.454	0.351	0.059	0.155	0.266	0.377	0.478	0.558

0.614 0.641 0.637 0.603 0.540 0.454 0.351 0.059 0.155 0.266 0.377 0.478
0.558 0.614 0.641 0.637 0.603 0.540 0.454 0.351 0.059 0.155 0.266 0.377
0.478 0.558 0.614 0.641 0.637 0.603 0.540 0.454 0.351 0.059 0.155 0.266
0.377 0.478 0.558 0.614 0.641 0.637 0.603 0.540 0.454 0.351 0.059 0.155
0.266 0.377 0.478 0.558 0.614 0.641 0.637 0.603 0.540 0.454 0.351 0.059
0.155 0.266 0.377 0.478 0.558 0.614 0.641 0.637 0.603 0.540 0.454 0.351
0.059 0.155 0.266 0.377 0.478 0.558 0.614 0.641 0.637 0.603 0.540 0.454
0.351

)

)

B.2: 2500 RPM

B.2.1: Mass Flowrate Profile

((distancemassflowrate-prof 169)

(x

-2.45 -2.45 -2.45 -2.45 -2.45 -2.45 -2.45 -2.45 -2.45 -2.45 -2.45 -2.45
-2.45 -2.45 -2.45 -2.45 -2.45 -2.45 -2.45 -2.45 -2.45 -2.45 -2.45 -2.45
-2.45 -2.45 -2.45 -2.45 -2.45 -2.45 -2.45 -2.45 -2.45 -2.45 -2.45 -2.45
-2.45 -2.45 -2.45 -2.45 -2.45 -2.45 -2.45 -2.45 -2.45 -2.45 -2.45 -2.45
-2.45 -2.45 -2.45 -2.45 -2.45 -2.45 -2.45 -2.45 -2.45 -2.45 -2.45 -2.45
-2.45 -2.45 -2.45 -2.45 -2.45 -2.45 -2.45 -2.45 -2.45 -2.45 -2.45 -2.45
-2.45 -2.45 -2.45 -2.45 -2.45 -2.45 -2.45 -2.45 -2.45 -2.45 -2.45 -2.45
-2.45 -2.45 -2.45 -2.45 -2.45 -2.45 -2.45 -2.45 -2.45 -2.45 -2.45 -2.45

(z

-0.245 -0.245 -0.245 -0.245 -0.245 -0.245 -0.245 -0.245 -0.245 -0.245 -0.245 -0.245
-0.245 -0.225 -0.225 -0.225 -0.225 -0.225 -0.225 -0.225 -0.225 -0.225 -0.225 -0.225
-0.225 -0.225 -0.204 -0.204 -0.204 -0.204 -0.204 -0.204 -0.204 -0.204 -0.204 -0.204
-0.204 -0.204 -0.204 -0.184 -0.184 -0.184 -0.184 -0.184 -0.184 -0.184 -0.184 -0.184
-0.184 -0.184 -0.184 -0.184 -0.163 -0.163 -0.163 -0.163 -0.163 -0.163 -0.163 -0.163
-0.163 -0.163 -0.163 -0.163 -0.163 -0.143 -0.143 -0.143 -0.143 -0.143 -0.143 -0.143
-0.143 -0.143 -0.143 -0.143 -0.143 -0.143 -0.122 -0.122 -0.122 -0.122 -0.122 -0.122
-0.122 -0.122 -0.122 -0.122 -0.122 -0.122 -0.122 -0.102 -0.102 -0.102 -0.102 -0.102
-0.102 -0.102 -0.102 -0.102 -0.102 -0.102 -0.102 -0.102 -0.081 -0.081 -0.081 -0.081
-0.081 -0.081 -0.081 -0.081 -0.081 -0.081 -0.081 -0.081 -0.081 -0.061 -0.061 -0.061
-0.061 -0.061 -0.061 -0.061 -0.061 -0.061 -0.061 -0.061 -0.061 -0.061 -0.040 -0.040
-0.040 -0.040 -0.040 -0.040 -0.040 -0.040 -0.040 -0.040 -0.040 -0.040 -0.040 -0.020
-0.020 -0.020 -0.020 -0.020 -0.020 -0.020 -0.020 -0.020 -0.020 -0.020 -0.020
-0.0200.000 0.000 0.000 0.000 0.000
0.000 0.000 0.000 0.000 0.000 0.000 0.000 0.000 0.000

)

(massflowrate

2.92 5.82 8.31 10.39 12.06 13.32 14.16 14.60 14.63 14.25 13.45 12.25
10.64 2.92 5.82 8.31 10.39 12.06 13.32 14.16 14.60 14.63 14.25 13.45
12.25 10.64 2.92 5.82 8.31 10.39 12.06 13.32 14.16 14.60 14.63 14.25
13.45 12.25 10.64 2.92 5.82 8.31 10.39 12.06 13.32 14.16 14.60 14.63
14.25 13.45 12.25 10.64 2.92 5.82 8.31 10.39 12.06 13.32 14.16 14.60
14.63 14.25 13.45 12.25 10.64 2.92 5.82 8.31 10.39 12.06 13.32 14.16

0.191 0.356 0.526 0.682 0.812 0.904 0.954 0.957 0.913 0.826 0.701 0.548

0.057 0.191 0.356 0.526 0.682 0.812 0.904 0.954 0.957 0.913 0.826 0.701

0.548

)

)